

# **So Many Dynamos:**

A study of planetary magnetic field morphologies

A thesis presented by

**Sabine Stanley**

to The Department of Earth and Planetary Sciences

in partial fulfillment of the requirements  
for the degree of Doctor of Philosophy  
in the subject of Geophysics

Harvard University  
Cambridge, Massachusetts

August 2004

© 2004 – Sabine Stanley  
All rights reserved.

## So Many Dynamos: A study of planetary magnetic field morphologies

### Abstract

We present 3-dimensional numerical dynamo models for Uranus, Neptune and Mercury. These three planets possess magnetic field morphologies quite different from the axially-dipolar dominated fields of Earth, Jupiter, Saturn and Ganymede. Uranus' and Neptune's fields are non-dipolar and non-axisymmetric, and Mercury's field is much weaker in magnitude than expected for an Earth-like dynamo. We examine whether these differences in planetary magnetic field morphologies can be explained by differences in the planets' convective-region geometries. We implement geometries that are consistent with Uranus', Neptune's and Mercury's interior structures in numerical dynamo models and analyze the resulting fields.

For Uranus and Neptune, the implemented geometry consists of a thin convecting shell surrounding a stably-stratified fluid core. The magnetic fields produced can match the observed surface power spectra and eccentric dipole models for these planets. For Mercury, we implement a thin convecting shell surrounding a solid conducting inner core. For certain Rayleigh numbers, this geometry can produce weak surface magnetic fields that are still in the strong-field regime because the toroidal-poloidal field partitioning that results in these models is different from the Earth-like case. Our numerical models can produce toroidal-poloidal field partitioning similar to that inferred from observations of Mercury's field.

The relationship between convective-region geometry and the morphology of the produced magnetic fields shown here is important in the understanding of these planets' interiors and evolution and may also provide a valuable tool for studying planetary interiors through spacecraft magnetic observations.



# Contents

<b>1</b>	<b>Introduction</b>	<b>1</b>
1.1	Planetary Magnetic Field Representations . . . . .	2
1.2	Observations of Planetary Magnetic Fields . . . . .	4
1.3	Dynamo Theory . . . . .	6
1.3.1	Fluid Flow . . . . .	7
1.3.2	Temperature . . . . .	9
1.3.3	Magnetic Field . . . . .	10
1.3.4	Shell vs. Sphere . . . . .	12
1.4	Numerical Dynamo Modeling . . . . .	14
1.4.1	Kuang and Bloxham Numerical Dynamo Model . . . . .	14
1.4.2	Other Numerical Models . . . . .	16
1.4.3	How Realistic are They? . . . . .	16
<b>2</b>	<b>Uranus and Neptune</b>	<b>19</b>
2.1	Introduction . . . . .	19
2.2	Uranus' and Neptune's Magnetic Fields . . . . .	20
2.2.1	Observations and Models . . . . .	20
2.2.2	A New Field Morphology . . . . .	25
2.2.3	Dynamo Location . . . . .	25
2.3	Explanations for the Anomalous Fields . . . . .	27
2.3.1	Stable Stratification in Uranus and Neptune . . . . .	31
2.4	Dynamos With Solid Inner Cores . . . . .	33
2.4.1	Model Setup . . . . .	33
2.4.2	Surface Magnetic Power Spectra . . . . .	34
2.4.3	Eccentric Dipole Models . . . . .	36
2.4.4	Magnetic Energy . . . . .	38
2.4.5	Kinetic Energy . . . . .	41
2.4.6	Magnetic Field Plots . . . . .	42
2.4.7	Velocity Field Plots . . . . .	45
2.4.8	Summary of Solid Inner Core Models . . . . .	48
2.5	Dynamos With Stably-Stratified Fluid Inner Cores . . . . .	49

2.5.1	Model Setup . . . . .	49
2.5.2	Surface Magnetic Power Spectra . . . . .	53
2.5.3	Eccentric Dipole Models . . . . .	53
2.5.4	Magnetic Energy . . . . .	55
2.5.5	Kinetic Energy . . . . .	56
2.5.6	Magnetic Field Plots . . . . .	61
2.5.7	Velocity Field Plots . . . . .	63
2.5.8	Magnetic Field Intensity . . . . .	63
2.5.9	Summary of Stably-Stratified Inner Region Models . . . . .	65
2.6	Discussion . . . . .	66
2.7	Stable Stratification in Other Dynamos . . . . .	67
2.7.1	Earth . . . . .	68
2.7.2	Saturn . . . . .	68
2.7.3	Sun . . . . .	68
<b>3</b>	<b>Mercury</b>	<b>71</b>
3.1	Introduction . . . . .	71
3.2	Observations of Mercury’s Magnetic Field . . . . .	72
3.3	Mercury’s Thermal History and the State of its Core . . . . .	74
3.4	Magnetic Field Strength Expected From a Dynamo . . . . .	75
3.5	Numerical Model Results . . . . .	78
3.5.1	Toroidal and Poloidal Field Partitioning . . . . .	78
3.5.2	Symmetry of Field Partitioning . . . . .	80
3.5.3	Eccentric Dipole Models . . . . .	81
3.5.4	Axisymmetric Magnetic Field Plots . . . . .	81
3.5.5	Axisymmetric Velocity Field Plots . . . . .	82
3.6	Discussion . . . . .	85
3.6.1	Trends in the Models . . . . .	86
3.6.2	Cause of Non-Earth-like Field Partitioning . . . . .	86
3.6.3	Future Work . . . . .	88
<b>4</b>	<b>Conclusions and Future Work</b>	<b>91</b>
<b>Bibliography</b>		<b>97</b>

# List of Figures

1.1	Canonical forms of toroidal and poloidal fields . . . . .	3
1.2	Surface radial magnetic fields . . . . .	7
1.3	Inner core tangent cylinder . . . . .	13
2.1	Interior structure of Uranus and Neptune . . . . .	21
2.2	Voyager II trajectory . . . . .	23
2.3	Surface magnetic power spectra . . . . .	26
2.4	Jupiter's interior structure . . . . .	28
2.5	Saturn's interior structure . . . . .	29
2.6	Average surface magnetic power spectra . . . . .	35
2.7	Average eccentric dipole models vs. $r_{io}$ . . . . .	36
2.8	Eccentric dipole models vs. time . . . . .	37
2.9	Average non-axisymmetric magnetic energy vs. $r_{io}$ . . . . .	39
2.10	Magnetic energy vs. time for model 1 . . . . .	40
2.11	Magnetic energy vs. time for model 2 . . . . .	40
2.12	Magnetic energy vs. time for model 3. . . . .	41
2.13	Average non-axisymmetric kinetic energy vs. $r_{io}$ . . . . .	42
2.14	Kinetic energy vs. time for model 1 . . . . .	43
2.15	Kinetic energy vs. time for model 2. . . . .	43
2.16	Kinetic energy vs. time for model 3. . . . .	44
2.17	Radial magnetic field . . . . .	45
2.18	Axisymmetric magnetic field . . . . .	46
2.19	Velocity field . . . . .	47
2.20	Axisymmetric temperature perturbation field . . . . .	48
2.21	Dynamo model geometries . . . . .	49
2.22	Background non-dimensional temperature gradient in numerical model . . . . .	51
2.23	Average surface magnetic power spectra . . . . .	52
2.24	Average eccentric dipole models vs. $r_s$ . . . . .	53
2.25	Average eccentric dipole models vs. time . . . . .	54
2.26	Average non-axisymmetric magnetic energy vs. $r_s$ . . . . .	55
2.27	Average magnetic energy in unstable shell vs. $r_s$ . . . . .	56

2.28	Magnetic energy vs. time for model 3 . . . . .	57
2.29	Magnetic energy vs. time for model 7 . . . . .	57
2.30	Magnetic energy vs. time for model 8 . . . . .	58
2.31	Average non-axisymmetric kinetic energy vs. $r_s$ . . . . .	58
2.32	Kinetic energy vs. time for model 3 . . . . .	59
2.33	Kinetic energy vs. time for model 7 . . . . .	60
2.34	Kinetic energy vs. time for model 8 . . . . .	60
2.35	Radial magnetic field . . . . .	61
2.36	Axisymmetric magnetic field . . . . .	62
2.37	Velocity field . . . . .	64
2.38	Axisymmetric temperature perturbation field . . . . .	65
3.1	Mariner 10 trajectory . . . . .	73
3.2	Magnetic field ratios . . . . .	79
3.3	Magnetic energy components for model 6 . . . . .	80
3.4	Magnetic energy components for model 7 . . . . .	81
3.5	Eccentric dipole models vs. time . . . . .	82
3.6	Axisymmetric magnetic field for models 2, 4, 7 and 9 . . . . .	83
3.7	Axisymmetric magnetic field for model 6 . . . . .	84
3.8	Axisymmetric velocity field . . . . .	84
3.9	Axisymmetric temperature perturbation field . . . . .	85
3.10	Sketch of theoretical convective flow patterns . . . . .	87
3.11	Velocity field slices for model 5 . . . . .	89
3.12	Velocity field slices for model 7 . . . . .	90
4.1	Magnetic field structure and the tangent cylinder . . . . .	92
4.2	Dependence of surface power spectra on inner core radius . . . . .	93

# List of Tables

1.1	Highlights of spacecraft missions . . . . .	4
1.2	Eccentric dipole models . . . . .	6
1.3	Summary of current numerical dynamo models . . . . .	18
2.1	Physical properties of Uranus and Neptune . . . . .	20
2.2	$Q_3$ and $O_8$ magnetic field models for Uranus and Neptune respectively . . . . .	22
2.3	Holme and Bloxham magnetic field models for Uranus and Neptune . . . . .	24
2.4	Heat flow parameters for the giant planets . . . . .	31
2.5	Solid inner core model parameters . . . . .	34
2.6	Stably-stratified inner core model parameters . . . . .	51
2.7	Gauss coefficients for model 3 . . . . .	66
3.1	Physical properties of the terrestrial planets . . . . .	71
3.2	Mariner 10 trajectory and magnetic field characteristics . . . . .	72
3.3	Model parameters and results . . . . .	78

*In this world we walk on  
the roof of hell and look  
at the flowers*  
-Issa (1763-1827), Shadowless Ants

# Chapter 1

## Introduction

Of all the planets in this solar system, we know most about the Earth. This is an obvious result of the fact that we live on this planet; it is the one to which we have the easiest access and history of information. Consequently, when studying planetary magnetic fields, we should begin by examining the Earth's field in an effort to understand its characteristics. The geomagnetic field is predominantly dipolar with strong symmetry about its rotation axis, it is long-lived (at least 2 billion years old), has maintained an intensity through time of the same order of magnitude as its current value, and has experienced chaotic reversals in time. If we can determine what these characteristics tell us about the Earth's interior and how representative they are of planetary magnetic fields in general, then magnetic fields can be an important tool in the study of planetary interiors.

Planetary magnetic fields are generated by dynamo action; a process where complex fluid motions in electrically conducting regions of the planets maintain a magnetic field against ohmic decay. By studying magnetic fields, we can learn about basic structural components of the planet: if a planet possesses a magnetic field generated by a dynamo, then it must necessarily contain a fluid electrically conducting region in its interior. We can also discover its basic thermal state: if a planet has an active dynamo then it must necessarily possess a power supply keeping that fluid in motion. Other information one can obtain includes the rotation rate of the planetary interior (important for gaseous planets with no solid surface features to track), the flow structure near the top of the dynamo region (using the secular variation of the field) and, from remanent crustal magnetism: physical/mineralogical properties of crustal rocks (amount of iron), mantle thermal history (plate tectonics) and planet rotational evolution (polar wander).

One characteristic that varies among the planets is magnetic field morphology. The planets in our solar system possess magnetic fields that fall into three categories:

- (I) Axially dipolar dominated fields: Earth, Jupiter, Saturn and Ganymede all fall into this category (Connerney, 1993; Kivelson *et al.*, 1996),
- (II) Non-dipolar, non-axisymmetric fields: Uranus and Neptune are in this category (Ness *et al.*, 1986, 1989),
- (III) Mercury: This planet gets its own category even though the field is axially dipolar dominated because the weak intensity of the observed surface field is inconsistent with the dynamos in category I. Since current observations of Mercury's field cannot distinguish between a remanent crustal or actively generated field (Stevenson, 1987; Aharonson *et al.*, 2004), the

existence of this category relies on the assumption that the observed field is dynamo generated.,

These different morphologies are not categorized strictly according to planet composition or structure since Jupiter, the planet least like Earth in composition and size, possesses a magnetic field most similar to Earth, whereas Venus, the planet most like Earth in composition and size, possesses a magnetic field least like it (in the sense that it has none). It therefore appears that other factors determine magnetic field morphology.

Over the past decade, numerical models developed to study the Earth's dynamo have been successful at reproducing many of the characteristic features of its magnetic field; most notably, the field's axially dipolar dominance. It appears that numerical dynamo models can readily produce magnetic fields seen in category I planets. The purpose of this thesis is to examine what factors might lead to magnetic field morphologies in categories II and III. One possible difference between the planets in the three categories is the geometry of their convecting regions (i.e. the relative size of the inner and convecting outer core, and the physical state (fluid vs. solid) of the inner core). In this work, we implement interior geometries that are suitable for the planets in categories II and III in numerical dynamo models to examine whether the magnetic fields produced in these geometries are consistent with the observations of these planets.

In chapter 1, we review magnetic field representations in insulators and conductors, observations of planetary magnetic fields, dynamo theory and numerical dynamo modeling. In chapter 2 we discuss Uranus' and Neptune's fields, chapter 3 deals with Mercury's field and finally, in chapter 4, we discuss future work and the possible implications of this work for other planetary fields.

## 1.1 Planetary Magnetic Field Representations

Assuming the source of the magnetic field is internal to the planet, the magnetic field  $\mathbf{B}$  outside the generation region (i.e. in an insulator) is irrotational ( $\nabla \times \mathbf{B} = 0$ ) and can therefore be represented as the gradient of a scalar potential ( $\mathbf{B} = \nabla\Phi$ ). From Maxwell's equations we know the magnetic field is divergence-free ( $\nabla \cdot \mathbf{B} = 0$ ) and therefore that the scalar potential satisfies Laplace's equation ( $\nabla^2\Phi = 0$ ). In planetocentric spherical coordinates  $(r, \theta, \phi)$ , the potential is given by

$$\Phi = a \sum_{l=1}^{\infty} \left(\frac{a}{r}\right)^{l+1} \sum_{m=0}^l P_l^m(\cos\theta) [g_l^m \cos(m\phi) + h_l^m \sin(m\phi)], \quad (1.1)$$

where  $a$  is the planetary radius,  $g_l^m$  and  $h_l^m$  are the Gauss coefficients and  $P_l^m$  are associated Legendre polynomials, Schmidt normalized so that

$$\int_{\phi=0}^{2\pi} \int_{\theta=0}^{\pi} (P_l^m(\cos\theta) \cos m\phi)^2 \sin\theta d\theta d\phi = \frac{4\pi}{2l+1}. \quad (1.2)$$

In the dynamo generation region (i.e. in a conductor) the field is no longer irrotational since Maxwell's equations give  $\nabla \times \mathbf{B} = \mu_0 \mathbf{J}$ . However it is still divergence-free which allows for the toroidal-poloidal decomposition in spherical coordinates:

$$\mathbf{B} = \mathbf{B}_T + \mathbf{B}_P = \nabla \times T_B \hat{\mathbf{r}} + \nabla \times (P_B \hat{\mathbf{r}}), \quad (1.3)$$

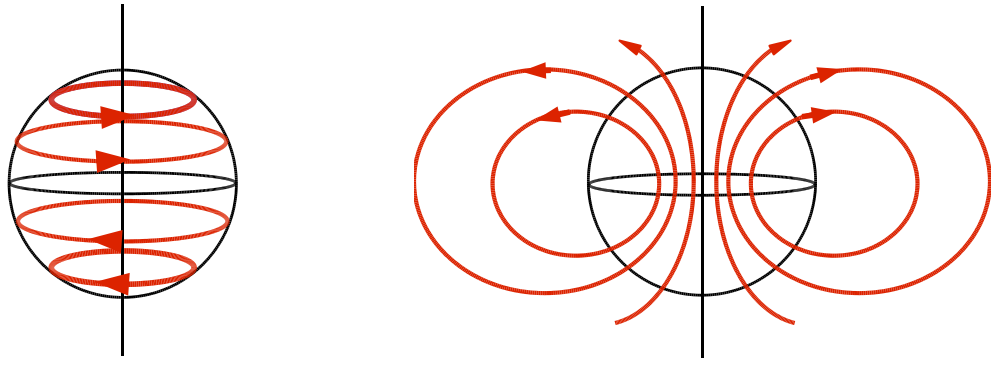


**Figure 1.1:** Canonical forms of toroidal (left) and poloidal (right) fields. Red curves are magnetic field lines, the black sphere is the boundary of the dynamo generation region and the black vertical line represents the rotation axis.

where  $\mathbf{B}_T$  and  $\mathbf{B}_P$  are the toroidal and poloidal field components respectively,  $T_B$  and  $P_B$  are the toroidal and poloidal scalars respectively and  $\hat{\mathbf{r}}$  is a unit vector in the radial direction. Canonical forms of the toroidal and poloidal fields are shown in Figure 1.1. Since the toroidal field has no radial component, it is not observable outside the dynamo generation region which means that spacecraft only observe the poloidal component of the field. This is a fundamental problem when studying planetary magnetic fields since we can only ever observe the poloidal field directly and it is believed the toroidal field may actually be the dominant field in the core.

Each spherical harmonic degree  $l$  and order  $m$  component in equation 1.1 represents a different basis function for of the field. For example, the three  $l = 1$  terms represent the dipolar components of the field. The  $l = 1, m = 0$  term is the axisymmetric dipole and the  $l = 1, m = 1$  term is the equatorial dipole. Higher degree terms such as  $l = 2$  (quadrupole) and  $l = 3$  (octupole) represent components with smaller length scales. The  $m = 0$  terms all represent the axisymmetric components of the field whereas higher order terms represent non-axisymmetric components.

## 1.2 Observations of Planetary Magnetic Fields

Spacecraft have observed the magnetic fields of all the planets in our solar system but Pluto, as well as the Earth's moon and the Galilean satellites. Table 1.1 lists these various missions for each planetary body. Clearly the amount of data from each planet varies as some have only been visited by one flyby mission whereas others have had multiple orbiters. Of the bodies visited, Venus, Europa, Callisto and possibly Io (difficult because it is so deeply embedded in the Jovian magnetosphere) do not exhibit an intrinsic magnetic field. Some of these bodies do however exhibit induced fields due to external currents. For example, Europa and Callisto exhibit a response to the Jovian magnetosphere most likely due to internal salty water oceans (Kivelson *et al.*, 1999; Khurana *et al.*, 1998).

For the planetary bodies with intrinsic fields, the sources of the fields fall into two categories:

- (a) Active dynamo generated fields: Earth, Jupiter, Saturn, Ganymede and possibly Mercury
- (b) Remanent crust fields due to past dynamo action: Earth, Moon, Mars and possibly Mercury.

**Table 1.1:** Highlights of spacecraft missions that have studied planetary magnetic fields.

Planet	Spacecraft	Years	Orbital Type
Mercury	Mariner 10	1974-1975	2 flybys
Venus	Mariners 2,5,10	1962,1967,1974	flybys
	Venera 4,9,10	1967,1975,1975	probe, orbiters
	Pioneer Venus	1979-1981	orbiter
	Magellan	1990-1994	orbiter
Earth	MagSat	1979-1980	orbiter
	Ørsted	1999-	orbiter
	Champ	2000-	orbiter
	Ørsted-2	2001-	orbiter
Moon	Lunar Prospector	1998-1999	orbiter
Mars	Mars Global Surveyor	1997-	orbiter
Jupiter	Pioneer 10,11	1973,1974	flybys
	Voyager I	1979	flyby
	Voyager II	1979	flyby
	Galileo	1995-2003	orbiter
Galilean Moons	Galileo	1995-2003	orbiter
Saturn	Pioneer 11	1980	flyby
	Voyager I	1981	flyby
	Voyager II	1981	flyby
	Cassini	2004-	orbiter
Uranus	Voyager II	1986	flyby
Neptune	Voyager II	1989	flyby

---

Spacecraft magnetic observations either measure the total intensity of the field (scalar data), or they measure the field in three orthogonal directions (vector data) which is much more useful in determining field morphology. The magnetic field data combined with positional data of the spacecraft can be used with equation 1.1 to solve an inverse problem in order to obtain the Gauss coefficients from the magnetic field data. This then provides an observational model for the magnetic field. A problem automatically arises as the infinite number of Gauss coefficients in the expansion for the magnetic potential cannot be calculated from an unavoidably finite number of observations, and truncation of the series is necessary at some degree and order. The truncation level should be large enough to adequately represent the field without being so large as to introduce more free parameters than can be determined accurately from the observations.

In terms of the Gauss coefficients, the power ( $\Psi$ ) in the magnetic field can be defined as the mean square field intensity:

$$\Psi = \sum_{l=1}^{\infty} (l+1) \left(\frac{a}{r}\right)^{2l+4} \sum_{m=0}^l [(g_l^m)^2 + (h_l^m)^2]. \quad (1.4)$$

Since the power in the higher degree components of the field are attenuated more strongly with distance from the source than the lower degree components (i.e. power scales as  $r^{-(2l+4)}$ ), spacecraft preferentially observe the lower degree components of the field. This affects the determination of

**Table 1.2:** Eccentric dipole models for the planets with active dynamos. Data from Connerney (1993).

Planet	Dipole Tilt (degrees)	Dipole Offset (radii)
Earth	11.2	0.076
Jupiter	9.4	0.119
Saturn	0.0	0.038
Uranus	58.6	0.352
Neptune	46.9	0.485

---

the basic field morphology if high spatial resolution of the field is not available, which is the case for all the planets but Earth and Mars. Other factors that affect the ability of observations to determine morphology include the accuracy and resolution of the magnetometer and any external fields present. For example, it was possible to determine some quadrupole and octupole components at Uranus and Neptune from one flyby, whereas the two flybys of Mercury were only able to determine the dipole component to within a factor of 2. This is because the interplanetary magnetic field (IMF) in the vicinities of Uranus and Neptune is much weaker since they are farther from the Sun.

For the planets with active dynamos (excluding Earth), we only have observations of the low degree components of these fields for the reasons mentioned above. In order to compare the large scale (low degree) structure of these fields, one possibly useful representation is the eccentric dipole model. In this model, the field is assumed to consist only of a dipole that has some tilt with respect to the rotation axis and is offset from the planetary center by some amount. The tilt of the dipole is determined by the ratio of the axial to equatorial dipole and the offset of the dipole from the planet center is a measure of the size of the quadrupole component relative to the dipole component. Table 1.2 lists the eccentric dipole tilts and offsets for the planets with active dynamos. Mercury and Ganymede are not included here since the data are not good enough to determine the eccentric dipole models. The differences in the axially-dipolar dominated fields (small tilts and offsets) and the non-dipolar, non-axisymmetric fields (large tilts and offsets) is evident.

Eccentric dipole models allow a decent visualization of the field for dipolar-dominated fields, but since they do not take into account higher degree structure, they aren't in general, good characterizations of non-dipolar fields. Another easy way to visualize the fields is with a plot of the radial component at the planets' surfaces (Figure 1.2). Dipole dominance is evident in the plots with one color of field (i.e. one direction) in one hemisphere and the other color (opposite direction) in the other hemisphere. One can visualize the field lines as emanating from one hemisphere and entering the other hemisphere. Axisymmetry is evident in the plots when the field doesn't vary significantly along a latitude circle. Non-dipolar, non-axisymmetric fields display a more complex field pattern with multiple magnetic equators (lines of zero radial field) and field variation with latitude.

### 1.3 Dynamo Theory

Clearly this is a vast topic that will not be covered here in any sort of detail that would give it justice. This section will cover the basic ideas and some important concepts that will be needed in later chapters. For a more thorough treatment, we suggest Braginsky and Roberts (1995), Fearn (1998) and Roberts and Glatzmaier (2000a).

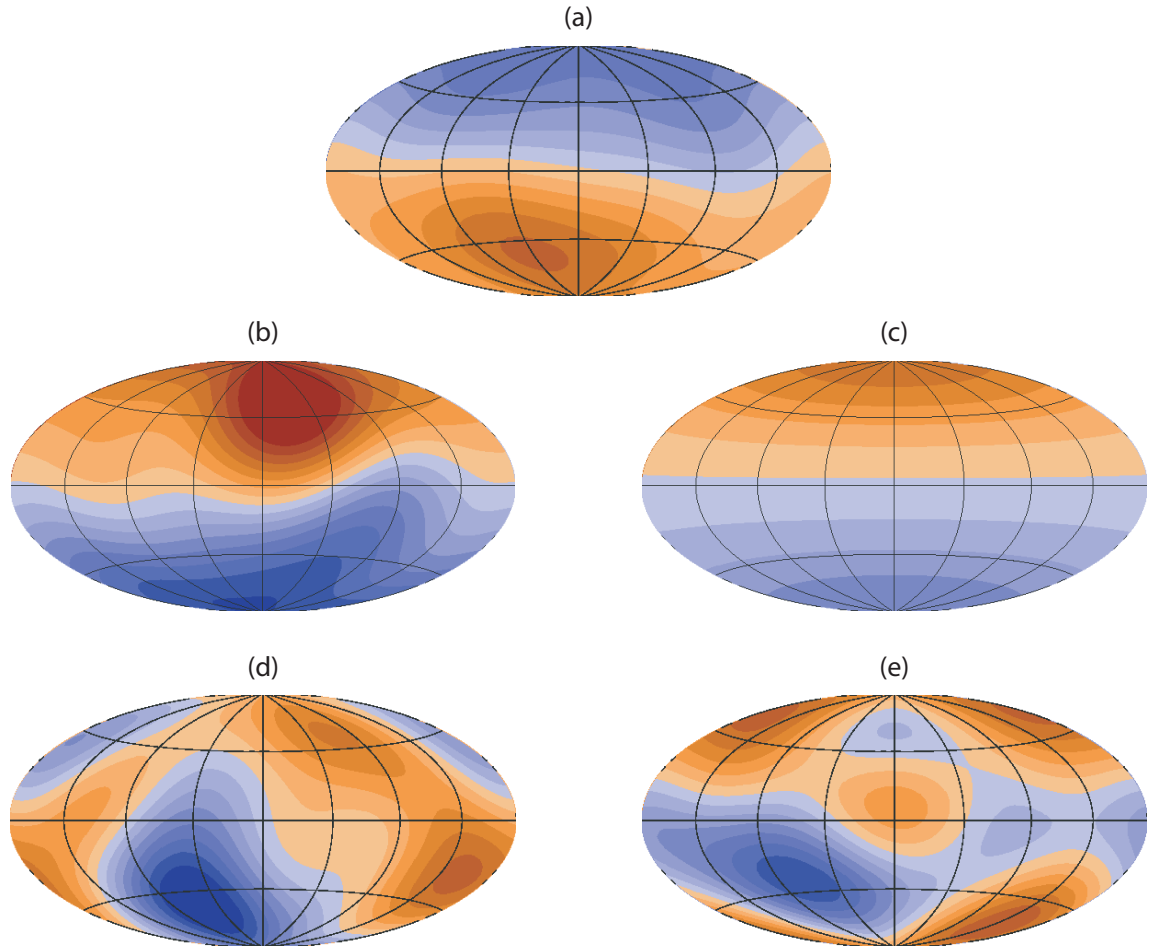


**Figure 1.2:** Surface radial magnetic fields for Earth (a), Jupiter (b), Saturn (c), Uranus (d) and Neptune (e). Orange and blue colors represent different field directions. For the gaseous planets, the surface is taken to mean the 1 bar pressure level. Data from Merrill *et al.* (1996) for Earth, Connerney (1993) for Jupiter and Saturn, and Holme and Bloxham (1996) for Uranus and Neptune.

The physical mechanism for dynamo action is as follows: the motion of an electrically conducting fluid with velocity  $\mathbf{v}$  in the presence of a magnetic field  $\mathbf{B}$  results in the generation of a current density  $\mathbf{J}$  which, through Ampère's law creates a magnetic field:

$$\mathbf{J} = \frac{1}{\mu_0} \nabla \times \mathbf{B}, \quad (1.5)$$

where  $\mu_0$  is the magnetic permeability of free space. This magnetic field can modify the fluid motion through the Lorentz force (per unit mass):

$$\mathbf{F}_\mathbf{B} = \frac{1}{\rho} \mathbf{J} \times \mathbf{B}, \quad (1.6)$$

which can then generate a new current density  $\mathbf{J}$  and so on. A dynamo is successful if this cycle is

able to maintain the magnetic field against ohmic decay.

In planetary cores, the fluid motion that drives the dynamo comes from convection which results from the core's removal of heat. Hence, dynamo generation involves the evolution of the velocity, magnetic, and energy fields. One important characteristic of the planetary dynamo problem is the rapid rotation of planetary cores which means the Coriolis force is a dominant component of the dynamics. Other important characteristics include the spherical geometry of the core and the radial gravity force. In the following sections we introduce the equations governing the dynamo problem, as well as the approximations we shall use in our numerical dynamo modeling. We shall remove a hydrostatic, adiabatic reference state from the equations and assume that the fluid is compositionally homogeneous in our discussion (for equations including compositional differences, see Roberts and Glatzmaier (2000a)).

### 1.3.1 Fluid Flow

Fluid flow is governed by two equations:

Conservation of Mass:

$$\frac{\partial \rho}{\partial t} + \nabla \cdot (\rho \mathbf{v}) = 0 \quad (1.7)$$

and the Momentum Equation:

$$\rho \left( \frac{\partial}{\partial t} + \mathbf{v} \cdot \nabla \right) \mathbf{v} + 2\rho \Omega \times \mathbf{v} = -\nabla p + \rho \mathbf{g} + \rho v \nabla^2 \mathbf{v} + \frac{1}{3} \rho v \nabla (\nabla \cdot \mathbf{v}) + \mathbf{J} \times \mathbf{B} \quad (1.8)$$

where  $\rho$  is fluid density,  $t$  is time,  $\mathbf{v}$  is fluid velocity,  $\Omega$  is the planetary rotation rate (assumed constant),  $p$  is the modified pressure which includes the centrifugal force,  $\mathbf{g}$  is the gravity vector and  $v$  is the kinematic viscosity. To simplify the equations somewhat, we make use of the Boussinesq approximation which assumes that the fluid is incompressible except for its effects on thermal buoyancy. This reduces equations 1.7 and 1.8 respectively to:

$$\nabla \cdot \mathbf{v} = 0 \quad (1.9)$$

and

$$\rho_0 \left( \frac{\partial}{\partial t} + \mathbf{v} \cdot \nabla \right) \mathbf{v} + 2\rho_0 \Omega \times \mathbf{v} = -\nabla p + \Delta \rho \mathbf{g} + \rho_0 v \nabla^2 \mathbf{v} + \mathbf{J} \times \mathbf{B} \quad (1.10)$$

where  $\rho_0$  is the constant average fluid density and  $\Delta \rho$  is the density variation. Since we are only considering thermal buoyancy, we can write the density variation in terms of the temperature perturbation ( $\Delta \rho = -\rho_0 \alpha_T \Theta$ , where  $\alpha_T$  is the coefficient of thermal expansion and  $\Theta$  is the temperature perturbation about the background state). The two terms on the left of equation 1.10 represent the inertial and Coriolis forces respectively; on the right hand side of the equation we have the pressure gradient, buoyancy, viscous and Lorentz forces respectively.

### Convection Without a Magnetic Field

In this section we will begin to examine the dynamo problem by studying the fluid motions in a planetary core without the presence of a magnetic field (*i.e.* we eliminate the Lorentz force from equation 1.10). The leading order force balance in the momentum equation for the planets, known

as geostrophic balance, is between the Coriolis and pressure terms:

$$2\rho_0\Omega \times \mathbf{v} = -\nabla p. \quad (1.11)$$

By taking the curl of this equation, and using equation 1.9, one obtains an important result known as the Proudman-Taylor theorem (Proudman, 1916; Taylor, 1917):

$$\frac{\partial \mathbf{v}}{\partial z} = 0 \quad (1.12)$$

where  $z$  is the coordinate in the direction of the rotation axis. This means that in the spherical geometry of the core, the main force balance requires that fluid motions are constrained to cylinders coaxial with the rotation axis (called Taylor columns) of constant height in the  $z$  direction. This is one type of zonal flow in planets.

Since convective motions must transport heat radially, they cannot exactly satisfy the Taylor-Proudman theorem, but they do satisfy it to leading order such that, in cylindrical coordinates  $(s, \phi, z)$ , derivatives in the  $z$  direction are much smaller than derivatives in the  $s$  and  $\phi$  directions. This constraint leads to larger critical Rayleigh numbers for the onset of convection in rotating spheres than in the non-rotating case. Near onset, linear theory predicts convection in the form of simple rolls (Busse rolls) parallel to the rotation axis (Roberts, 1968; Busse, 1970; Jones *et al.*, 2000; Busse and Carrigan, 1976; Zhang, 1992).

The regime of fluid flow in planetary cores is most likely highly supercritical and the near-critical linear analysis which predicts Busse rolls is no longer valid. However, numerical studies (Ardes *et al.*, 1997; Tilgner and Busse, 1997; Grote *et al.*, 2000b; Aurnou and Olson, 2001; Christensen, 2001; Grote and Busse, 2001; Christensen, 2002) show that in general, at supercritical Rayleigh numbers, the flow maintains a similarity to the Busse rolls with the possible addition of strong zonal flows (there are exceptions in certain parameter regimes (Zhang, 1992, 1994, 1995)). These zonal flows arise from the non-linear inertial term  $\mathbf{v} \cdot \nabla \mathbf{v}$  in the momentum equation because the curvature of the outer boundary of the sphere causes a tilt of the convection columns, which leads to a correlation of the azimuthal and cylindrically-radial velocities (Busse, 1983, 1994).

The buoyancy term in the momentum equation can also lead to another form of motion known as a thermal wind. Balancing the Coriolis and buoyancy forces gives:

$$2\Omega \times \mathbf{v} = -\alpha_T \Theta \mathbf{g}. \quad (1.13)$$

By taking the curl of both sides and using equation 1.9 we get:

$$\frac{\partial \mathbf{v}}{\partial z} = -\frac{\alpha_T}{2\Omega} \mathbf{g} \times \nabla \Theta, \quad (1.14)$$

which implies that if the temperature perturbation gradients in the core are not in the same direction as gravity (the spherical-radial direction), then motion will occur.

The viscous term in equation 1.10 is very small compared to the Coriolis force except in thin boundary layers at the inner and outer core boundaries. The inertial term is also small, but allows for time dependence as well as the Reynold's stresses mentioned earlier. In the above analysis, buoyancy was assumed to be only due to thermal effects. If compositional differences exist, say a two-component fluid, they can be incorporated through a new variable, the concentration of light element ( $\xi$ ) which then appears in equation 1.10 identically as the temperature variable, except  $\alpha_T$  is

replaced by the compositional expansion coefficient. Since its treatment is identical to temperature, we shall avoid adding this complication in the following sections.

### 1.3.2 Temperature

The buoyancy force in the momentum equation includes the temperature perturbation  $\Theta$  which is governed by the heat equation with the conductive solution removed:

$$\left( \frac{\partial}{\partial t} - \kappa \nabla^2 \right) \Theta = -\mathbf{v} \cdot (T_0(r) + \Theta) + Q \quad (1.15)$$

where  $\kappa$  is the thermal diffusivity,  $T_0(r)$  is the conductive temperature solution and  $Q$  represents internal heat sources or secular cooling.

### 1.3.3 Magnetic Field

When a magnetic field is added to the picture, an equation governing magnetic field generation is needed. Since the fluid velocity  $v \ll c$  (the speed of light) we can use the magnetohydrodynamic (MHD) approximation when studying the magnetic fields. This means that we can neglect the displacement current in Ampere's law which then reduces to

$$\nabla \times \mathbf{B} = \mu_0 \mathbf{J}. \quad (1.16)$$

To derive our needed equation we begin with Ohm's law:

$$\mathbf{J} = \sigma \mathbf{E} + \sigma \mathbf{v} \times \mathbf{B} \quad (1.17)$$

where  $\sigma$  is electrical conductivity and  $\mathbf{E}$  is the electric field. Taking the curl of Ohm's law gives:

$$\nabla \times \mathbf{J} = \sigma (\nabla \times \mathbf{E} + \nabla \times (\mathbf{v} \times \mathbf{B})). \quad (1.18)$$

Using Ampere's law to substitute for  $\mathbf{J}$  on the left hand side of this equation, and Faraday's law ( $\nabla \times \mathbf{E} = -\frac{\partial \mathbf{B}}{\partial t}$ ) to substitute for  $\mathbf{E}$  on the right hand side of the equation gives

$$\nabla \times (\nabla \times \mathbf{B}) = -\mu_0 \sigma \frac{\partial \mathbf{B}}{\partial t} + \mu_0 \sigma \nabla \times (\mathbf{v} \times \mathbf{B}) \quad (1.19)$$

Using the vector identity  $\nabla \times (\nabla \times \mathbf{B}) = \nabla(\nabla \cdot \mathbf{B}) - \nabla^2 \mathbf{B}$  along with Gauss' law ( $\nabla \cdot \mathbf{B} = 0$ ), we obtain our needed equation, known as the magnetic induction equation:

$$\frac{\partial \mathbf{B}}{\partial t} = \nabla \times (\mathbf{v} \times \mathbf{B}) + \eta \nabla^2 \mathbf{B} \quad (1.20)$$

where  $\eta = (\sigma \mu_0)^{-1}$  is the magnetic diffusivity. The first term on the right hand side of the equation describes the advection and hence generation of magnetic field and the second term is the diffusion component.

In a successful dynamo, the field is maintained against diffusion which implies that the first term on the right hand side of equation 1.20 must be larger than the second term. The ratio of the sizes

of these two terms is called the Magnetic Reynolds number:

$$Re_M = \frac{|\nabla \times (\mathbf{v} \times \mathbf{B})|}{|\eta \nabla^2 \mathbf{B}|} \approx \frac{UL}{\eta} \quad (1.21)$$

where  $U$  and  $L$  are characteristic velocity and length scales respectively. Theoretical analysis has shown that in general,  $Re_M \geq 10$  approximately, is necessary for dynamo action to occur.

## Weak and Strong Field Regimes

As mentioned in section 1.3.1, the rapid rotation of the planetary core inhibits convective motions since they do not obey the Proudman-Taylor constraint. This constraint was a result of the leading order balance in the momentum equation in the absence of magnetic fields. If magnetic fields are present, then the Lorentz force in the momentum equation can either be one of the dominant terms in the equation (i.e. it can balance the Coriolis force) or it can be a secondary term that does not participate in the leading order balance. If it is a leading order term, the dominant force balance in the core is called magnetostrophic:

$$2\Omega \times \mathbf{v} = -\nabla p + \frac{1}{\rho} \mathbf{J} \times \mathbf{B}. \quad (1.22)$$

In this case, not only does the velocity field generate magnetic field, but the magnetic field can affect or generate velocity field and the dynamics is said to be in the 'strong field regime'. Since the Lorentz force can balance the Coriolis force, convection is not necessarily inhibited, which means that the presence of a strong magnetic field can aid in generating convective motions in a rapidly rotating core. In a more philosophical description, the planet wants to be in a strong field regime since then the magnetic field can then aid in the cooling of the planet.

If the Lorentz force is not in the dominant force balance, then geostrophic balance holds, and the magnetic field can be considered more as a byproduct of fluid motion and does not significantly affect the velocity field or aid in convection. This is known as the 'weak field regime' and the magnetic field is generally much smaller in magnitude in this case.

The ratio of the size of magnetic and Coriolis forces is given by the Elsasser number:

$$\Lambda = \frac{|\rho^{-1} \mathbf{J} \times \mathbf{B}|}{|2\Omega \times \mathbf{v}|} \approx \frac{B^2}{2\Omega \rho \mu_0 \eta} \quad (1.23)$$

where we have used equation 1.5, and  $B$  is a characteristic magnetic field strength. By definition, an Elsasser number of  $O(1)$  is needed for a strong-field dynamo and an Elsasser number much less than  $O(1)$  is the result of a weak field dynamo. It is unclear whether the Elsasser number can be much larger than  $O(1)$  since in this case, there would be no balance between the Coriolis and Lorentz forces, and the magnetic field would take on an inhibiting role for convection since the fluid needs to work against the Lorentz force. One could imagine that this is an unstable situation since the large magnetic field, which is a result of strong convective motions would then diminish the strong convective motions, thereby destroying the large magnetic field.

## Magnetic Field Generation Mechanisms

As seen in section 1.1 the magnetic field in a planetary core can be decomposed into its toroidal ( $\mathbf{B}_T$ ) and poloidal ( $\mathbf{B}_P$ ) components. In an incompressible fluid, the velocity can also be represented in a toroidal-poloidal decomposition:

$$\mathbf{v} = \mathbf{v}_T + \mathbf{v}_P = \nabla \times T_v \hat{\mathbf{r}} + \nabla \times (\nabla \times P_v \hat{\mathbf{r}}) \quad (1.24)$$

where  $\mathbf{v}_T$  and  $\mathbf{v}_P$  are the toroidal and poloidal velocity components respectively, and  $T_v$  and  $P_v$  are the toroidal and poloidal velocity scalars respectively. In this section we outline some basic interactions between velocity and magnetic fields that can generate magnetic field in the dynamo process.

An important process in magnetic field generation is the conversion of toroidal magnetic field to poloidal magnetic field and vice versa. Both poloidal and toroidal velocities can produce toroidal magnetic field from poloidal field, however only poloidal velocities can generate poloidal magnetic field from toroidal field (*i.e.* toroidal velocities cannot generate poloidal from toroidal field). We refer you to Bullard and Gellman (1954) for a detailed discussion of the individual interactions. Here we describe a few simple processes for the conversion of one field to the other that are believed to be important in planetary cores.

Two main motions present in planetary cores are differential rotation (a form of geostrophic flow) and convective upwellings. Differential rotation, a toroidal flow, can generate toroidal field by shearing poloidal field. This process is known as the ' $\omega$  effect'. Convective upwellings can generate poloidal from toroidal field, as well as toroidal from poloidal field. These processes are known as ' $\alpha$  effects' (the name comes from mean field dynamo theory). If the  $\omega$  effect is the dominant producer of toroidal field, then the dynamo is known as an ' $\alpha\omega$  dynamo', if the  $\alpha$  effect is the dominant toroidal field producer, then it is called an ' $\alpha^2$  dynamo', and if both processes are equally important, then it is an ' $\alpha^2\omega$ ' dynamo. Which sort of dynamo operates in planetary cores is unknown.

### 1.3.4 Shell vs. Sphere

The Earth possesses a solid inner core whose radius is about 0.35 the total core radius. Although the inner core occupies a small volume of the total core volume (about 4%), it can affect the dynamo process. No direct detection of solid inner cores has been possible so far in other planets, but thermal evolution models suggest it is possible for other planets to have solid inner cores as well. We will discuss these planets in the following chapters.

A solid inner core has two effects on the dynamo. First, it presents a barrier to fluid flow, thereby having a dynamical consequence: the flow structure in the core must accommodate the presence of the inner core boundary. This not only results in a restriction of flow past the center of the sphere, but because of the Proudman-Taylor constraint, perhaps a more important consequence involves the formation of the inner core tangent cylinder which is the cylinder coaxial with the rotation axis and tangent to the inner core boundary (see Figure 1.3). This cylinder provides a barrier to flow and separates the core into three dynamical regimes: (a) The region outside the tangent cylinder, (b) the region in the tangent cylinder northward of the equator, and (c) the region inside the tangent cylinder southward of the equator.

The second effect of the inner core is a result of its conductivity. The equation governing the magnetic field in a solid conducting inner core is the magnetic diffusion equation:

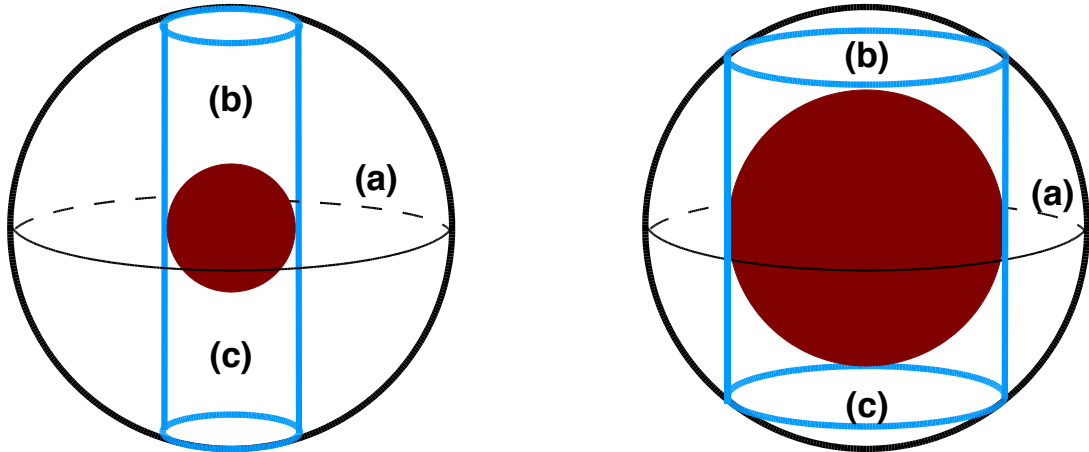


**Figure 1.3:** Sketch of inner core tangent cylinder in a thick (left) and thin (right) shell geometry showing the different dynamical regions of the core. The solid inner core is the red sphere at the centers of the figures, the inner core tangent cylinder is the blue cylinder, the outer bounding sphere is the core-mantle boundary, the region outside the tangent cylinder is marked (a), and the two regions inside the tangent cylinder are marked (b) and (c).

---

$$\frac{\partial \mathbf{B}}{\partial t} = \frac{1}{\sigma\mu} \nabla^2 \mathbf{B}. \quad (1.25)$$

A conducting inner core can contain magnetic field that has diffused into it from the fluid outer core. If the inner core is insulating, then the magnetic field is merely the potential field extension of the field at the inner core boundary. Hollerbach and Jones (1993a,b, 1995) studied the effect of the conductivity of Earth's inner core on the dynamo. By comparing axisymmetric mean-field dynamo models with conducting and insulating cores, they determined that a conducting inner core can have a stabilizing effect on the polarity of the field not seen in models with insulating inner cores. In models with an insulating inner core, the fields were observed to reverse more often than in models with a conducting inner core. This is due to the fact that the magnetic field which threads the conducting inner core is approximately frozen into it, only able to change via diffusion. This is a much slower process than the advection which is generating fluctuations in the field in the outer core and therefore, adds stability to the field. If a fluctuation in the outer core is to cause the magnetic field to reverse, then it must be sufficiently large, and last long enough to change the field in the inner core as well. Hence, small fluctuations in the outer core cannot affect the field polarity in dynamos with conducting inner cores, however they can affect dynamos with insulating inner cores. The extent to which the conductivity of the core can affect the field has been debated recently by Wicht (2002) using 3-D numerical dynamo modeling.

Due to the dynamical and conductivity effects of solid cores, the size of the inner core may have an effect on the morphology of magnetic fields produced. Geometries with larger inner cores will have a larger barrier to flow and larger tangent cylinders (evident in Figure 1.3). Additionally, a relatively larger proportion of field may thread the inner core affecting the stability of the field. These processes will be discussed in the following chapters.

## 1.4 Numerical Dynamo Modeling

We will limit our discussion in this section to three-dimensional, self-consistent numerical dynamo models operating in spherical geometries (i.e. no kinematic, mean field or planar layer dynamos). The different numerical models developed by various groups over the past decade use different approximations, work in different parameter regimes and/or use different boundary conditions, but their general approach is the same. They solve the equations governing magnetic field generation in the core and evolve the system in time to study the evolution of the field.

### 1.4.1 Kuang and Bloxham Numerical Dynamo Model

In this thesis we use the Kuang and Bloxham 3-dimensional numerical dynamo model (Kuang and Bloxham, 1997, 1999) to study magnetic field generation in a spherical, rotating, Boussinesq, electrically conducting fluid shell surrounding a solid inner core. We non-dimensionalize the governing equations (1.10, 1.15 and 1.20) by using the radius of the core ( $r_o$ ) as a length scale, the magnetic diffusion time ( $\tau = r_o^2/\eta$ ) as a time scale, a magnetostrophic balance estimate  $B = \sqrt{2\Omega\rho\mu_0\eta}$  as the magnetic field scale and  $h_T r_o$  (where  $h_T$  is the incoming heat flux at the inner core boundary) as a temperature scale to obtain:

Momentum Equation:

$$Ro \left( \frac{\partial}{\partial t} + \mathbf{v} \cdot \nabla \right) \mathbf{v} + \hat{\mathbf{z}} \times \mathbf{v} = -\nabla p + \mathbf{J} \times \mathbf{B} + \frac{Ra}{(1-r_{io})^2} \Theta \mathbf{r} + E(1-r_{io})^2 \nabla^2 \mathbf{v}, \quad (1.26)$$

Magnetic Induction Equation:

$$\left( \frac{\partial}{\partial t} - \nabla^2 \right) \mathbf{B} = \nabla \times (\mathbf{v} \times \mathbf{B}), \quad (1.27)$$

Heat Equation:

$$\left( \frac{\partial}{\partial t} - q_k \nabla^2 \right) \Theta = -\mathbf{v} \cdot \nabla [T_0(r) + \Theta], \quad (1.28)$$

where  $\hat{\mathbf{z}}$  is a unit vector in the direction of the rotation axis. All other variables have been defined in previous sections.

The non-dimensional parameters in the above equations are the magnetic Rossby number  $Ro$ , the Ekman number  $E$ , the ratio of the inner to total core radius  $r_{io}$ , the Rayleigh number  $Ra$  and the magnetic Prandtl number  $q_k$  which are given by:

$$Ro \equiv \frac{\eta}{2\Omega r_o^2}, \quad (1.29)$$

$$E \equiv \frac{\nu}{2\Omega r_o^2 (1-r_{io})^2}, \quad (1.30)$$

$$r_{io} \equiv \frac{r_i}{r_o}, \quad (1.31)$$

$$Ra \equiv \frac{\alpha_T g_o h_T r_o^2 (1-r_{io})^2}{2\Omega\eta}, \quad (1.32)$$

$$q_\kappa \equiv \frac{\kappa}{\eta}, \quad (1.33)$$

where  $g_o$  is the gravitational acceleration at  $r_o$ . The term  $r_o(1 - r_{io})$  is just the fluid outer core shell thickness ( $d = r_o - r_i$ ) written in terms of our control parameters.

We use fixed heat flux boundary conditions on the temperature, impenetrable and viscous stress-free boundary conditions on the velocity, and finite electrically conducting boundary conditions on the magnetic field. In this thesis, our spherical harmonic expansion goes out to degree 33 and order 21 which are high enough so our solutions are fully converged. In order to work at highly super-critical Rayleigh numbers (appropriate for planetary cores), we employ hyperdiffusivities similar to Kuang and Bloxham (1999). For further information on the approximations and numerical method, refer to Kuang and Bloxham (1999).

Due to our choice of length scale in the non-dimensionalization, the buoyancy term scales with the non-dimensional grouping  $Ra/(1 - r_{io})^2$  which we shall call the modified Rayleigh number ( $Ra_m$ ) and the viscous term scales with  $E(1 - r_{io})^2$  which we shall refer to as the modified Ekman number  $E_m$ . In Kuang and Bloxham (1999), the non-dimensionalization is slightly different since the Rayleigh and Ekman numbers are defined in terms of the total core radius instead of the outer core shell thickness as is done here. The choice presented here is more appropriate for our models since we shall vary the shell thickness and  $d$  can be quite different from  $r_o$ . In Kuang and Bloxham (1999) the inner core is kept fixed at  $r_{io} = 0.35$  and is relatively small making the definitions used there appropriate for that study.

The non-dimensional numbers can vary between the models. In all our models we use  $Ro = E_m = 2 \times 10^{-5}$  and  $q_\kappa = 1$ . This choice implies that all the Prandtl numbers in the system (i.e. all the possible ratios of kinematic viscosity, magnetic and thermal diffusivity) are equal to 1. In real planetary cores, if molecular values are used for the diffusivities, the magnetic diffusivity is much larger than the other diffusivities, however, if we assume turbulent eddies are the main diffusive mechanism, then it is more realistic to take all the diffusivities equal to each other, which we have done. Values for  $r_{io}$  and  $Ra_m$  vary in our models and we will specify their values when discussing specific models in the following chapters.

### 1.4.2 Other Numerical Models

The first 3-D spherical dynamo models were developed to study the solar dynamo (Gilman and Miller, 1981; Gilman, 1983; Glatzmaier, 1984, 1985a,b). A decade later, models were designed to study the geodynamo. In Table 1.3 we list the parameters, approximations and boundary conditions of several numerical geodynamo models. Only models that are fully three-dimensional, in spherical geometry, and fully dynamical are listed. References are also given to studies involving the various models. Other models for studying magnetic field generation that are simpler computationally include kinematic dynamo models, mean-field dynamo models and 2.5-dimensional dynamo models.

### 1.4.3 How Realistic are They?

Although the numerical models in the last section can reproduce many of the characteristics of planetary dynamos, none of them work in the parameter regime of planetary cores because of computational constraints. Using molecular values for the viscosity, the Ekman number in the Earth's

core is about  $10^{-15}$ . This value is 10 orders of magnitude smaller than the values used in the models. In order to work in the appropriate parameter regime for planetary cores, a dynamo model would need to resolve the Ekman and Stewartson boundary layers in the core which are very thin. For example, with rigid boundary conditions, the Ekman layer thickness at the core-mantle boundary is  $\delta \propto E^{1/2} r_o$ . This results in an Ekman boundary layer thickness of  $\sim 3 \times 10^{-8} r_o$  which is about 0.1 m in the Earth's core. If instead, one argues that turbulent eddies in the core are responsible for diffusion, then the Ekman number is about  $10^{-9}$  which leads to an Ekman layer thickness of about 100 m which is better, but still not numerically feasible.

The turbulence in the problem also results in very large Reynolds number (ratio of viscous diffusion time to convective time) in the core:

$$Re = \frac{UL}{\nu} \approx 10^8, \quad (1.34)$$

where  $U$  and  $L$  are characteristic velocity and length scales of the convection. In order to achieve these Reynolds numbers, the models need to employ highly supercritical Rayleigh numbers. This leads to very small scale structure which, similar to the Ekman number issue, requires much higher spatial resolution than is currently possible.

Because of these issues, one might be shocked that numerical models do as well as they do at reproducing the Earth's field. Since the field we observe is just the extension of the poloidal field filtered to low degree and order, one might ask whether it is just a coincidence that we can reproduce the large scale structure of the field. If this is the case, then the dynamics seen inside the cores of dynamo models may not be representative of what is happening inside planetary cores. Another possibility (the excessively optimistic one) is that the large scale structure may not really be affected by the small scale workings inside the core, and all we need to understand the generation of the large scale field is the low degree components in the magnetic and velocity fields. Most likely, the truth is somewhere between these two extremes. Some aspects of the dynamo may only require the large scale components, whereas others may rely on the small. More observational data from planets, and better numerical models will be necessary to answer these questions.

It is important to understand what should be taken out of numerical modeling exercises. In the parameter regimes numerical models work in, if a particular result is found, one needs to ask whether it is reasonable that in the planetary regime, this result will occur. For example if a certain aspect of a model seems to be due to the large viscous forces present, then it is most likely that it will not be present in a planetary core where the viscous forces are small. Similarly, if an aspect is only present at slightly-supercritical Rayleigh numbers, then it is unlikely that it is present in the highly supercritical Rayleigh number regime of planetary cores. With this in mind, we step with caution into the realm of numerical modeling in the following chapters, in an effort to understand the effects of geometry on magnetic field morphology.

**Table 1.3:** Summary of current numerical dynamo models.  $Pr = v/\kappa$ . In the boundary conditions column, I.C. refers to inner core, and rigid or stress-free refer to the boundary conditions on the velocity. Some models have changed approximations or parameters with time and different studies, so the values listed are only meant as a guide. The numbers in the ref.'s column refer to the following: (1)-(6): Glatzmaier and Roberts (1995a,b, 1996a,b, 1997, 1998), (7): Glatzmaier *et al.* (1999), (8): Glatzmaier and Clune (2000), (9): Glatzmaier (2002), (10): McMillan *et al.* (2001), (11)-(12): Roberts and Glatzmaier (2000a,b), (13): Buffett and Glatzmaier (2000), (14): Coe *et al.* (2000), (15)-(17): Kuang and Bloxham (1997, 1998, 1999), (18): Kuang (1999), (19): Bloxham (2000a), (20): Buffett and Bloxham (2002), (21): Dumberry and Bloxham (2003), (22): Stanley and Bloxham (2004), (23)-(25): Kageyama and Sato (1997a,c,b), (26): Kageyama *et al.* (1999), (27): Ochi *et al.* (1999), (28): Li *et al.* (2002), (29): Kida *et al.* (1997), (30)-(31): Kida and Kitauchi (1998a,b), (32): Kitauchi and Kida (1998), (33): Kitauchi (1998), (34)-(36): Ishihara and Kida (2000, 2002a,b), (37): Busse *et al.* (1998), (38): Grote *et al.* (1999), (39)-(40): Grote *et al.* (2000a,b), (41): Grote and Busse (2000), (42): Busse (2000), (43): Grote and Busse (2001), (44): Busse (2002), (45-46): Christensen *et al.* (1998, 1999), (47): Olson *et al.* (1999), (48): Wicht (2002), (49): Olson and Christensen (2002), (50): Kutzner and Christensen (2002), (51): Christensen and Olson (2003), (52): Christensen and Tilgner (2004), (53): Aubert and Wicht (2004), (54): Wicht and Olson (2004), (55): Sakuraba and Kono (1999), (56)-(57): Kono *et al.* (2000); Kono and Roberts (2002), (58): Katayama *et al.* (1999), (59)-(60): Takahashi *et al.* (2001, 2003). Aside from the references column, this table is adapted from Dormy *et al.* (2000).

Model	$E_m$	$Pr$	$q_\kappa$	approximations	Boundary conditions	Refs.
Glatzmaier and Roberts	$1.8 \times 10^{-6}$	725	725	anelastic, axial-inertia, hyperdiffusion	insulating mantle, conducting I.C., rigid,	(1)-(14)
Kuang and Bloxham	$2 \times 10^{-6}$	1	1	Boussinesq, axial-inertia, hyperdiffusion	insulation mantle + conducting layer, conducting I.C., stress-free	(15)-(22)
Kageyama and Sato	$4 \times 10^{-4}$	1	10.6-15	compressible, full-inertia, perfect gas	$\mathbf{B} \times \mathbf{r} = 0$ , rigid	(23)-(28)
Kida and Kitauchi	$5.6 \times 10^{-3}$	1	8.3-14.2	Boussinesq, full-inertia	vacuum, rigid	(29)-(36)
Busse Grote Tilgner	$5.1 \times 10^{-4}$	5	100	Boussinesq, full-inertia	insulating mantle and I.C., stress-free	(37)-(44)
Christensen Olson Glatzmaier	$4.2 \times 10^{-5}$	1	0.5-5	Boussinesq, full-inertia	Insulating mantle and I.C., rigid/stress free	(45)-(54)
Sakuraba and Kono	$6.3 \times 10^{-5}$	1	20	Boussinesq, full-inertia, hyperdiffusion	conducting I.C., Insulating mantle, rigid	(55)-(57)
Katayama Matsushima Honkura	$7.2 \times 10^{-3}$	1	35	Boussinesq, full-inertia	Insulating mantle and I.C., stress-free	(58)-(60)

# Chapter 2

## Uranus and Neptune

### 2.1 Introduction

The two ice giants, Uranus and Neptune, have only been visited by one spacecraft, Voyager II, which was launched on August 20, 1977 and visited all four giant planets (Jupiter, Saturn, Uranus and Neptune) between 1979 and 1989. The spacecraft took advantage of a rare alignment of the four planets which only occurs once every 175 years. This alignment provided a simple trajectory to encounter all four planets and allowed the use of gravity assists from each planet to get to the next. Amazingly, Voyager II along with its twin, Voyager I, are still in operation today and returning valuable science (the phrase '*they don't make them like they used to*' comes to mind). Both spacecraft are heading out of the solar system in search of the heliopause. This boundary is analogous to the magnetopause which surrounds planets with intrinsic magnetic fields and separates the regions where the internal magnetic field and solar magnetic field dominate. Recently, there has been some evidence that Voyager I has crossed the termination shock (Krimigis *et al.*, 2003), although it remains controversial (McDonald *et al.*, 2003).

The planets are called 'ice' giants because their main constituents, namely water ( $H_2O$ ), ammonia ( $NH_3$ ) and methane ( $CH_4$ ), are in their solid states at the temperatures characteristic of the region of the solar nebula where they are located. This does not mean the planets themselves are solid, since at the temperatures and pressures in their interiors, these components are definitely fluid. These constituents do not remain intact molecules at the pressures in their interiors, and most likely dissociate into various ions. In addition to their main ice-rich components, the planets also possess relatively small hydrogen-helium atmospheres and possibly contain small rocky cores.

Not much is known about the interior composition and structure of the two planets. Experimental studies of ice-giant-like compositions have been carried out to determine the properties of the materials at characteristic temperatures and pressures in their interiors (Nellis *et al.*, 1988; Hubbard *et al.*, 1991; Benedetti *et al.*, 1999), and numerical experiments have determined possible internal structures for the planets using the observed mass, radius, moment of inertia and gravitational harmonic coefficients for the planets (Hubbard *et al.*, 1991; Marley *et al.*, 1995; Podolak *et al.*, 1995, 2000). A schematic of their interior structure is shown in Figure 2.1 with characteristic temperatures and pressures indicated. Although the schematic has the regions completely separated, this is most likely not the case for the planets (Podolak *et al.*, 1995). In reality, the hydrogen-helium gas atmosphere also contains a larger than solar proportion of heavy elements such as the 'ice'  $CH_4$ , and the 'Ice' and 'Rock' layers may be mixed to some degree. Notice there is no labeling of the specific

**Table 2.1:** Physical properties of Uranus and Neptune. Data taken from Holme (1995) and references therein.

Property	Uranus	Neptune
Planet radius (km)	25600	24800
Planet mass (Earth masses)	14.53	17.14
Mean density ( $\text{kg/m}^3$ )	1285	1640
Surface gravity ( $\text{m/s}^2$ )	8.8	11.1
Dimensionless moment of inertia	0.23	0.24
$J_2$	$3.34 \times 10^{-2}$	$3.41 \times 10^{-2}$
$J_4$	$-2.8 \times 10^{-5}$	$-2.6 \times 10^{-5}$
Rotation period (hours)	17.24	16.11
Orbital period (Earth years)	84	164.8
Solar distance (AU)	19.2	30.0
Obliquity of spin axis (degrees)	98	29

radii at which these transitions occur in Figure 2.1 since this is relatively model dependent, but the sizes shown are approximately correct. Table 2.1, which lists some of the physical properties of the two planets, demonstrates their similarity. The only major difference is in their spin axis obliquities, with Uranus effectively rotating on its side. This is most likely due to a collision with a large body in Uranus' past, as opposed to some natural difference between Uranus' and Neptune's interiors.

## 2.2 Uranus' and Neptune's Magnetic Fields

### 2.2.1 Observations and Models

Voyager II carried out magnetic field measurements as it flew by Uranus and Neptune. The spacecraft was in the magnetospheres of Uranus and Neptune for approximately 16 and 38 hours respectively (Connerney *et al.*, 1987, 1991) and followed the trajectories shown in Figure 2.2. With the limited data from the flyby's, Connerney *et al.* (1987, 1991) created magnetic field models (see section 1.2) that were truncated at relatively low spherical harmonic degree and order. They used the limited data to construct partial solutions to the linear inverse problem by reparameterizing the problem in terms of eigenvectors that are linear combinations of the original Gauss coefficients. For more details on the method employed, see Connerney (1981). Using this method, they produced a magnetic field model that resolved the first eight Gauss coefficients (i.e. the dipole and quadrupole terms) for Uranus, called the ' $Q_3$ ' model. For Neptune, the dipole terms were well resolved, and some quadrupole and octupole terms were well or marginally resolved, leading to the ' $O_8$ ' model. Table 2.2 lists the Gauss coefficients for Uranus and Neptune from these two models.

More recently, Holme and Bloxham (1996) used a different approach which allowed them to examine higher degree structure in the fields. They truncated the spherical harmonic expansion to degree and order 16 and then resolved the non-uniqueness of field models by imposing smoothing constraints on the fields. For example, they solved for fields with minimum mean field strength averaged over a spherical surface, or fields which produced minimum ohmic heating. Although the smoothing constraints may not be realistic, it was found that the models created were quite robust

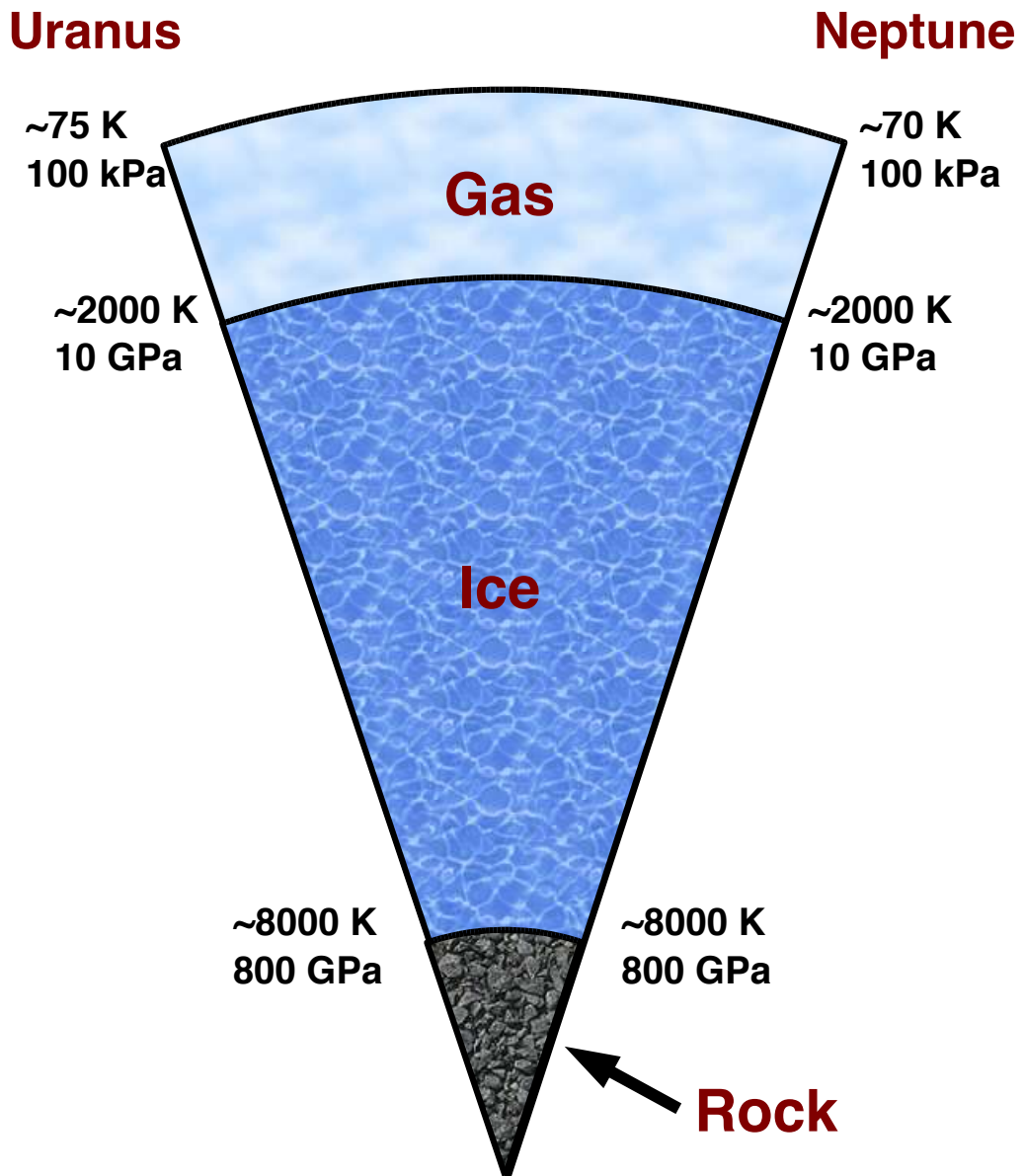


**Figure 2.1:** Interior structure of Uranus and Neptune. The region labeled 'Gas' consists mostly of molecular  $H_2$ , helium and some ices, the region labeled 'Ice' consists mainly of  $H_2O$ ,  $CH_4$ ,  $NH_3$ , but most likely has some hydrogen and rocky elements mixed in, and the region labeled 'Rock', which consists of magnesium-silicate and iron material, may or may not exist. The Figure is adapted from Guillot (1999).

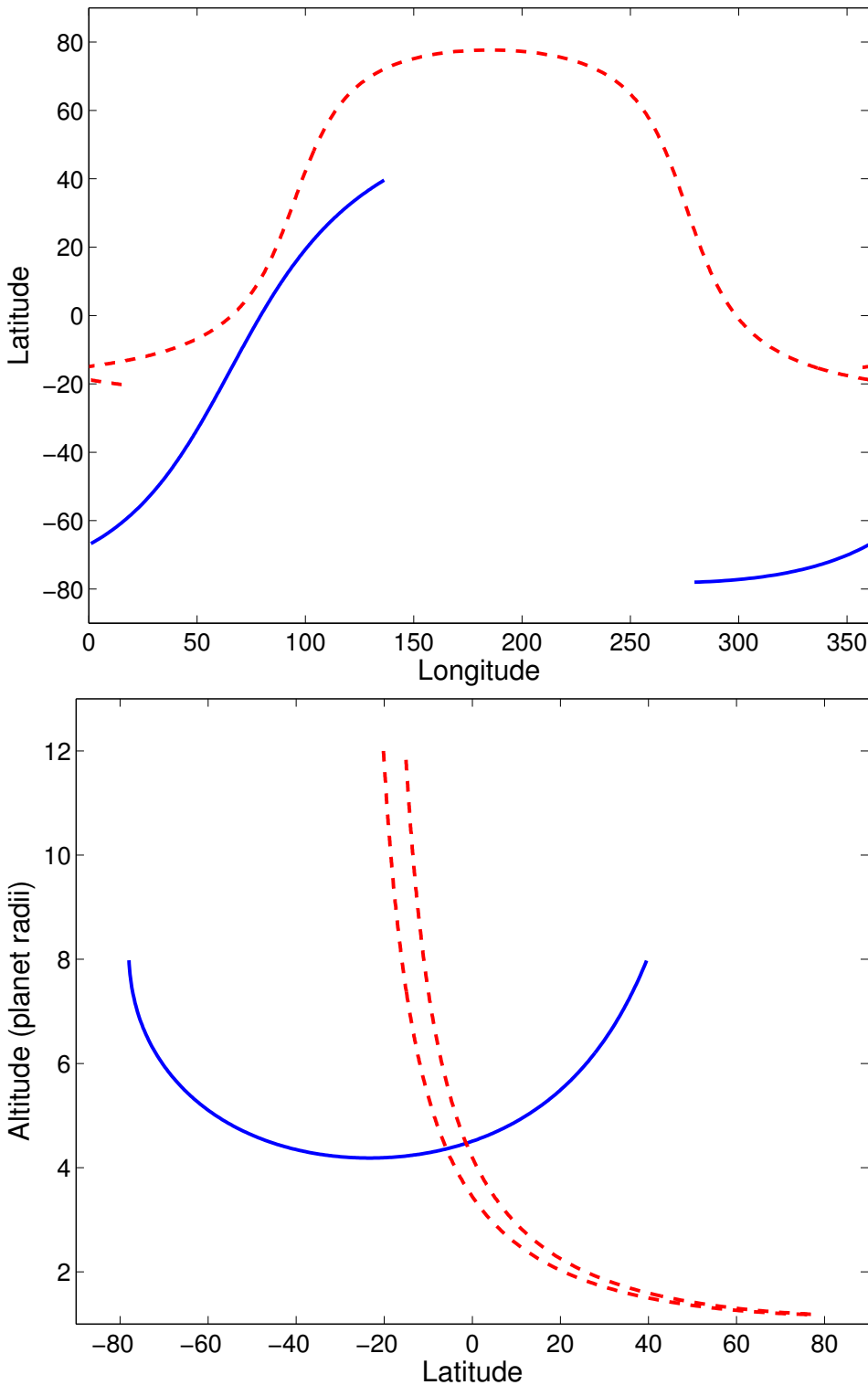


**Figure 2.2:** Voyager II trajectory shown as latitude vs. longitude coverage (top) and altitude vs. latitude coverage (bottom). The blue solid lines are the trajectory for the Uranus flyby and the red dashed lines are the trajectory for the Neptune flyby.

**Table 2.2:**  $Q_3$  and  $O_8$  magnetic field models for Uranus and Neptune respectively. Gauss coefficients are in nanoTeslas. Entries marked with '\*' indicate coefficients that are marginally resolved, '(nr)' indicates coefficients that are not resolved, and all other entries are well resolved. Data from Connerney *et al.* (1987, 1991).

Gauss coefficient	Uranus $Q_3$	Neptune $O_8$
$g_1^0$	11893	9732
$g_1^1$	11579	3220
$h_1^1$	-15684	-9889
$g_2^0$	-6030	7448
$g_2^1$	-12587	664*
$g_2^2$	196	4499
$h_2^1$	6116	11230(nr)
$h_2^2$	4759	-70
$g_3^0$	2705(nr)	-6592(nr)
$g_3^1$	1188(nr)	4098(nr)
$g_3^2$	-4808(nr)	-3581(nr)
$g_3^3$	-2412(nr)	484*
$h_3^1$	-7095(nr)	-3669*
$h_3^2$	-1616(nr)	1791(nr)
$h_3^3$	-2608(nr)	770*

to the choice of constraint, indicating that the major features in the models were required by the data and not artifacts of a particular smoothing constraint chosen. In this way, they were able to create field models for the planets with higher degree structure than was previously done. Table 2.3 lists the Gauss coefficients out to degree and order 3 for Uranus and Neptune from the Holme and Bloxham models.

In equation 1.1 the magnetic potential was given for a field whose only source is internal to the planet. Although this is a good approximation for the outer planets, it is not entirely correct since the interplanetary magnetic field originating from the Sun is present as well. In this case, we must also account for this external source in the spherical harmonic expansion of the magnetic potential and the total potential is given by

$$\Phi = a \sum_{l=1}^{\infty} \sum_{m=0}^l \left\{ \left( \frac{a}{r} \right)^{l+1} [g_l^m \cos(m\phi) + h_l^m \sin(m\phi)] + \left( \frac{r}{a} \right)^l [G_l^m \cos(m\phi) + H_l^m \sin(m\phi)] \right\} P_l^m(\cos \theta), \quad (2.1)$$

where  $G_l^m$  and  $H_l^m$  are the Gauss coefficients of the external magnetic field. In order to create the internal field models, the external field must be removed from the magnetic field data. This is relatively simple to do at Uranus and Neptune since they are so far from the Sun. The external field is relatively weak and can be well approximated by spherical harmonic degree  $l=1$  terms only. The

**Table 2.3:** Holme and Bloxham magnetic field models for Uranus and Neptune using the ohmic heating smoothing constraint. Gauss coefficients are in nanoTeslas. The models are truncated at degree 16, however we only show the first 3 degrees in order to compare with the models in Table 2.2. For information on the higher degree coefficients and the resolution of all the coefficients, see Holme (1995); Holme and Bloxham (1996).

Gauss coefficient	Uranus	Neptune
$g_1^0$	11855	10336
$g_1^1$	11507	3359
$h_1^1$	-15812	-9772
$g_2^0$	-5877	8566
$g_2^1$	-13085	-406
$g_2^2$	-605	4644
$h_2^1$	5851	11139
$h_2^2$	4185	-743
$g_3^0$	4183	-5749
$g_3^1$	-1336	11632
$g_3^2$	-6776	-1889
$g_3^3$	-4021	-2920
$h_3^1$	-5817	-3905
$h_3^2$	-357	903
$h_3^3$	-2265	-245

values used by Holme and Bloxham (1996) are (in nanoTeslas):

$$\begin{aligned} \text{Uranus : } & G_1^0 = -1.64, \quad G_1^1 = -0.99, \quad H_1^1 = -0.19 \\ & \text{Neptune : } G_1^0 = -0.25, \quad G_1^1 = 0.17, \quad H_1^1 = 0.23. \end{aligned} \tag{2.2}$$

## 2.2.2 A New Field Morphology

Having a quick look through Uranus' and Neptune's internal Gauss coefficients we see that some of the quadrupole and octupole coefficients are as large as the dipole coefficients, and the non-axisymmetric coefficients ( $m \neq 0$ ) are similar in size to the axisymmetric coefficients ( $m = 0$ ). This is quite unlike Earth's, Jupiter's and Saturn's magnetic fields where the axisymmetric dipole is dominant. The difference between the fields is easily demonstrated by examining their magnetic power spectra. The power in each harmonic degree and order of the field at a particular distance from the planet ( $r$ ) can be defined in terms of the mean square field intensity:

$$p(l, m, r) = (l+1) \left( \frac{a}{r} \right)^{(2l+4)} [(g_l^m)^2 + (h_l^m)^2]. \tag{2.3}$$

In Figure 2.3 we plot the magnetic power spectra at the surface of the planets ( $r = a$ ) for Earth,

Jupiter, Saturn, Uranus and Neptune. Power vs. degree  $l$  is found by summing over the order  $m$  components of equation 2.3 for each degree  $l$ , and power vs order  $m$  is found by summing over the degree  $l$  components for each order  $m$ . The axisymmetry of Earth's, Jupiter's and Saturn's fields is demonstrated by the dominance of the  $m = 0$  power, and the dipole-nature of their fields is evident in the dominance of the  $l = 1$  power. This is not the case for Uranus and Neptune whose fields are not dipole-dominated (comparable power at degrees 1,2 and 3) and contain significant power in both axisymmetric ( $m = 0$ ) and non-axisymmetric (higher order  $m$ ) components.

### 2.2.3 Dynamo Location

In order to find the dynamo source region in a planet, we must determine where the electrically conducting, fluid region undergoing convective motions is located. For Earth, we know the magnetic field is generated in the fluid iron outer core; this is the only liquid region in the planet with high enough electrical conductivity to generate the scale of magnetic field seen. At first glance it may appear difficult to determine where the magnetic field is being generated in the giant planets since we have much less information on their interior structures, however a quick look at the various possibilities leads us to the most likely answers.

#### Jupiter and Saturn

Jupiter's and Saturn's interior structures are shown in Figures 2.4 and 2.5 respectively. The planets consist mostly of hydrogen and helium which is found in the molecular phase at lower pressures and transforms to a metallic phase due to pressure ionization at higher pressures. Determining where this transition from molecular to metallic hydrogen occurs is difficult since it requires working with hydrogen at high pressures and temperatures and is therefore not well understood either experimentally or theoretically. See Hubbard *et al.* (2002) for a review of current knowledge of the hydrogen phase diagram.

For our purposes of locating the dynamos in Jupiter and Saturn, we are interested in the electrical conductivity of hydrogen in these planets. Nellis *et al.* (1996); Nellis (2000) use shock compression experiments in liquid hydrogen in order to examine the electrical conductivity of the fluid as a function of pressure and temperature. They find that for Jupiter, the minimum conductivity of a disordered fluid metal ( $\sigma = 2 \times 10^5 (\Omega m)^{-1}$ ) is reached at a radius of 0.90 Jupiter radii. Since Saturn is smaller, this transition occurs deeper in the planet at about 0.5 Saturn radii.

Voyager I and II obtained values for the heat fluxes from Jupiter and Saturn which determined that the planetary interiors are convective (Hanel *et al.*, 1981, 1983). We therefore have an obvious electrically conducting, convecting fluid region where the dynamo can operate. The other possibility, that the dynamos are located in the liquid iron cores of the 'Rock and Ice' layers (which may not exist) can be discarded on the basis of the intensity and complexity of the observed fields. If the fields were generated there, then we would expect to see a much smaller and very dipolar dominated field at spacecraft altitude since we are much further from the source region. Also, the field would still interact with the electrically conducting metallic hydrogen layer surrounding it.

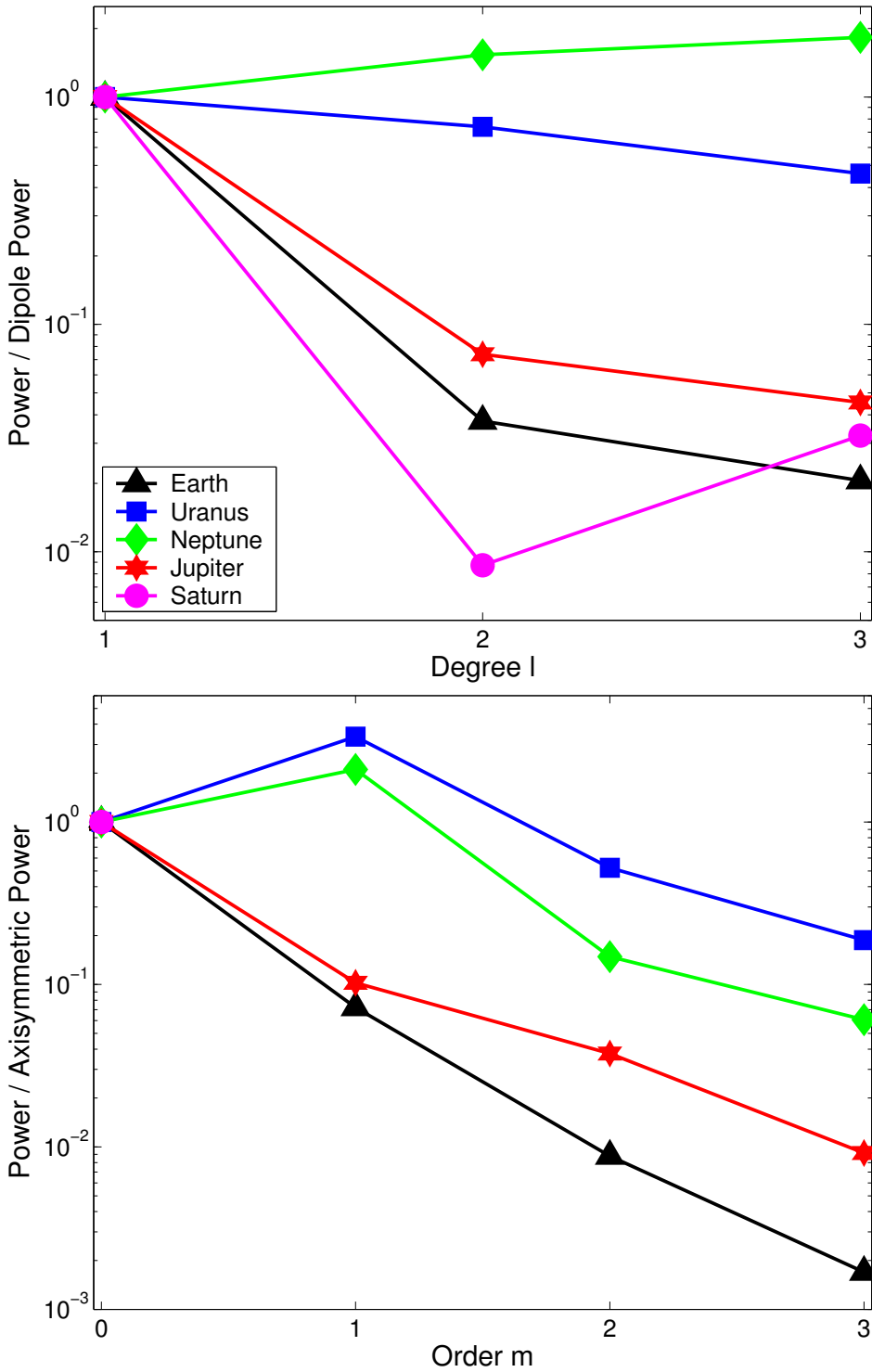


**Figure 2.3:** Surface magnetic power spectra for Earth, Jupiter, Saturn, Uranus and Neptune. Power vs. degree normalized to the dipole ( $l=1$ ) power is shown in the top plot and power vs. order normalized to the axisymmetric ( $m=0$ ) power is shown in the bottom plot. In the power vs. order plot, Saturn's spectrum is only represented by the  $m = 0$  magenta circle because observations indicate all higher  $m$  terms are zero. The legend in the top plot also applies to the bottom plot.

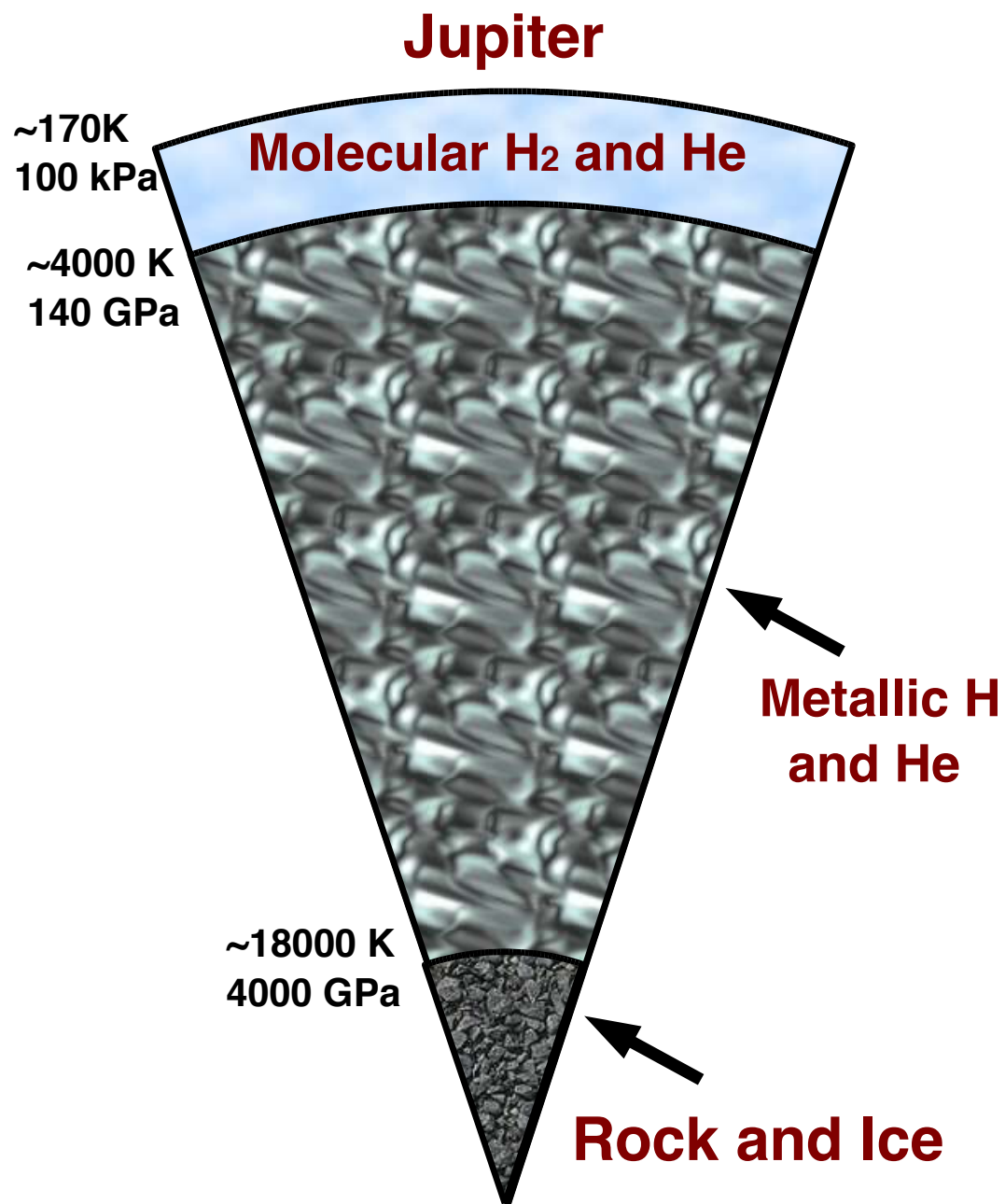


**Figure 2.4:** Jupiter's interior structure adapted from Guillot (1999).

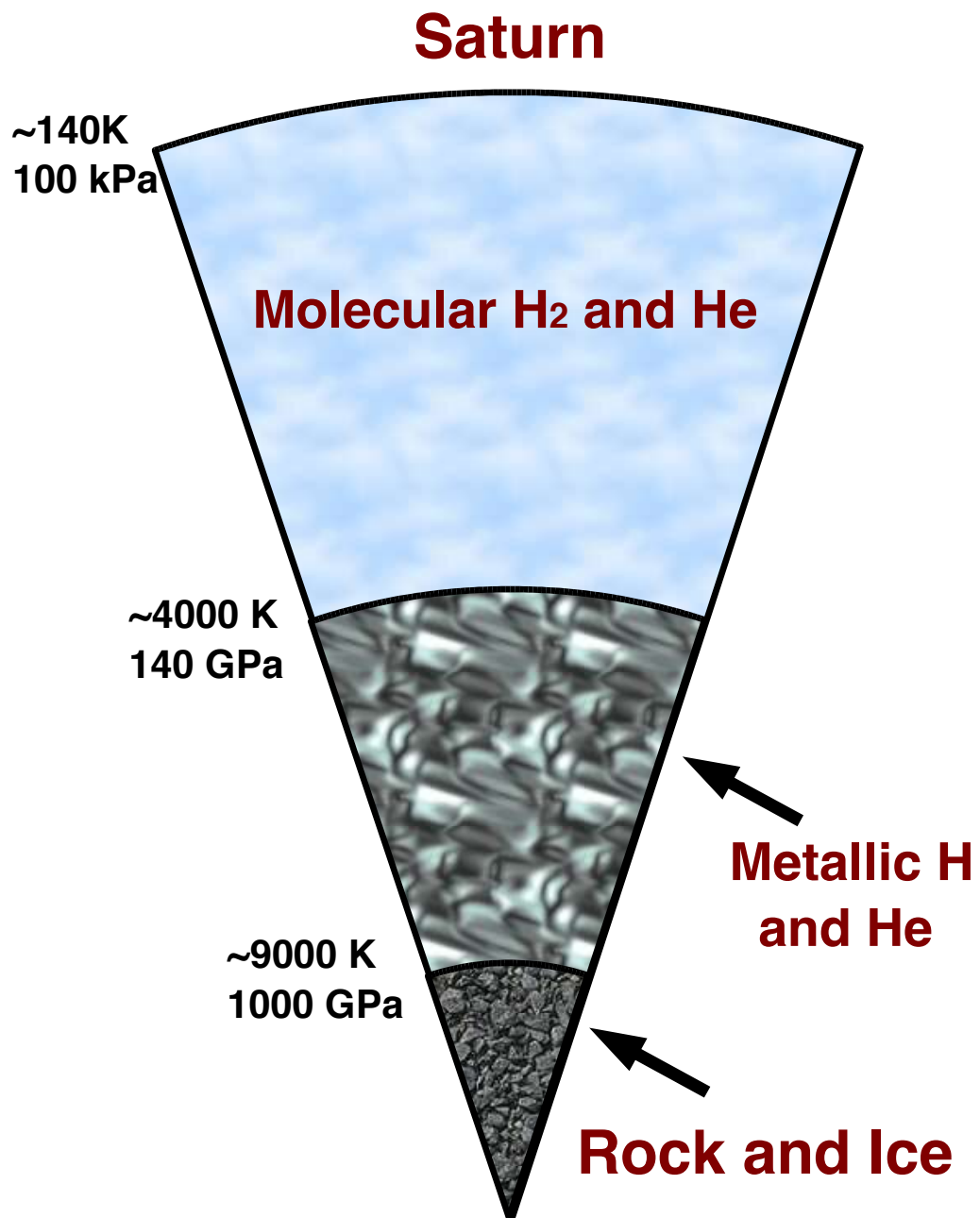


**Figure 2.5:** Saturn's interior structure adapted from Guillot (1999).

## Uranus and Neptune

The hydrogen atmospheres in Uranus and Neptune are much smaller than in Jupiter and Saturn, and do not reach the pressures and temperatures necessary to transform to metallic state. We must therefore look to other locations for the dynamos in these planets. The small (possibly non-existent) rocky core is another possibility, but similar to our argument for Jupiter and Saturn, it is unlikely that the observed fields are generated there because of their complexity and intensity. In fact this is a much stronger argument for Uranus and Neptune than it was for Jupiter and Saturn because of the much larger quadrupole and octupole field components of Uranus' and Neptune's fields. If the source region is buried deep in the planet, it is unlikely that we would see such a large non-dipolar field since power in higher degree components is attenuated more strongly with distance from the source.

This leaves the fluid 'ice' layer as the best possibility. The pressure is not high enough for the ices to attain a metallic state in these planets, however shock wave experiments which measure electrical conductivity for various planetary ices and mixtures of the ices at Uranus- and Neptune-like temperatures and pressures show that the materials attain an ionic conductivity of about  $2 \times 10^3 (\Omega m)^{-1}$  above 40 GPa (David and Hamann, 1959; Hamann and Linton, 1969; Mitchell *et al.*, 1980; Mitchell and Nellis, 1982; Nellis *et al.*, 1988). For Uranus, this corresponds to a radius of about 0.7 Uranus radii, and for Neptune, about 0.8 Neptune radii. It is most likely then, that Uranus' and Neptune's dynamos operate in the ionically conducting liquid ice layers of the planets which extend out to about 3/4 of their planetary radii.

## 2.3 Explanations for the Anomalous Fields

Since Uranus and Neptune have a very similar internal structure and composition, and they both possess a similar magnetic field morphology, it seems a likely bet that their dynamo mechanisms are similar as well. Different explanations for these planets' anomalous fields have been proposed in the past. Schulz and Paulikas (1990) tried to explain Uranus' magnetic field in terms of a reversal. If Uranus has similar reversal timescales as Earth, then the chance of observing the field in reversal is about 1 percent (small but not impossible). However, when Neptune's field was also observed to be anomalous, this argument seemed much less appealing since the probability of observing two planets in the process of reversing becomes very small. This argument becomes more attractive if reason is found for the fields to reverse much more frequently than Earth's field and we will discuss this in later sections.

Other explanations included appealing to Uranus' large obliquity (Podolak *et al.*, 1991), however an alternative mechanism would then be needed to explain Neptune's field. Connerney *et al.* (1987, 1991) suggest that the non-axisymmetric fields are due to fewer and larger convection cells in Uranus and Neptune, however their argument does not explain the non-dipole nature of the field.

Holme (1995); Holme and Bloxham (1996) suggest the fields' anomalous natures are due to the fact that the fields are not in magnetostrophic balance, unlike the other giant planets and Earth, and it is therefore not surprising that the fields are different. Their argument is based on comparing these planets' surface heat flows to the ohmic heating that would result from a dynamo in magnetostrophic balance. The ohmic heating produced from these estimates is greater than the surface heat flow and so they conclude that the fields cannot be in magnetostrophic balance. However, there are some reservations on the scaling approach used (Stevenson, 1983, 2003a) since these estimates are based

on ideas from dipole dominated Earth-like fields. There is also no particular evidence that a weak-field dynamo (*i.e.* non-magnetostrophic force balance) would lead to non-dipolar, non-axisymmetric fields.

There have also been some proposed explanations that rely on geometry to explain the anomalous fields. Holme (1995); Holme and Bloxham (1996) suggest that the fields are produced by chaotically, rapidly reversing dynamos resulting from the lack of a relatively large solid conducting inner core in the planets to stabilize the fields. However, Jupiter and Saturn do not contain large conducting inner cores and still maintain axisymmetric, dipolar dominated fields. Numerical models have also shown that the opposite is more likely: dynamos with smaller electrically conducting inner cores have more axially-dipolar dominated fields (Roberts and Glatzmaier, 2001).

In the other extreme, a thin shell dynamo geometry has been used to explain the fields. Ruzmaikin and Starchenko (1991) suggest that the dynamo operates in a thin layer of metallized carbon at the base of the ice shell, and that the thinness of the shell would result in more complex, small scale fields. However, there is no evidence for this metallized carbon layer and the magnetic field would still interact strongly with the conducting ice layer above. In a later section we will show that the geometry they propose would not produce the fields observed at Uranus and Neptune. Hubbard *et al.* (1995) also suggest a thin shell dynamo as an explanation, however in their scenario, the thin shell is located in the outermost part of the electrically conducting fluid ice layer. In the next section we present their argument as to why the dynamo may be located here.

### 2.3.1 Stable Stratification in Uranus and Neptune

It is easier to measure the intrinsic heat flows of the giant planets via remote sensing than it is for the terrestrial planets because they are further out in the solar system (smaller thermalization by sunlight) and because the heat flow values are larger in absolute terms. Table 2.4 lists the heat flow parameters for the giant planets. These parameters can be used to tell us about the thermal regime and interior dynamics of the planet. Notice that although Uranus and Neptune are very similar planets, they have quite different energy balances. The heat flow from Neptune requires that there be a significant internal source (the non-dimensional energy balance is larger than 1) whereas for Uranus, the internal heat flow appears to be quite small. We can use this heat flow information to determine how much of the planet is convecting.

If the dominant source of internal luminosity  $L$  of a planet is loss of internal heat content, then the appropriate equation defining thermal evolution is given by:

$$4\pi R_P^2 \sigma_B (T_e^4 - T_0^4) = -\frac{dE_{th}}{dt}, \quad (2.4)$$

where  $R_P$  is the planet radius,  $\sigma_B$  is the Stefan-Boltzmann constant,  $T_e$  is the effective temperature,  $T_0$  is the effective temperature if there were no internal heat source (*i.e.* the value due to solar insolation only), and  $E_{th}$  is the internal thermal energy. The thermal energy can be given in the form:

$$E_{th} = MC_v \langle T_i \rangle, \quad (2.5)$$

where  $M$  is the planetary mass,  $C_v$  is the specific heat at constant volume per unit mass and  $\langle T_i \rangle$  is the average internal temperature. In order to solve the differential equation 2.4, we need a relationship between the effective temperature and the internal temperature. If one assumes that the mean internal temperature is proportional to the effective temperature, with a constant of proportionality

**Table 2.4:** Heat flow parameters for the giant planets. The effective temperature is defined as the temperature a blackbody would have if it had the planet's total infrared energy flux. The energy balance is the ratio of the average total infrared energy flux from the planet (interior plus thermalized sunlight) to the value of thermalized sunlight alone. Table adapted from Podolak *et al.* (1991).

Parameter	Jupiter	Saturn	Uranus	Neptune
Effective temperature (K)	$124.4 \pm 0.3$	$95.0 \pm 0.4$	$59.1 \pm 0.3$	$59.3 \pm 0.8$
Energy balance (non-dimensional)	$1.67 \pm 0.09$	$1.78 \pm 0.09$	$1.06 \pm 0.08$	$2.61 \pm 0.28$
Internal energy flux ( $\text{W m}^{-2}$ )	$5.44 \pm 0.43$	$2.01 \pm 0.14$	$0.042 \pm 0.047$	$0.433 \pm 0.046$
Internal power/unit mass ( $10^{-11}\text{W kg}^{-1}$ )	$17.6 \pm 1.4$	$15.2 \pm 1.1$	$0.392 \pm 0.441$	$3.22 \pm 0.34$

that does not change during the evolution (Hubbard *et al.*, 1995), then equation 2.4 can be rewritten in the form:

$$Af \frac{dT_e}{dt} = -(T_e^4 - T_0^4), \quad (2.6)$$

where  $A$  is a constant that characterizes the thermal inertia of the interior and  $f$  is the fraction of that thermal content that is available for driving the luminosity ( $0 \leq f \leq 1$ ). Solving this equation shows that the present day observed luminosity of the planets (the internal power/ unit mass is also known as the specific luminosity  $L/M$ ), is only consistent with  $f$  values of about 0.4 for Uranus and 0.6 for Neptune (see Hubbard *et al.* (1995) for details). This means that the ice layers cannot be fully convective since then, the entire layer would be available for driving the luminosity ( $f \approx 1$ ). Instead, it seems that only the outer 0.4 and 0.5 planetary radii for Uranus and Neptune respectively, are contributing to the luminosity. Notice that a very small difference in this radius can account for the very different heat flows observed from the planets.

If the planets are not fully convective, some factor must be keeping the interior regions from convecting. If thermal effects are the only source of buoyancy, then the Schwarzschild's instability condition says that convection occurs if the temperature gradient is greater in magnitude than the adiabatic gradient:

$$\frac{dT}{dr} \leq \left( \frac{dT}{dr} \right)_{ad} = \frac{-g\alpha_T T}{C_P}, \quad (2.7)$$

where  $T$  is temperature,  $r$  is radius,  $g$  is the gravitational acceleration, and  $C_P$  is the specific heat at constant pressure per unit mass. (Note: there is a ' $<$ ' operator in the equation because the temperature gradient is negative. In order for it to be larger in magnitude than the adiabatic gradient, the actual gradient must be less than the adiabatic gradient).

The possibility that the interior region is sub-adiabatic (hence not convecting) because it was not heated as much as the outer regions during accretion is rejected by Podolak *et al.* (1991) using simple scaling analysis. The other possibility is that the interior region is not convecting because of a compositional stratification. In the presence of compositional differences, the Schwarzschild's

instability condition is given by

$$\frac{dT}{dr} < \left( \frac{dT}{dr} \right)_{ad} - \frac{\alpha_\xi}{\alpha_T} \frac{d\xi}{dr}, \quad (2.8)$$

where  $\xi$  is the concentration of light element in a fluid and  $\alpha_\xi = -\rho^{-1}(\partial\rho/\partial\xi)$  is the compositional equivalent of the thermal expansion coefficient  $\alpha_T$  (Gubbins and Roberts, 1987). It is therefore possible to have a region that is not convecting (stable) even if the temperature gradient is super-adiabatic. It should be stressed that a continuously changing compositional profile, or an extremely large number of small homogeneous layers is necessary to suppress the heat flow. Having a few compositionally separate layers that are homogeneous within themselves will not do the trick since the planet is then nearly adiabatic throughout most of its interior. A continuously stable stratification is possible and is seen in other fluids such as the Earth's oceans where salinity gradients provide stability.

Although compositional stratification could explain the low heat flows from Uranus and Neptune, we should look into whether they are a reasonable choice for the interior composition of these planets. The terrestrial planets are separated into only a few compositionally distinct layers that are homogeneous within themselves because at the temperatures and pressures present, metallic iron and mantle material are mutually insoluble and they separate out. This is not expected in Uranus and Neptune since the main constituents are miscible at the relevant temperatures and pressures. Another way to achieve only a few homogeneous layers is with heterogeneous accretion, but current quantitative models (Lissauer *et al.*, 1995) suggest this is unlikely for Uranus and Neptune since part of the accreting material is from large bodies that only partially mix with the previous accreted material. Without reason as to why Uranus and Neptune would form a small number of homogeneous layers, and since we know the planets are not made up of only a single component, it appears that a stably-stratified interior region is possible, although currently, there is no direct evidence.

We do however, have some indirect evidence. As we've already discussed, this possibility can explain the anomalously low heat flows from Uranus and Neptune which may be considered indirect evidence for the stable layer existence. The shock pressure experiments of Benedetti *et al.* (1999) may provide more indirect proof as they show that for conditions in Uranus and Neptune, dissociation of 'ice' molecules into different chemical components occurs, and any heavier dissociated components should sink deeper into the planets. This may result in the compositional stratification needed to explain the low luminosities. Further indirect evidence may come from the planet's magnetic fields. Hubbard *et al.* (1995) suggest that this interior structure may help to explain the anomalous magnetic fields of Uranus and Neptune since the stable stratification would place the convective region in a thin shell that is close to the planet surface. They invoke the same reasoning as Ruzmaikin and Starchenko (1991) as to why a thinner shell may promote non-dipolar structure.

This is the hypothesis we will examine in the remainder of this chapter. A thin convecting shell surrounding a stably-stratified fluid core is a different geometry from the Earth-like thick convecting shell surrounding a small solid conducting inner core, and we wish to examine its effect on the morphology of the produced fields. We will approach this geometry in two steps. First we will examine the effect of a thin shell dynamo with a large solid inner core on the magnetic field morphology produced. We will then replace the solid inner core with a stably-stratified fluid core to determine if this affects the morphology.

**Table 2.5:** Solid inner core model parameters.

---

Model #	$r_{io}$	$\eta_{io}$	$Ra$
1	0.35	1	18000
2	0.7	1	18000
3	0.7	100	18000
4	0.7	10000	24000
5	0.8	1	30000
6	0.8	1	40000
7	0.9	1	60000
8	0.9	1	70000

---

## 2.4 Dynamos With Solid Inner Cores

### 2.4.1 Model Setup

The equations and parameters solved by the Kuang and Bloxham numerical dynamo model were given in section 1.4. The parameter governing the size of the inner core in the model is

$$r_{io} \equiv \frac{r_i}{r_o} \quad (2.9)$$

where  $r_i$  is the solid inner core radius and  $r_o$  is the total radius of the core. The important role of the inner core in magnetic field generation was discussed in section 1.3.4. Aside from its size, its conductivity was also shown to be important. The inner core's conductivity is parameterized in the models as the ratio of the inner and outer core magnetic diffusivities:

$$\eta_{io} = \frac{\eta_i}{\eta_o} \quad (2.10)$$

where  $\eta_i$  and  $\eta_o$  are the magnetic diffusivities of the solid inner core and fluid outer core respectively. If one were modeling the Earth's dynamo, these parameters would take the values  $r_{io} \approx 0.35$  and  $\eta_{io} \approx 1$ . We created numerical models with various values for  $r_{io}$ ,  $\eta_{io}$  and  $Ra$  (defined in equation 1.32). Table 2.5 lists the parameters for the various models studied.

We will now examine various features of these models that relate to their magnetic field morphologies. We will also compare these models to the observations of Uranus' and Neptune's fields.

### 2.4.2 Surface Magnetic Power Spectra

The surface magnetic power spectra for Earth and the four giant planets was shown earlier in Figure 2.3. This plot demonstrated the non-axisymmetry and non-dipole nature of Uranus' and Neptune's fields. In Figure 2.6 we compare the surface power spectra of the models in Table 2.5 to the spectra of Earth, Uranus and Neptune. It is immediately obvious that only two of the models (models 3 and 4) have similar surface power spectra to the observations of Uranus and Neptune. All the other models produce fields that are similar to Earth's in that they are axially-dipolar dominated. The two Uranus- and Neptune- like models have large inner-outer core magnetic diffusivities. This means

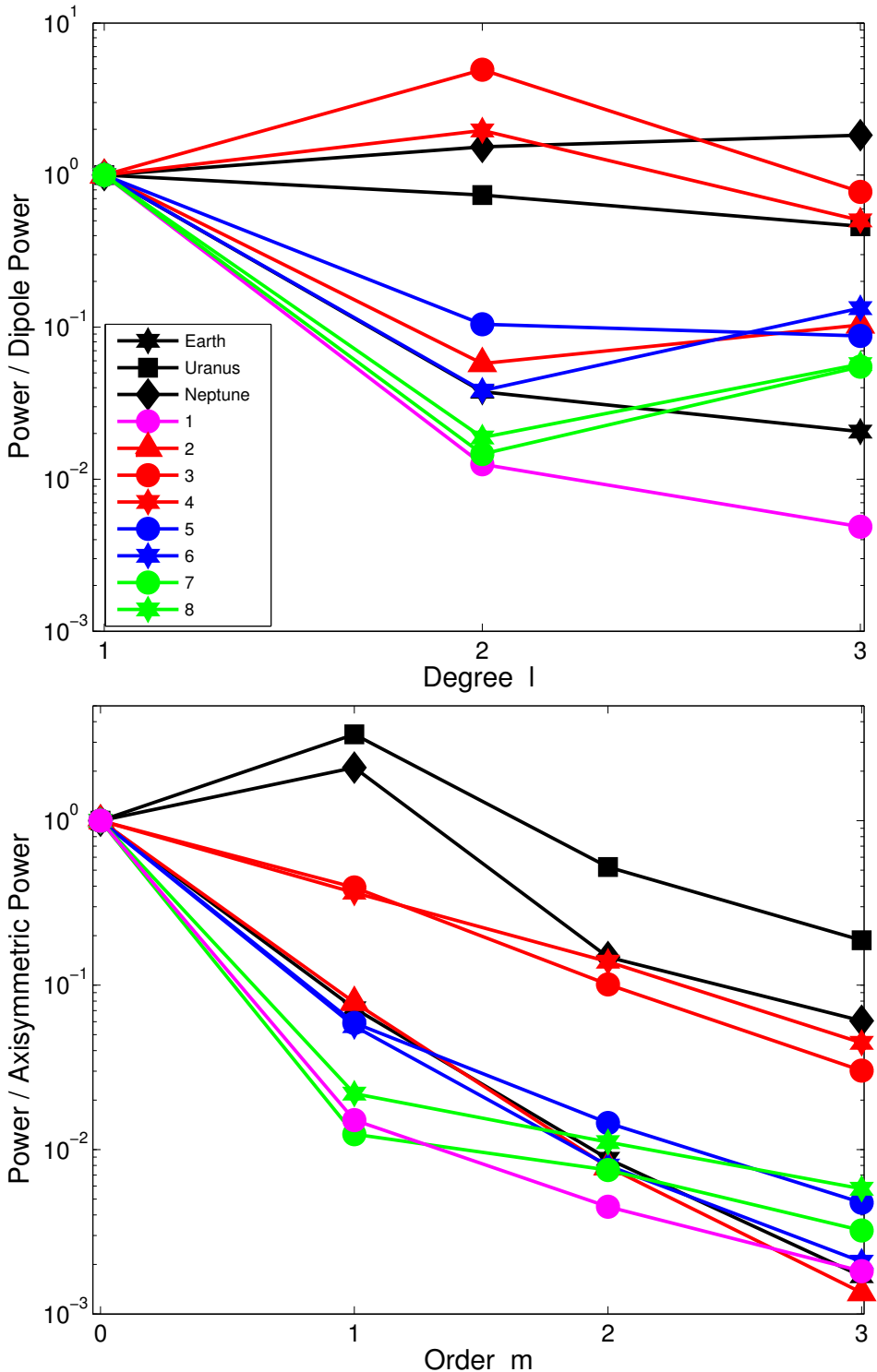


**Figure 2.6:** Average surface magnetic power spectra for models with solid inner cores. The parameters for models 1-8 are given in Table 2.5. The observational models for Earth, Uranus and Neptune are also shown for comparison. The legend in the top plot also applies to the bottom plot.

that their inner cores are much less conducting than their fluid outer cores. These results indicate that only changing the size of the inner core does not produce non-axisymmetric, non-dipolar fields; the inner core must also lose the influence it possesses based on its conductivity.

The surface power spectra in Figure 2.6 all assume that the top of the dynamo source region is at 0.75 planetary radii. If we assume the dynamo is located much deeper in the planet, say near the base of the ice layer (as suggested by Ruzmaikin and Starchenko (1991) to explain the anomalous fields) then, the surface power spectra would contain much smaller power in the higher degree components (quadrupole and octupole) and none of the models would match the surface power spectra of Uranus and Neptune. Our models indicate that the observed power in higher degree components requires that the dynamo source region be near the surface of the planets.

It should also be noted that the power spectra for the models are averages over a diffusion time whereas the observational models are from one instant in time. The magnetic fields from models 3 and 4 are quite variable in time and do not always possess power spectra similar to their averages. The time variability of the fields will be examined in later sections. The other models in Table 2.5 are also variable in time, but their power spectra at specific times tend to be much more similar to their average power spectra (*i.e.* they are not as variable as the non-dipolar, non-axisymmetric models).

### 2.4.3 Eccentric Dipole Models

Eccentric dipole models for the planets were given earlier in Table 1.2. Whereas Earth, Jupiter and Saturn possessed small dipole tilts and offsets, Uranus' and Neptune's fields, in contrast, had large tilts and offsets. A large dipole tilt is the result of relatively large equatorial dipole components ( $g_1^1$  and  $h_1^1$ ), and a large offset is a result of large quadrupole terms. These models do not take higher degree components into consideration at all and are therefore best used for planets with axially-dipolar dominated fields. If these models are implemented for magnetic fields with very large quadrupole components, they can result in dipole offsets that are larger than the planetary radius (suggesting the source of the magnetic field is actually outside of the planet). This is not a realistic effect and just a result of how poor an eccentric dipole model can be at characterizing a field. However, since these models are used to characterize observations, we will compare eccentric dipole models from our numerical models to the observational models.

Figure 2.7 plots the average eccentric dipole tilts and offsets for the models in Table 2.6. Again we see that models 3 and 4 are the only ones that produce large dipole tilts and offsets similar to the observations. Our models with  $\eta_{io} = 1$  indicate that thin shell geometries produce dipole tilts that are slightly larger than a model with an Earth-like shell thickness (model 1), but there does not appear to be a clear trend with shell thickness since the models with the thinnest shells ( $r_{io} = 0.9$ ) have smaller dipole tilts and offsets than models with thicker shells ( $r_{io} = 0.7$  and 0.8). If we only consider the average surface power and eccentric dipole data in the models, then model 3 is most similar to Neptune's observed field and model 4 most resembles Uranus' field. However, since both models are so variable in time, it may be unwise to rely on average data to distinguish between the two, since both models can reproduce power spectra and eccentric dipole models very similar to both planets at specific time steps in the evolution. This may also be true for the planets. Slightly different dynamo geometries may not be required to explain the small differences in Uranus' and Neptune's surface spectra and dipole tilt and offsets. Since the fields are so variable in time, it may be that both planets possess similar dynamo geometries, but are not displaying the same instant field.

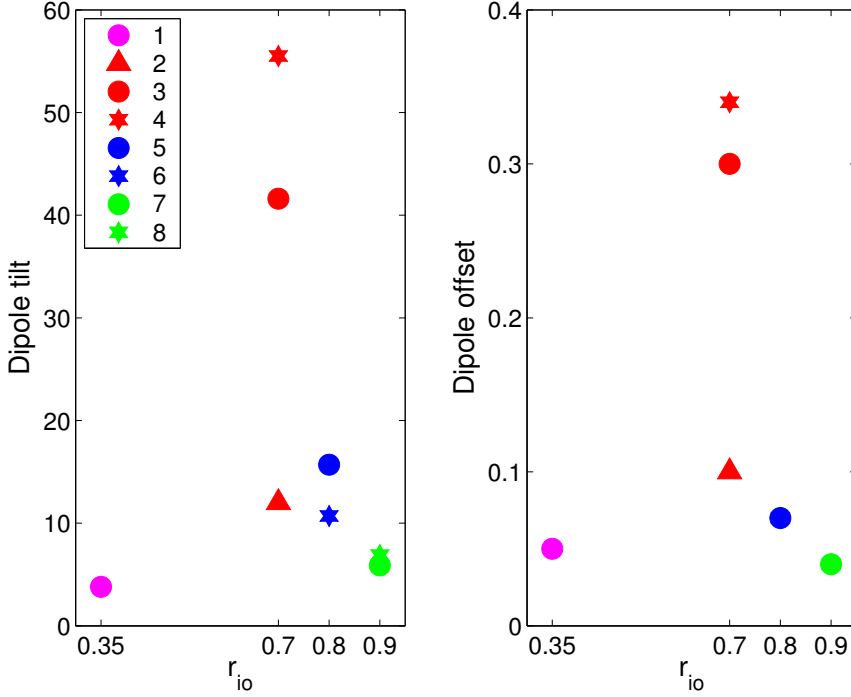


**Figure 2.7:** Average eccentric dipole tilts (left) and offsets (right) for models with solid inner cores. The parameters for the models are given in Table 2.5. The absolute value of the dipole tilt is plotted on the left rather than the actual dipole tilt since we are interested in how large the tilt is rather than its polarity. At  $r_{io} = 0.8$  and  $0.9$ , there appears to be only a single model in the dipole offset plot (right), however, this is because the individual models at the specific radii have offsets that are so similar, they plot on top of each other. The legend in the left plot also applies to the right plot.

Figure 2.8 plots the eccentric dipole models vs. time for models 2, 3 and 4. This figure demonstrates the time variability of the field morphologies quite nicely. Notice that the model with  $\eta_{io} = 1$  (model 2) is much less variable than the two models with less conducting inner cores (models 3 and 4). Also notice that there are points in time when the dipole offsets of models 3 and 4 are larger than the planet radius, illustrating the lack of physical interpretation of eccentric dipole models. The dipole tilts for models 3 and 4 show high variability in magnitude and polarity. This means the fields experience 'excursions' and 'reversals' quite frequently. This relays back to the possible explanation for the fields given by Schulz and Paulikas (1990) discussed in section 2.3. Although it is unlikely that we would observe both Uranus' and Neptune's fields in the middle of a reversal if they possessed Earth-like reversal frequencies, it appears likely that we would observe their fields in reversal (or large excursion) if they have similar reversal frequencies as numerical models 3 and 4, since these models rarely maintain stable axially-dipole configurations.

#### 2.4.4 Magnetic Energy

In the previous sections, we examined characteristics of our numerical models that related to the potential field produced outside the dynamo source region. This allowed comparison of our numerical models to observations. A luxury of numerical modeling is that we can also examine the characteristics of the magnetic fields inside the dynamo source region. This allows us to study the

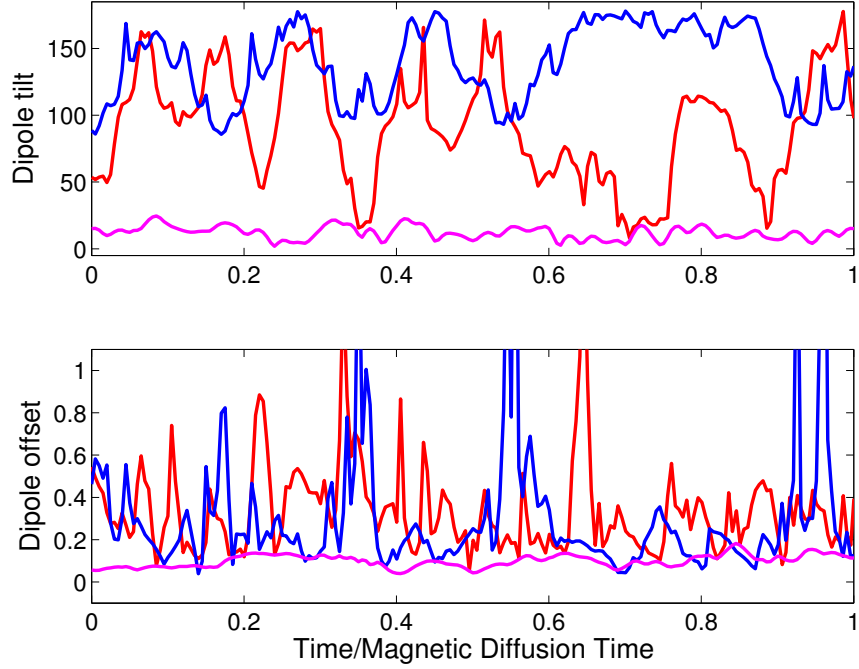


**Figure 2.8:** Eccentric dipole models vs time for models 2 (magenta), 3 (blue) and 4 (red). Here the dipole tilt is plotted rather than the absolute value of the dipole tilt as was done in Figure 2.7 in order to examine the polarity reversals of the fields. Dipole offset is given in units of planetary radii.

---

dynamics producing the potential fields we see at spacecraft altitude.

We begin by examining the energy in the magnetic fields, which we define in terms of the non-dimensional mean square field intensity:

$$E_B = \int_V |\mathbf{B}|^2 dV, \quad (2.11)$$

where  $V$  is the non-dimensional volume of the fluid outer core. Because of the orthogonality of spherical harmonics, the energy can be separated into its toroidal and poloidal components:

$$E_B = E_{BT} + E_{BP} = \int_V |\mathbf{B}_T|^2 dV + \int_V |\mathbf{B}_P|^2 dV, \quad (2.12)$$

where  $E_{BT}$  and  $E_{BP}$  are the energy in the toroidal and poloidal fields respectively. We can further separate the toroidal and poloidal energies into their axisymmetric and non-axisymmetric components. Figure 2.9 plots the average ratio of non-axisymmetric to total magnetic energy for the models in Table 2.6. The poloidal fields in all the models have a significant non-axisymmetric component, although only three of the models (3,4, and 5) have a non-axisymmetric component that is larger than the axisymmetric component (i.e. non-axisymmetric / total > 0.5). The potential field that is observable outside the source region is an extension of this poloidal field, so the fact that the surface power spectra and eccentric dipole models were more dominated by axisymmetric components than the energy in the dynamo source region (for all but models 3 and 4), implies that the smaller scale fields that are not represented by the power spectra and eccentric dipole models possess a higher level of non-axisymmetry than the large scale components in the poloidal field. This is especially

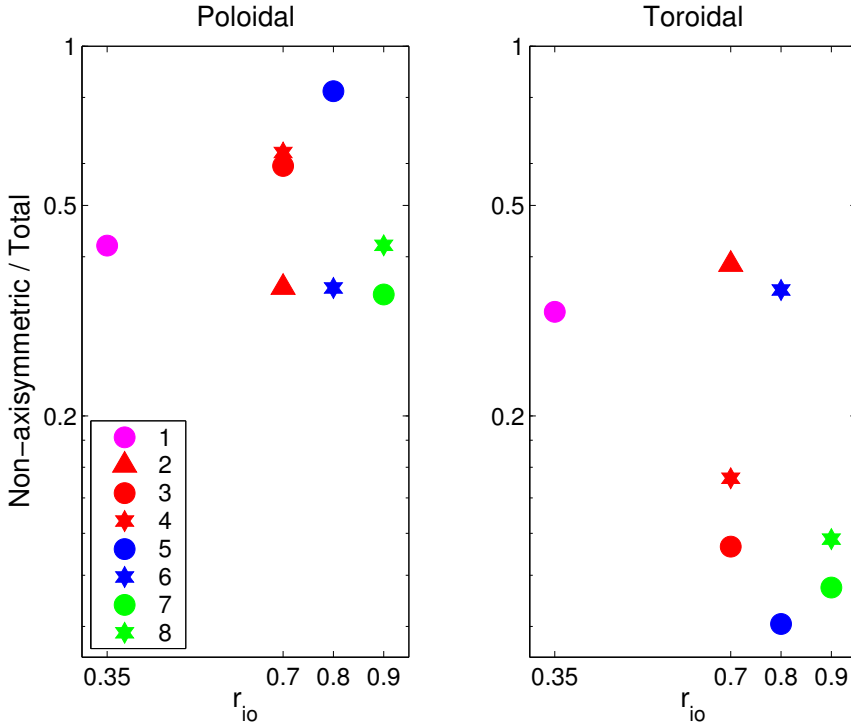


**Figure 2.9:** Average non-axisymmetric magnetic energy vs.  $r_{io}$  in the poloidal (left) and toroidal (right) fields for the models with solid inner cores. The energy is plotted on a log scale and the parameters for the models are found in Table 2.5. The legend in the left plot also applies to the right plot.

true for model 5 which produced a very Earth-like surface power spectrum but possesses the largest non-axisymmetric poloidal energy component of all the models.

We see a different story when we examine the energy in the toroidal field (which is not observable outside the dynamo source region). Here, all the fields are dominated by their axisymmetric components, however to varying degrees. The three models with poloidal energies dominated by non-axisymmetric components have toroidal fields that are very axisymmetric. It also appears that models with very thin shells ( $r_{io} = 0.9$ ) possess very axisymmetric toroidal fields. The differences in symmetry between the toroidal and poloidal energies clearly demonstrates that different processes are responsible for their maintenance.

We can also examine the time dependence of the magnetic energy in the models. Figure 2.10 plots the magnetic energy vs. time for the Earth-like model 1. This plot demonstrates the variability of the energies' magnitudes and also shows that the level of non-axisymmetry seen in the average energy plotted for this model in Figure 2.9 is representative of the non-axisymmetry at any point in time (i.e. the average is representative of the field at any time). Figures 2.11 and 2.12 plot the magnetic energy in the toroidal and poloidal fields vs. time for models 2 and 3 respectively. These models have the same inner core size ( $r_{io} = 0.7$ ) but different inner core conductivities. Model 2, which has  $\eta_{io} = 1$ , has a very similar magnetic energy distribution as the Earth-like case seen in Figure 2.10. In contrast, model 3 which has  $\eta_{io} = 100$ , has a very different energy distribution. The strong non-axisymmetric component is evident in the poloidal energy plot, as it was in the average energy plots in Figure 2.9 and the toroidal field has a much smaller non-axisymmetric en-

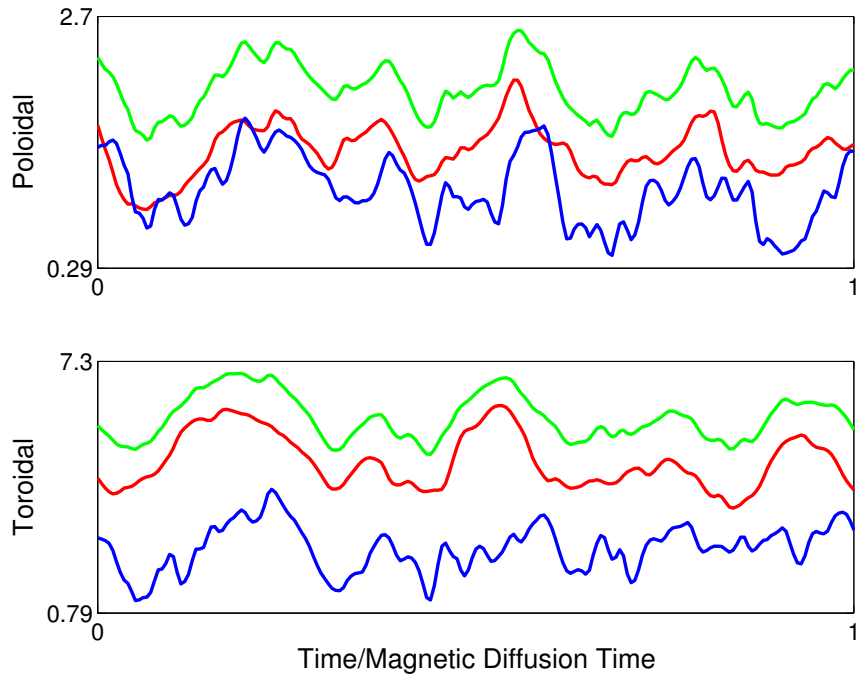


**Figure 2.10:** Magnetic energy vs. time for model 1. The axisymmetric (red), non-axisymmetric (blue) and total (green) energy are shown for the poloidal (top) and toroidal (bottom) components of the field. Energy is plotted on a log scale.

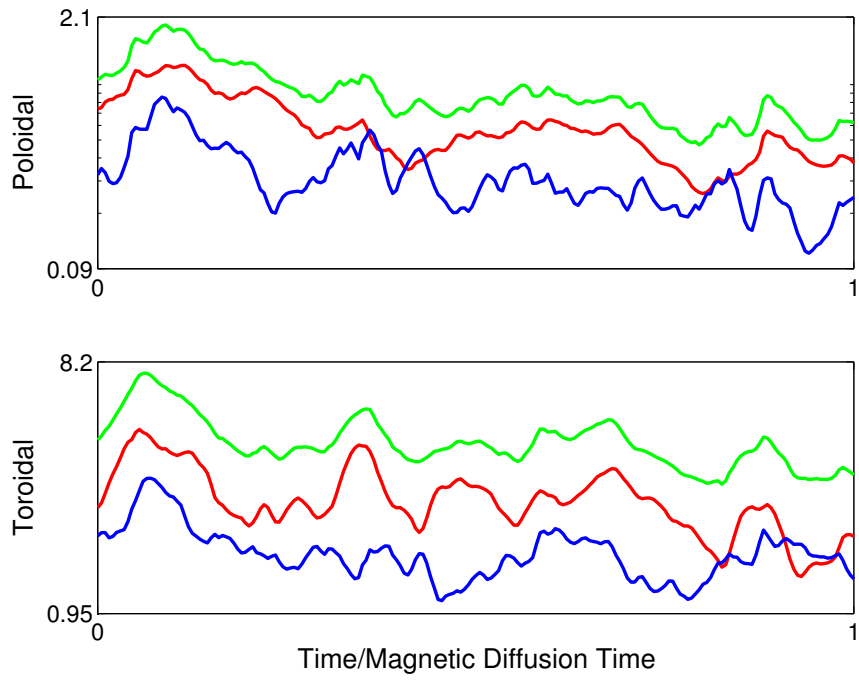


**Figure 2.11:** Same as 2.10 except for model 2.

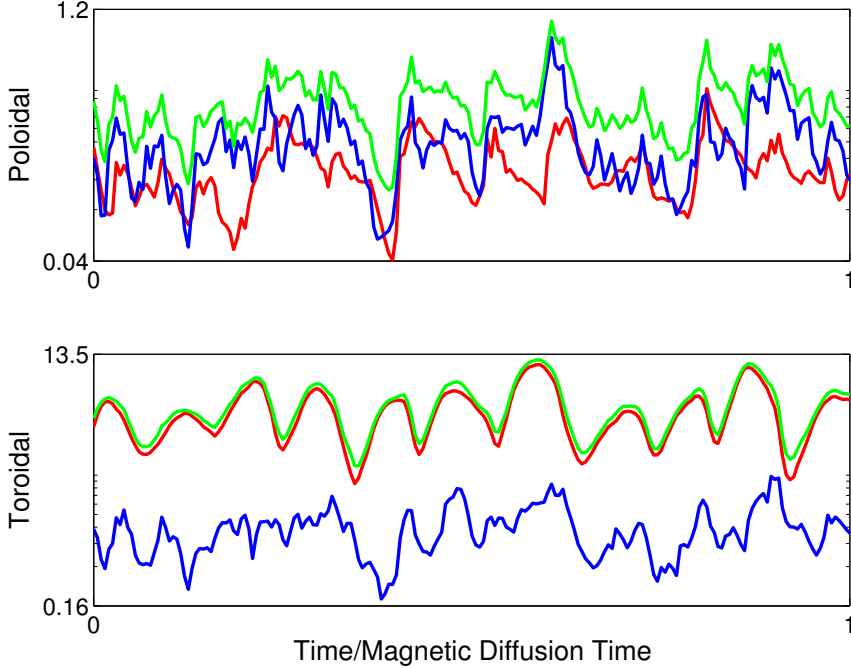


**Figure 2.12:** Same as 2.10 except for model 3.

ergy component than model 2. It appears that reducing the conductivity of the inner core, promotes the creation of axisymmetric toroidal field and non-axisymmetric poloidal field. This suggests that the influence of the inner core on field morphology (discussed in section 1.3.4) is different for the toroidal and poloidal field components.

## 2.4.5 Kinetic Energy

Similar to the magnetic energy, we can define the non-dimensional kinetic energy in terms of the mean square field intensity and separate it into its toroidal and poloidal components:

$$E_k = E_{kT} + E_{kP} = \int_V |\mathbf{v}_T|^2 dV + \int_V |\mathbf{v}_P|^2 dV, \quad (2.13)$$

where  $E_{kT}$  and  $E_{kP}$  are the energy in the toroidal and poloidal velocity fields respectively, and  $V$  is the non-dimensional volume of the outer core. Figure 2.13 plots the average ratio of non-axisymmetric to total kinetic energy for the models in Table 2.6. All the models have poloidal kinetic energies dominated by their non-axisymmetric components (note the limits on the vertical axes). This is expected since convection produces a dominantly non-axisymmetric velocity pattern. In contrast, the toroidal velocity fields are dominated by their axisymmetric components, with the Earth-like case having the largest non-axisymmetric toroidal energy component of all the models.

Figures 2.14, 2.15 and 2.16 plot the kinetic energy in the toroidal and poloidal fields vs. time for models 1,2 and 3 respectively. Like the magnetic energy, the average kinetic energy distributions are representative of the fields at any point in time. The poloidal velocity fields are so non-axisymmetric that their curves are barely visible under the total energy curves in the plots for all three models.

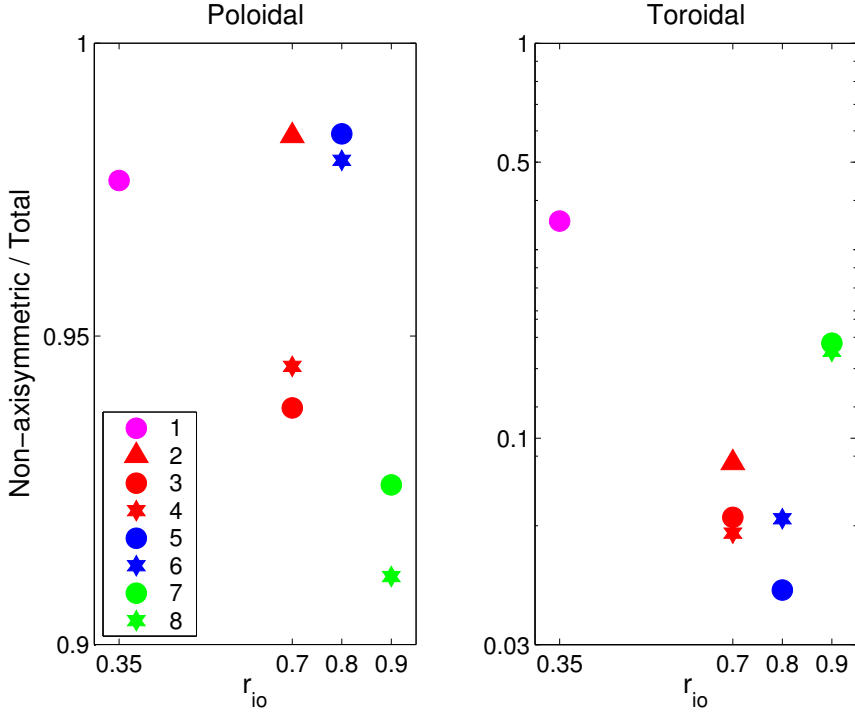


**Figure 2.13:** Average non-axisymmetric kinetic energy vs.  $r_{io}$  in the poloidal (left) and toroidal (right) fields for the models with solid inner cores. The energy is plotted on a log scale and the parameters for the models are given in Table 2.5. Note the difference in vertical axes limits for the poloidal and toroidal energy plots. The legend in the left plot also applies to the right plot.

Similarly, the axisymmetric toroidal velocity is barely visible under the total toroidal energy curves for models 2 and 3. The only major difference that can be seen between the three models is the level of axisymmetry of the toroidal fields: the model with Earth-like inner core size (model 1) has a much larger non-axisymmetric component than the models with  $r_{io} = 0.7$  (models 2 and 3).

#### 2.4.6 Magnetic Field Plots

For a more visual representation of the fields, Figure 2.17 plots the radial magnetic field at the top of the dynamo source regions for some of the models in Table 2.5. The three models shown with  $\eta_{io} = 1$  (models 1, 2 and 7) have radial fields dominated by axisymmetric dipole components. Differences between these models are evident in the smaller scale features of the fields. The models with larger inner cores (thinner fluid outer shells) have intense small-scale flux patches near their equators (models 2 and 7) which are not seen in the Earth-like model (model 1). Although these are observable in the numerical models, they would not be resolvable in the spacecraft observations of the fields due to the sparse data set and high altitude of the spacecraft. The non-axisymmetric, non-dipolar nature of model 3 that we discussed in previous sections is also demonstrated in this figure.

To aid in the visualization of the magnetic field inside the dynamo source region, Figure 2.18 plots the axisymmetric field in this region for the same models and time steps as Figure 2.17. Here we see that although models 1, 2 and 7 all produce dipolar dominated axisymmetric poloidal fields,

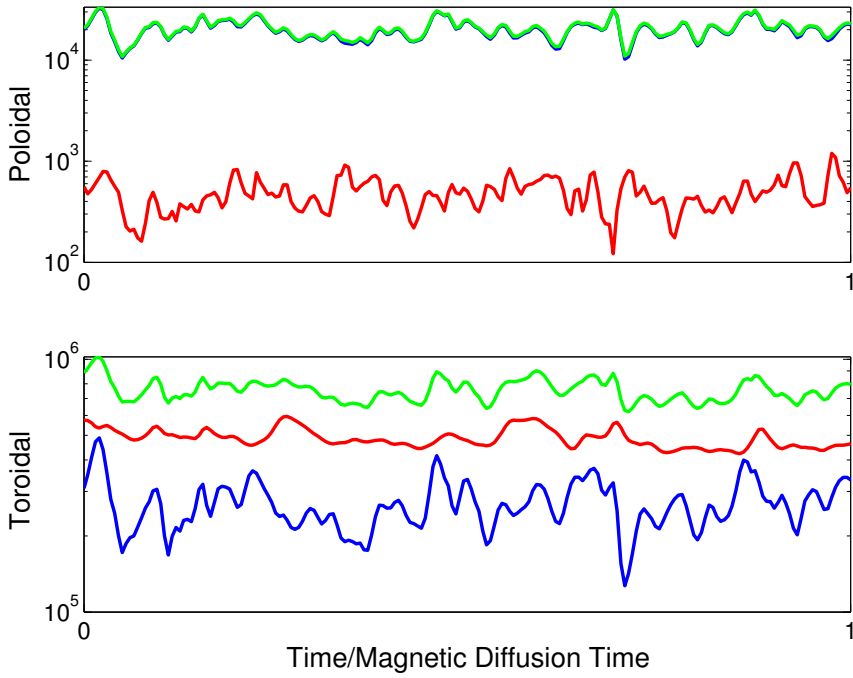


**Figure 2.14:** Kinetic energy vs. time for model 1. The axisymmetric (red), non-axisymmetric (blue) and total (green) energy are shown for the poloidal (top) and toroidal (bottom) components of the field. Energy is plotted on a log scale.

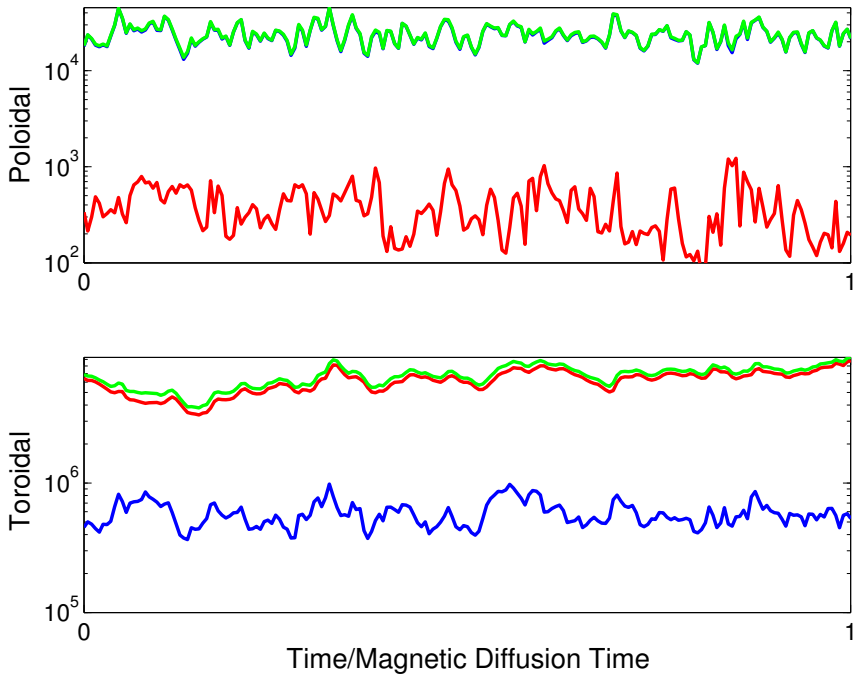


**Figure 2.15:** Same as 2.14 except for model 2.

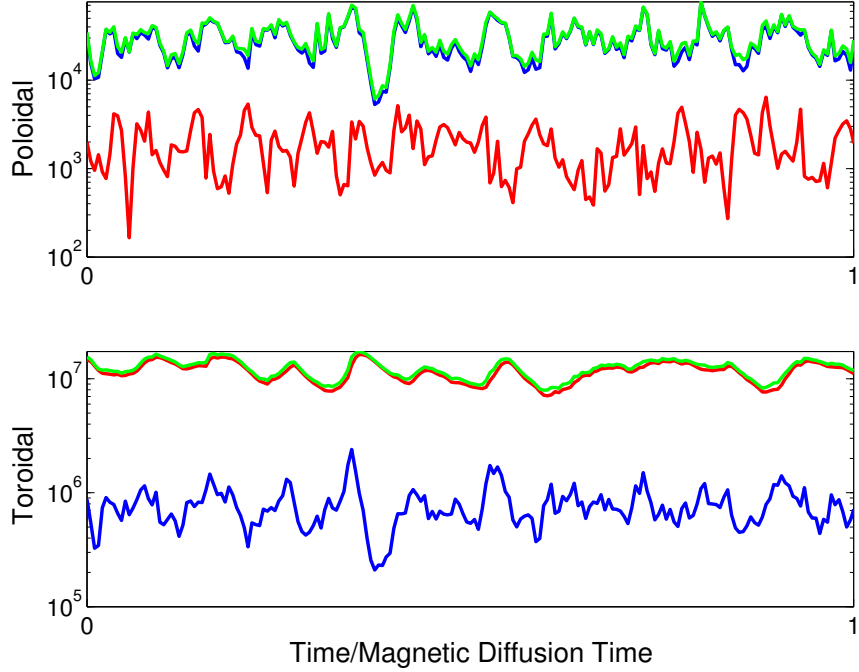


**Figure 2.16:** Same as 2.14 except for model 3.

their toroidal fields are quite different. The models with larger solid inner cores appear to have more small scale structure in their toroidal fields than the Earth-like model. An obvious difference between model 3 and the others is the lack of toroidal field penetrating the solid inner core. This is expected since the inner core has a much smaller conductivity in this model. The axisymmetric poloidal field in model 3 is clearly more complex than a dipole field, however it should be kept in mind that model 3's poloidal field is dominated by non-axisymmetric components, and therefore this plot is not a good visualization of the total poloidal magnetic field for this model.

#### 2.4.7 Velocity Field Plots

Figure 2.19 plots the velocity field for models 2 and 3. Both models have the same  $r_{io}$  and  $Ra$  but different  $\eta_{io}$ . The axisymmetric field plots show that the model with a more insulating inner core experiences stronger differential rotation. There also appears to be a stronger axisymmetric poloidal flow. In contrast, the non-axisymmetric plots suggest that the more intense convective motions have a smaller scale and are found more homogeneously throughout the core in model 2. Since these models have the same Rayleigh number and shell thickness, they are 'driven' by the same buoyancy force. It appears that models with more insulating inner cores partition more of their kinetic energy into axisymmetric velocity components than models with conducting inner cores.

Another interesting feature of model 3 is that the contours of differential rotation are slightly tilted with respect to the rotation axis. This is correlated with a strong axisymmetric poloidal flow across the equator outside the tangent cylinder. Examining the axisymmetric temperature perturbations in this region (see Figure 2.20), suggests that this might be the result of a thermal wind.

These differences are due only to the change in conductivity of the inner core. They are most

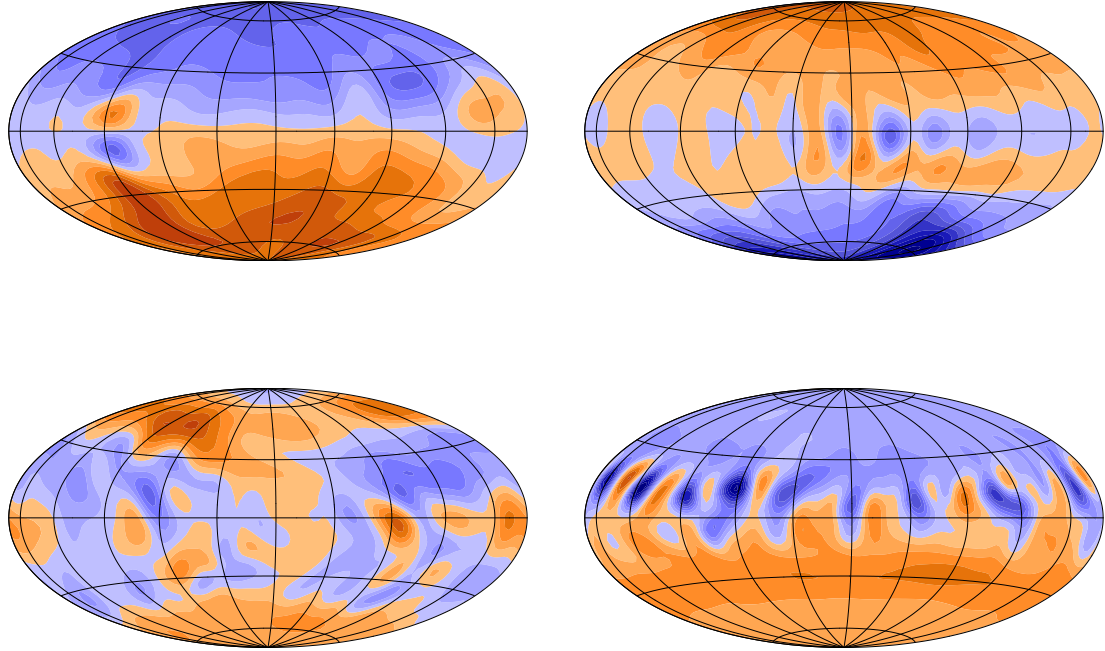


**Figure 2.17:** Filled contours of the radial magnetic field at the top of the dynamo source region at one instant in time for models 1 (top left), 2 (top right), 3 (bottom left) and 7 (bottom right). The different colors represent different field directions.

likely the direct result of the change in magnetic field structure resulting from the change in conductivity of the inner core rather than a direct result of the inner core's conductivity. This demonstrates that our models are strong field dynamos in the sense that the magnetic field influences the form of the velocity field.

#### 2.4.8 Summary of Solid Inner Core Models

The purpose of section 2.4 was to determine the effect of thin shell geometry on the magnetic field morphology. We have shown that taking an Earth-like set-up (fluid convecting shell surrounding a solid conducting inner core) and just making the inner core larger (hence the fluid shell thinner) does not result in a large-scale change in field morphology. This geometry still produces fields dominated by their axially-dipolar components at spacecraft altitude, and hence it does not appear that Uranus' and Neptune's fields can be explained by this geometry. There are some differences in the small scale features and toroidal field inside the shell, however neither of these is observable at spacecraft altitude.

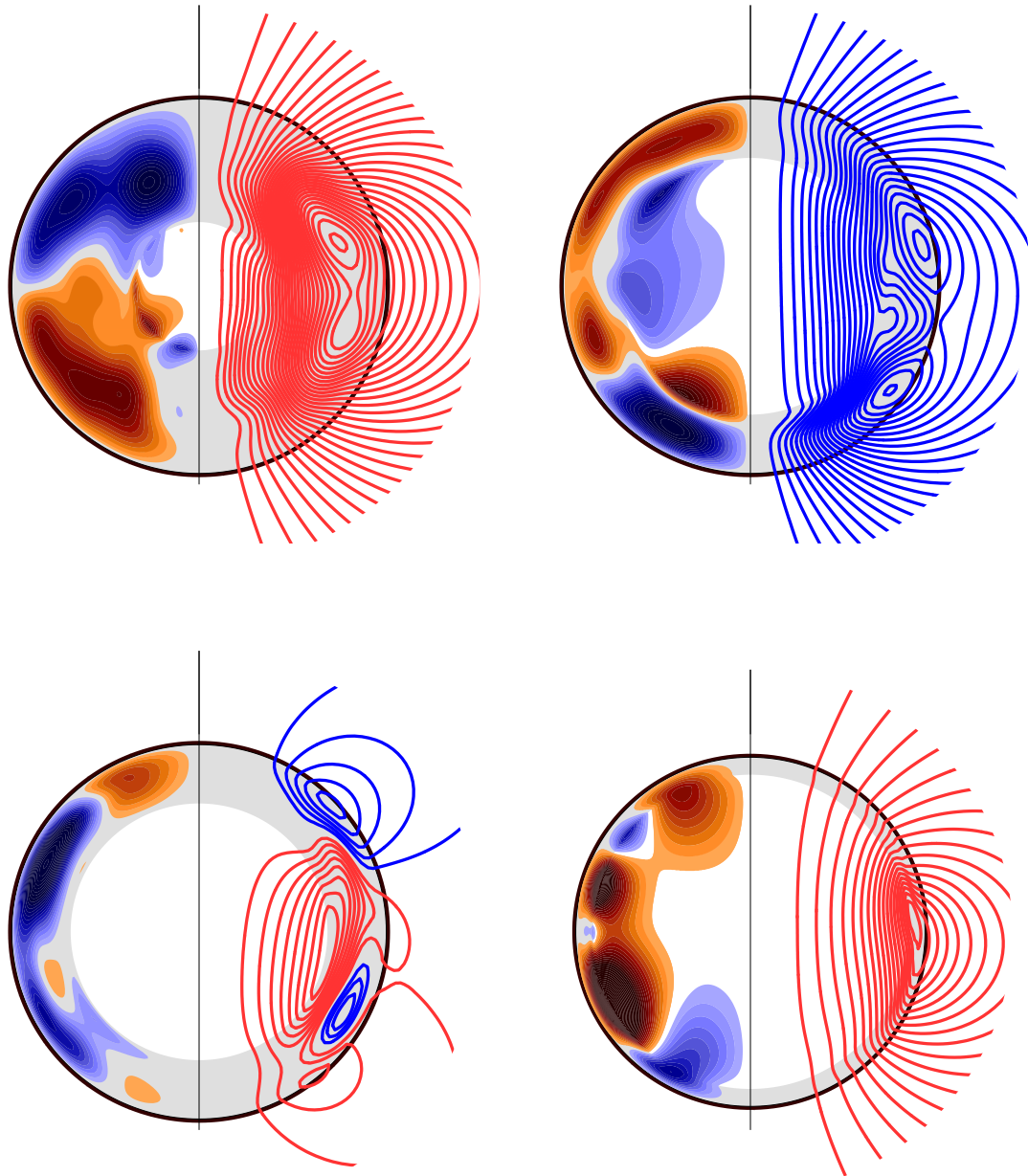


**Figure 2.18:** Axisymmetric magnetic fields in a meridional slice through the dynamo source region at one instant in time for models 1 (top left), 2 (top right), 3 (bottom left) and 7 (bottom right). Contours of the toroidal field are shown in the left half and streamlines of the poloidal field are shown in the right half of the plots. The different colors represent different field directions. The grey shell is the fluid outer core, the inner white region is the solid inner core, the thick black circle is the top of the dynamo source region and the black vertical line represents the rotation axis.

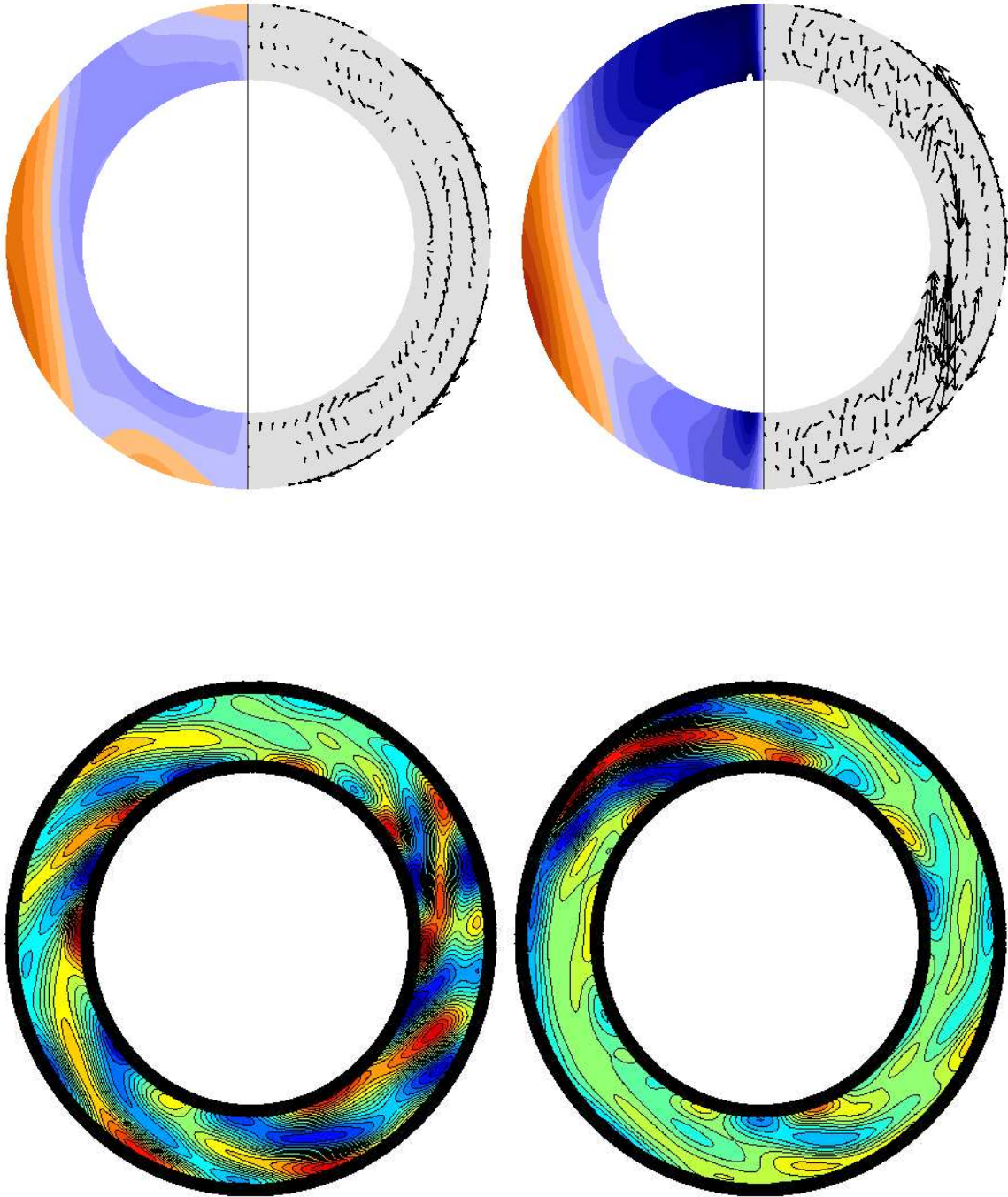


**Figure 2.19:** Velocity field for models 2 (left) and 3(right). The Axisymmetric field in a meridional slice through the dynamo source region at one instant in time is plotted in the top row. Contours of the axisymmetric toroidal field are plotted in the left half and flow vectors of the axisymmetric poloidal field are plotted in the right half. The non-axisymmetric poloidal field in a slice through the equator is shown in the bottom row. The contours are of the curl of the horizontal velocity field.

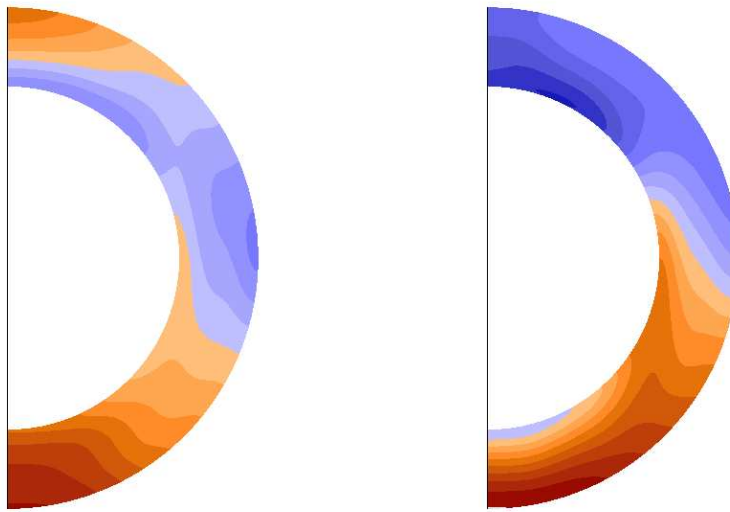


**Figure 2.20:** Contours of the axisymmetric temperature perturbation field in a meridional slice through the dynamo source region at one instant in time for models 2 (left) and 3 (right).

We did however, find a set-up that does produce Uranus- and Neptune- like fields. If we work in a thin shell geometry and make the inner core much less conducting than the outer core, then we can produce non-dipolar, non-axisymmetric fields. It appears that if the inner core loses the influence it has as a result of its conductivity, then it can have a significant effect on the morphology of the resultant magnetic fields, as well as on the velocity fields in the outer core. This effect was seen most clearly by comparing the magnetic and kinetic energy components of models 1,2, and 3, where we saw that the size of the inner core has a significant effect on the toroidal velocity fields produced, and the inner core conductivity has a significant effect on the magnetic fields produced (especially the poloidal field).

Although this set-up produces fields similar to Uranus and Neptune, it is not a realistic geometry for these planets. Since the convecting shell must be near the planet surface (i.e. top of shell at about 0.75 planetary radii), it is impossible that the interiors of these thin shells are solid in Uranus and Neptune based on physical and chemical properties of these planets. However, it is possible that the true physical nature of the region interior to Uranus' and Neptune's convecting shells somehow mimics the effect of an insulating solid inner core on the field morphologies produced. This will be examined in the next section.

## 2.5 Dynamos With Stably-Stratified Fluid Inner Cores

### 2.5.1 Model Setup

In this section we move to the next phase of our dynamo model geometry by replacing the large solid inner core with a stably-stratified fluid core. We still include a small solid inner core ( $r_{io} \approx 0.17$ ) below the stably-stratified fluid core for numerical convergence issues, but this solid inner core may also be realistic if Uranus and Neptune contain the 'rock' layer illustrated in Figure 2.1. We make the conductivity of this solid inner core equal to the outer core conductivity, but do not expect it to

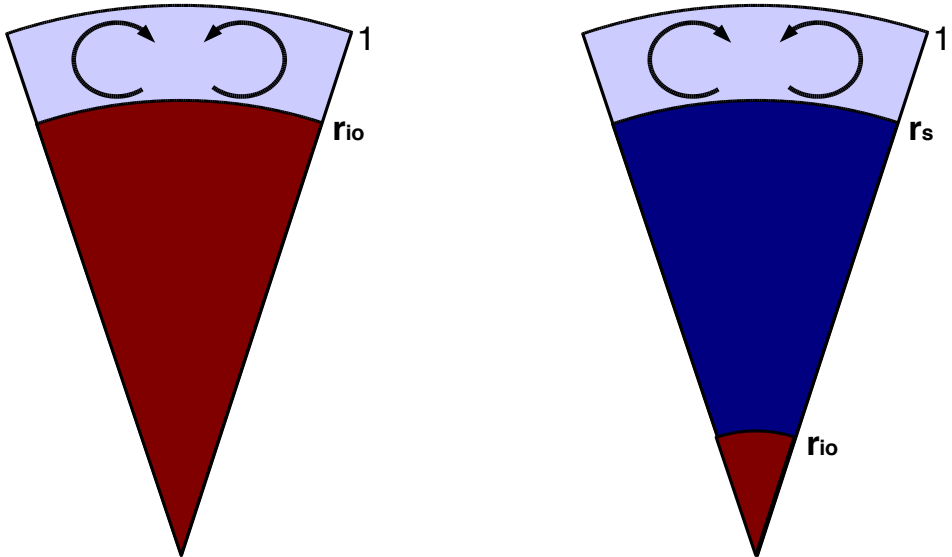


**Figure 2.21:** Dynamo model geometries for a solid inner core model (left) and a stably-stratified fluid inner core model (right). The convecting shell is shown in light blue, the stably-stratified fluid region is shown in dark blue, and the red regions are the solid inner cores.  $r_{io}$  is the non-dimensional inner core radius and  $r_s$  is the non-dimensional stable shell radius.

affect the solutions greatly since this solid inner core is far removed from the dynamo generation region. A sketch comparing the two geometries used in our dynamo models is given in Figure 2.21.

In the planets, this stable layer is most likely due to a compositional gradient and since compositional differences exist, convection due to compositional buoyancy may be important in the dynamo problem. However, in this work, we are interested in investigating the effect of a stably-stratified fluid inner core on the magnetic field morphology, not the stability of the problem, nor the interplay between compositional and thermal buoyancy. We therefore choose to numerically model the buoyancy and stable stratification as a thermal effect. This will also allow for easier comparison to the solid inner core models of section 2.4 and since compositional effects are treated nearly identically to thermal effects in the governing equations, it is not a severe simplification. Some other numerical dynamo models have composition as an added variable and do solve for it (*e.g.* Glatzmaier and Roberts (1996a)), while others choose to define a new variable called the buoyancy variable  $C = \xi + T$  (Wicht and Olson, 2004), and use this variable in their numerical model instead of temperature.

We use the background state to implement the stable stratification. Clearly little is known about the stably-stratified layer in Uranus and Neptune. We make the conductivity of the stable shell equal to that of the convecting shell so that the only difference between the two layers is their stability to convection. The method of maintaining stability and instability is similar to that of Zhang and Schubert (1996, 2000, 2002) (studies of thermal convection in the presence of stable layers) and Jones *et al.* (1995) (in which a thin stable layer near the core-mantle boundary was incorporated in a 2.5D geodynamo model), although our actual stability profiles are different. The profiles in our

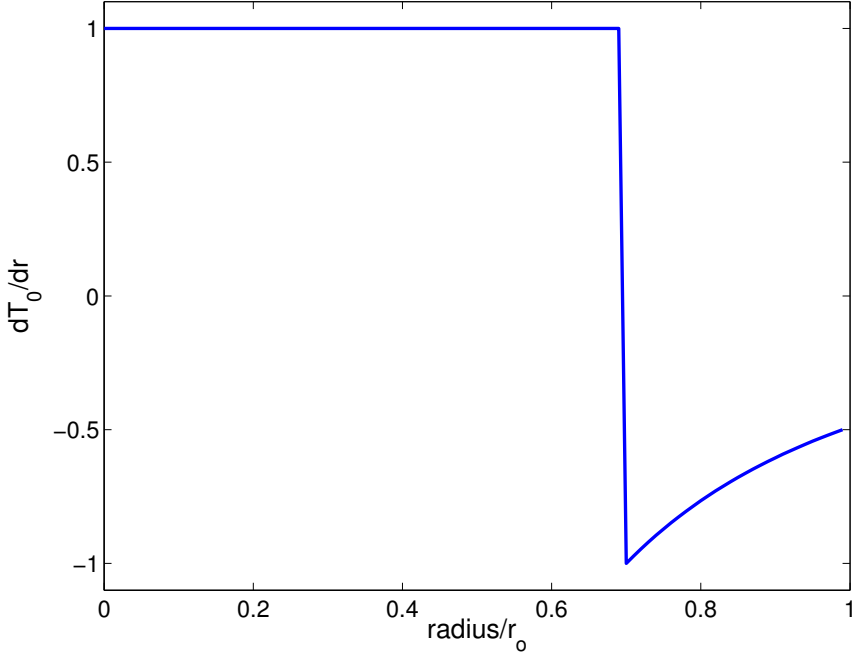


**Figure 2.22:** Background non-dimensional temperature gradient in a numerical model with  $r_s = 0.7$ . A model with a solid inner core instead of a stably-stratified inner core and the same convective shell thickness would have the same background temperature gradient in the region  $0.7 \leq r \leq 1$ .

---

models are chosen for their simplicity and comparability to models with solid inner cores since the background buoyancy profiles in Uranus and Neptune are unknown.

In a model with a non-dimensional stable shell radius of  $r_s$ , we impose a super-adiabatic background temperature gradient in the unstable layer consistent with our fixed heat flux boundary conditions:

$$\frac{dT_0}{dr} = -\left(\frac{r_s}{r}\right)^2, \quad (2.14)$$

and in the stable layer, we impose a sub-adiabatic temperature gradient:

$$\frac{dT_0}{dr} = 1. \quad (2.15)$$

where the equations are non-dimensionalized. We choose the unstable background temperature gradient so that the temperature profile is the same as it would be if this unstable shell were surrounding a solid inner core. This is done so easier comparison can be made to our thin shell models with solid inner cores. The profile in the stable layer is arbitrary, and chosen for simplicity. Since we model it as a thermal stability, one can think of this stable region as possessing heat sources distributed in such a way that the region maintains its stability to convection even though the conductive temperature gradient in the absence of the heat sources is super-adiabatic. This is meant to mimic the effect a compositional stratification would have on this region. Figure 2.22 shows the background buoyancy profile in our models.

We created numerical models with various values for  $r_s$  and  $Ra$ . Table 2.6 lists the parameters for the models studied. In the following sections we will examine several features of these models that

**Table 2.6:** Stably-stratified inner core model parameters.

Model #	$r_s$	$Ra$
1	0.5	15000
2	0.5	18000
3	0.6	12000
4	0.6	15000
5	0.6	18000
6	0.7	18000
7	0.7	24000
8	0.8	40000

relate to their magnetic field morphologies. We will also compare these models to the observations of Uranus' and Neptune's fields.

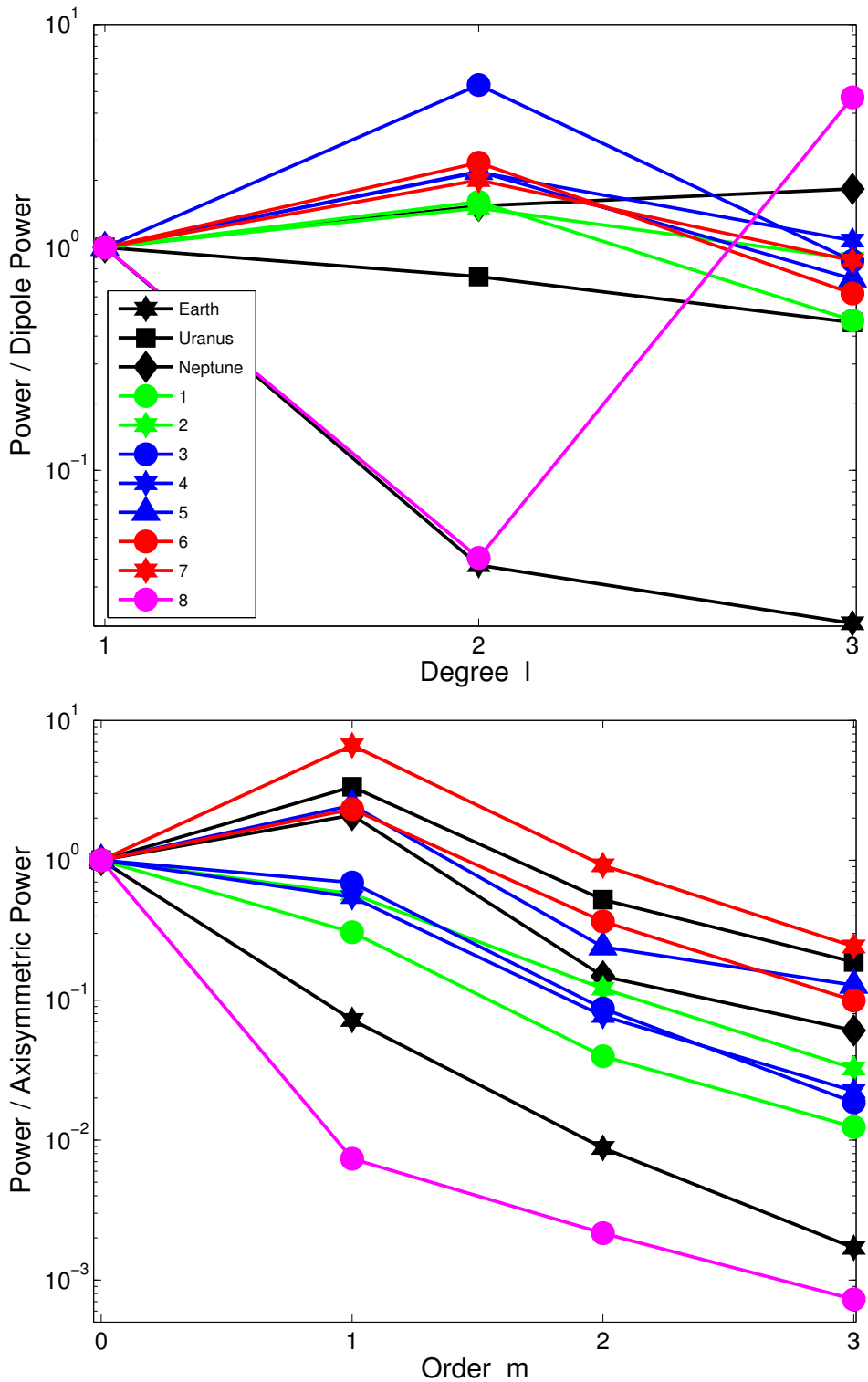
### 2.5.2 Surface Magnetic Power Spectra

Figure 2.23 compares the average surface magnetic power spectra of the models in Table 2.6 to the observational models of Uranus and Neptune. It is evident that all the models in Table 2.6, except model 8, have magnetic fields dominated by non-axisymmetric, non-dipolar components, similar to those of Uranus and Neptune. Although model 8 does not have a Uranus- or Neptune- like field, it also doesn't have an Earth-like field because of the dominant octupole component.

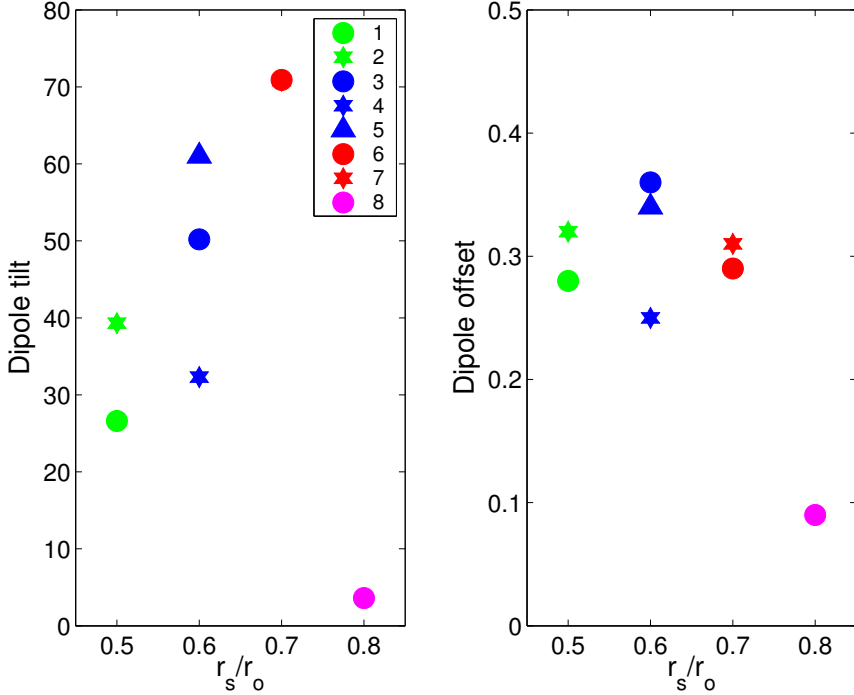
### 2.5.3 Eccentric Dipole Models

Figure 2.24 plots the average eccentric dipole tilts and offsets for the models in Table 2.6. We find that, aside from model 8, thin shell models surrounding stably-stratified inner cores produce larger dipole tilts and offsets than the Earth-like numerical model shown in Figure 2.7 (magenta circle). There appears to be a trend of higher average dipole tilt with thinner shell for stable shell radii in the range  $0.5 \leq r_s \leq 0.7$ , however this trend does not appear in the dipole offset. This suggests that convective shell thickness might affect the symmetry of the dipole component more than it affects the amounts of smaller scale structure (such as the quadrupole component) relative to the large scale dipole component. A quick comparison of the averages in this plot, to the observational values for Uranus and Neptune given in Table 1.2 suggests that models with  $r_s = 0.6$  are most similar to Uranus' and Neptune's fields, and that matching the offset of Uranus (0.352 planetary radii) is easier than the larger offset of Neptune (0.485 planetary radii). However, we should be careful in comparing averages of quite variable properties to observations at a single time.

To examine the time-variability of these models, Figure 2.25 plots the eccentric dipole tilts and offsets vs. time for models 3, 7 and 8. The difference between model 8 and the other models is again evident in this plot. Since eccentric dipole models don't take into account octupole or higher degrees, the octupole nature of model 8 is not evident in this figure. According to these eccentric dipole models, model 8 has a field very similar to Earth's field, with small dipole tilt and offset. Models 3 and 7 are quite variable with the main differences seen in their dipole offsets. Model 3 appears to have larger variations in this property. Notice that both models 3 and 7 can match the



**Figure 2.23:** Average surface magnetic power spectra for models with stably-stratified inner regions. The parameters for models 1-8 are given in Table 2.6. The observational models for Earth, Uranus and Neptune are also shown for comparison. The legend in the top plot also applies to the bottom plot.



**Figure 2.24:** Average eccentric dipole tilts (left) and offsets (right) for models with stably-stratified fluid inner cores. The parameters for the models are given in Table 2.6. The absolute value of the dipole tilt is plotted on the left rather than the actual dipole tilt since we are interested in how large the tilt is rather than its polarity. In the left plot, at  $r_s/r_o = 0.7$ , both models 6 and 7 have approximately the same average dipole tilt, hence the symbols plot on top of each other which is why only one is visible. The legend in the left plot also applies to the right plot.

dipole tilts and offsets of Uranus' and Neptune's fields at specific time steps, which suggests that our concerns over the models' averages not being able to match Neptune's large dipole offset may not be warranted. It also suggests that the differences between Uranus' and Neptune's observed fields may not be the result of different dynamo region geometries, but merely a result of the strong variability of these fields in time.

## 2.5.4 Magnetic Energy

Similar to the section on solid inner cores, we wish to examine the properties of the magnetic field inside the source region in an effort to understand why this convective-region geometry produces a new field morphology. We begin by examining the magnetic energy (defined in section 2.4.4) in the models. Figure 2.26 plots the average ratio of non-axisymmetric to total magnetic energy for the models in Table 2.6 for both the poloidal and toroidal field components. We see that model 8 is again, quite different from the other models with a very axisymmetric poloidal and toroidal field. The other models show varying degrees of non-axisymmetry, with non-axisymmetric to total energy ratios in the range 0.4 to 0.8 for the poloidal field and 0.05 to 0.5 for the toroidal field. Clearly the poloidal fields are much more non-axisymmetric than the toroidal fields in the models. There also appears to be a correlation with Rayleigh number when  $r_s$  is kept constant. At a specific  $r_s$ , models with larger Rayleigh numbers contain a higher degree of non-axisymmetry. This effect is seen in

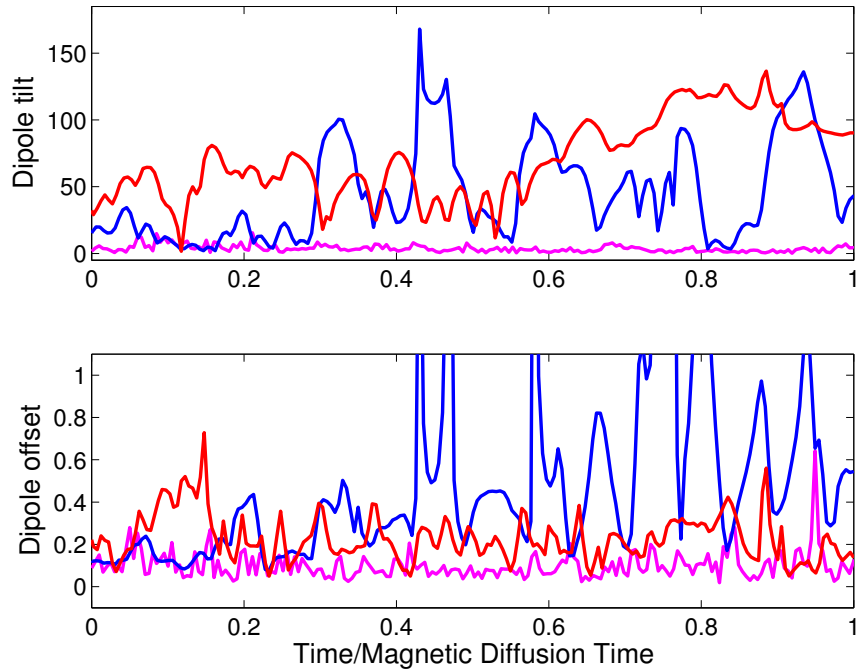


**Figure 2.25:** Average eccentric dipole models vs. time. Eccentric dipole tilts (top) and offsets (bottom) are shown for models 3 (blue), 7 (red) and 8 (magenta). Dipole offset is in units of planetary radii.

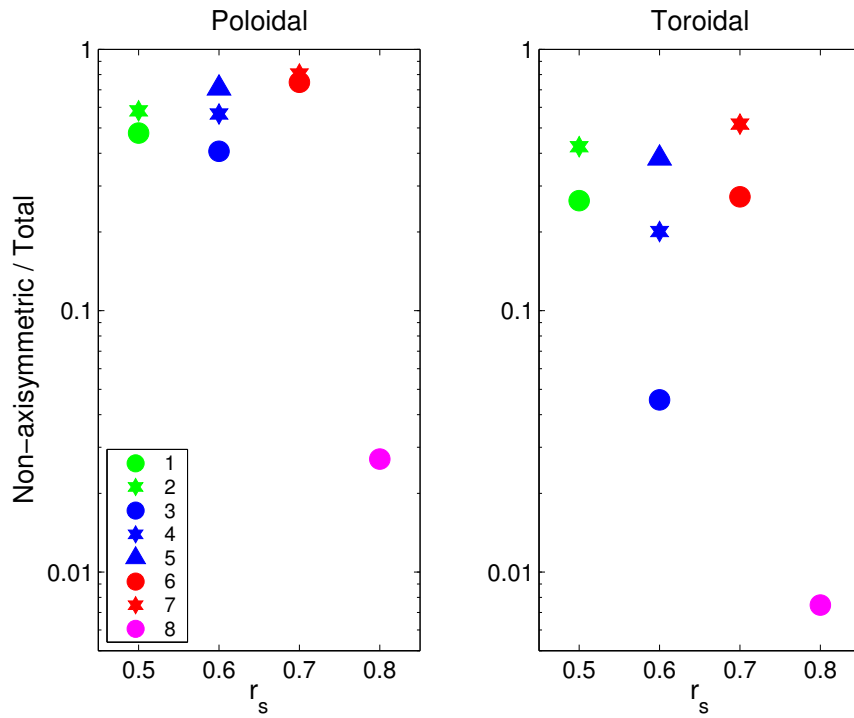


**Figure 2.26:** Average non-axisymmetric magnetic energy in poloidal (left) and toroidal (right) fields for the models with stably-stratified inner regions. The energy is plotted on a log scale and the parameters for the models are found in Table 2.6. The legend in the left plot also applies to the right plot.

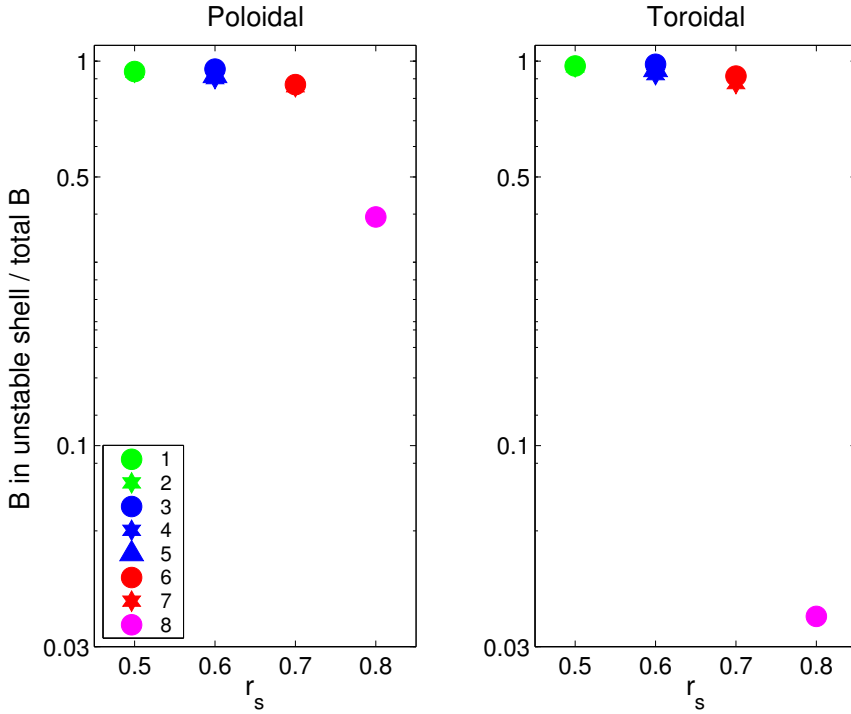


**Figure 2.27:** Average magnetic energy in unstable shell in poloidal (left) and toroidal (right) fields normalized to the total magnetic energy. The energy is plotted on a log scale and the parameters for the models are given in Table 2.6. The legend in the left plot also applies to the right plot.

both the poloidal and toroidal energy, but appears to affect the toroidal energy more significantly.

Although the inner region in these models is stable to convection, other fluid motions are not restricted in this region by the models and so it is possible to have some field generation/advection in the stable layer. It is also possible for magnetic field to diffuse into this region since it is electrically conducting. In Figure 2.27 we examine the ratio of energy in the unstable shell to energy in the stable shell for both the poloidal and toroidal components of the field. Model 8 is again quite different from the other models. Whereas most of the models have energy dominant in the unstable layer, suggesting that most of the field is generated here and resides here, model 8 appears to have nearly its entire toroidal field energy present in the stable layer and a significant portion of its poloidal energy as well.

To examine the time variability of the energy, Figures 2.28, 2.29 and 2.30 plot the magnetic energy in the stable and unstable layers of the toroidal and poloidal fields vs. time for models 3, 7 and 8 respectively. All three models exhibit strong time variability. Models 3 and 7, which both produce surface power spectra similar to those of Uranus and Neptune, have very different toroidal field components in the unstable shell. Model 3 has a toroidal field strongly dominated by its axisymmetric component whereas model 7 does not. It is interesting that both of these models produce similar symmetry in their poloidal fields. This again suggests that Rayleigh number and stable layer radius may be a strong influence on the toroidal field pattern produced.

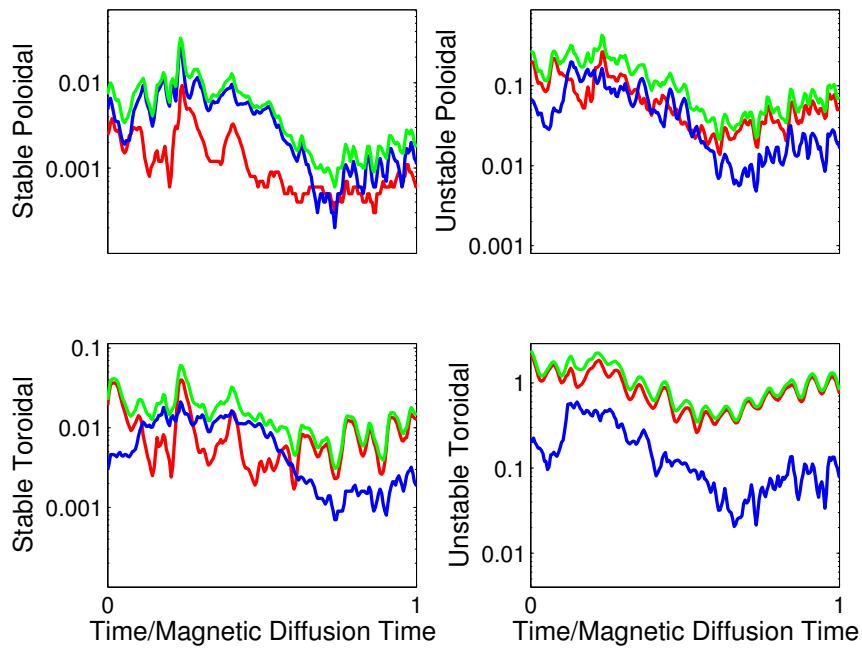


**Figure 2.28:** Magnetic energy vs. time for model 3. The axisymmetric (red), non-axisymmetric (blue) and total (green) energy are shown for the poloidal (top) and toroidal (bottom) components of the field in both the stable (left) and unstable (right) layers. Energy is non-dimensional and plotted on a log scale.

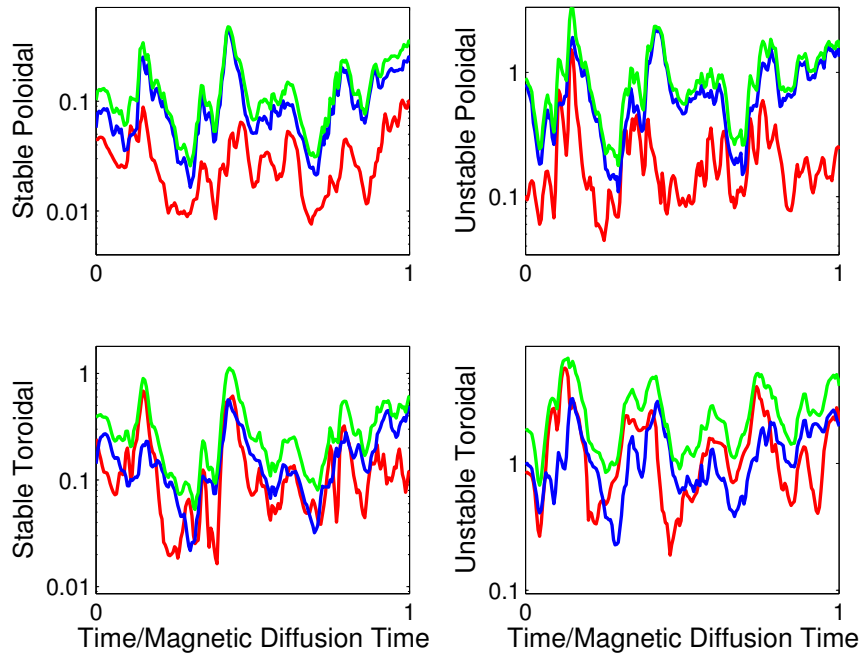


**Figure 2.29:** Same as Figure 2.27 except for model 7.

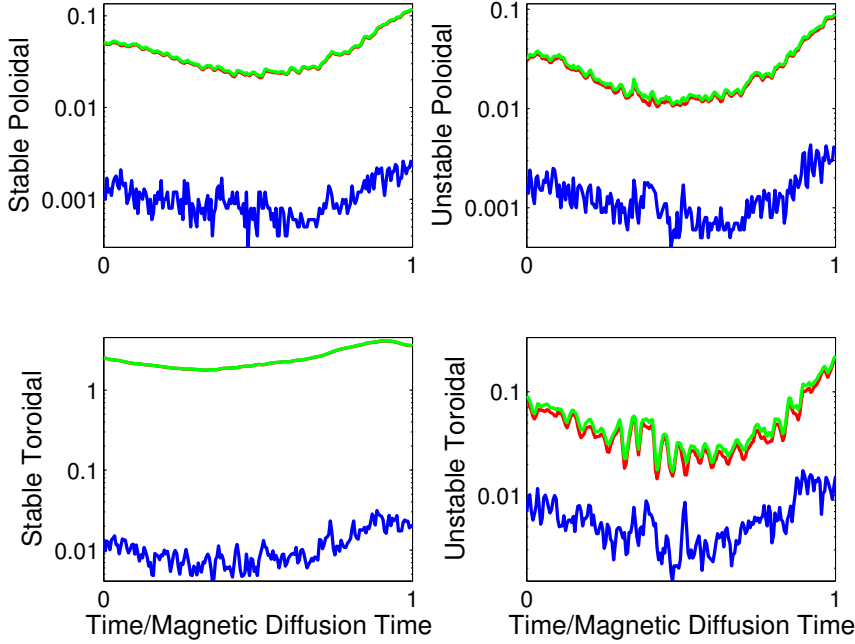


**Figure 2.30:** Same as Figure 2.27 except for model 8.

## 2.5.5 Kinetic Energy

Figure 2.31 plots the average kinetic energy (defined in section 2.4.5) for the models in Table 2.6. The models appear much more similar in their kinetic energies than any of the other characteristics examined so far. Their poloidal energies are all dominated by their non-axisymmetric components which is expected since convection produces a non-axisymmetric pattern, and the toroidal energies are dominated by their axisymmetric components. It is evident in these plots that model 8's different magnetic field structure is not a result of a different velocity field structure from the other models. The trend of stronger non-axisymmetry with higher Rayleigh number that was seen in both the toroidal and poloidal magnetic energies also holds for the toroidal kinetic energy. The poloidal kinetic energy, in contrast appears to have the opposite trend, with stronger non-axisymmetry seen at lower Rayleigh numbers, however the scale of the effect is much smaller here.

The time-variability of the kinetic energy is shown in Figures 2.32, 2.33 and 2.34 for models 3,7 and 8 respectively. In all three models, the non-axisymmetric (blue curve) component of the poloidal energy is barely visible because it lies under the total poloidal energy curve (green), and the axisymmetric (red curve) component in the toroidal energy is barely visible because it lies under the total toroidal energy curve (green). The most visible difference between the models is seen by comparing the axisymmetric toroidal energy for model 7 to the others. The amplitude of the toroidal energy appears to vary by an order of magnitude in this model, whereas the other models appear to have a very steady toroidal kinetic energy. In contrast to the toroidal energy, the poloidal energy in model 7 appears to vary much less in amplitude about the average, and has a similar pattern to the poloidal energy in models 3 and 8.

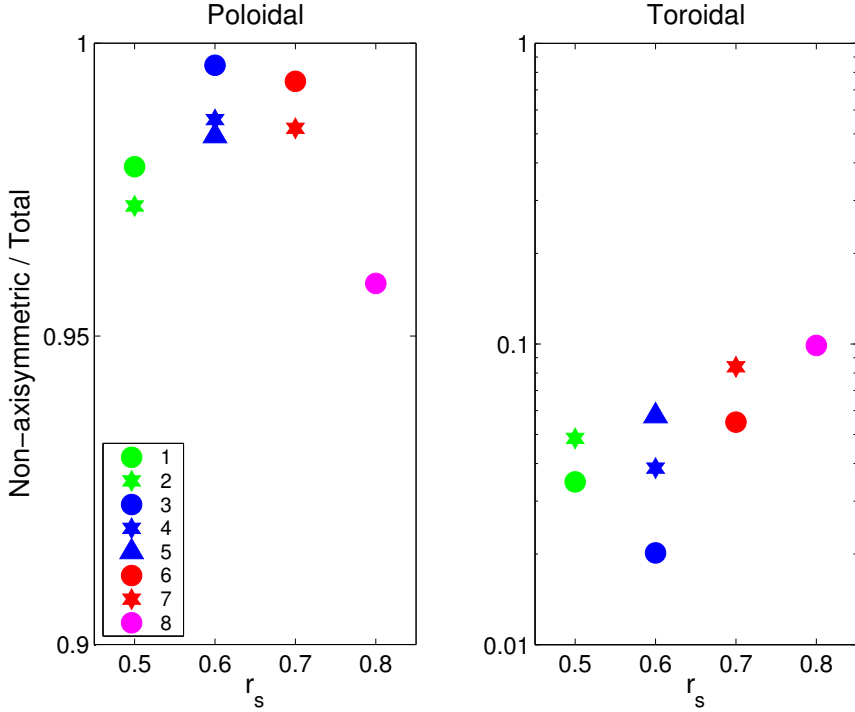


**Figure 2.31:** Average non-axisymmetric kinetic energy in the poloidal (left) and toroidal (right) fields for the models with stably-stratified inner regions. The energy is plotted on a log scale and the parameters for the models are found in Table 2.6. Note the difference in vertical axes limits for the poloidal and toroidal fields. The legend in the left plot also applies to the right plot.

## 2.5.6 Magnetic Field Plots

For a more visual representation of the fields, Figure 2.35 plots the radial magnetic fields at the top of the dynamo source regions for some of the models in Table 2.6. The axisymmetric-octupole dominated field of model 8 is well illustrated in this figure. The other models demonstrate similar levels of non-dipolar, non-axisymmetric field at the large scales as the fields of Uranus and Neptune. The models are very time dependent and so not too much emphasis should be placed on the similarity of specific features in these plots (showing the field at one instant in time) to Uranus' and Neptune's fields, however we will point out that model 7 appears quite similar to Neptune's radial field shown in Figure 1.2.

Figure 2.36 aids in the visualization of the axisymmetric magnetic field inside the dynamo source region for the same models and time steps as Figure 2.35. However, we should keep in mind that Figure 2.26 demonstrated that except for model 8, the fields have significant non-axisymmetric components, and therefore this figure may not give a good visualization of the total field. This figure gives a good visualization of model 8's toroidal field concentrated inside the stable shell and shows that the poloidal field in this model is strongest at the boundary between the two layers. For the other models, most of the toroidal and poloidal field are maintained in the unstable shell, although some field does penetrate the stable layer. It does not appear that the conductivity of the small inner core is important in any of the models since the magnetic field does not penetrate the stable layer significantly to that depth. The fields in models 1, 5 and 7 display various degrees of equatorial

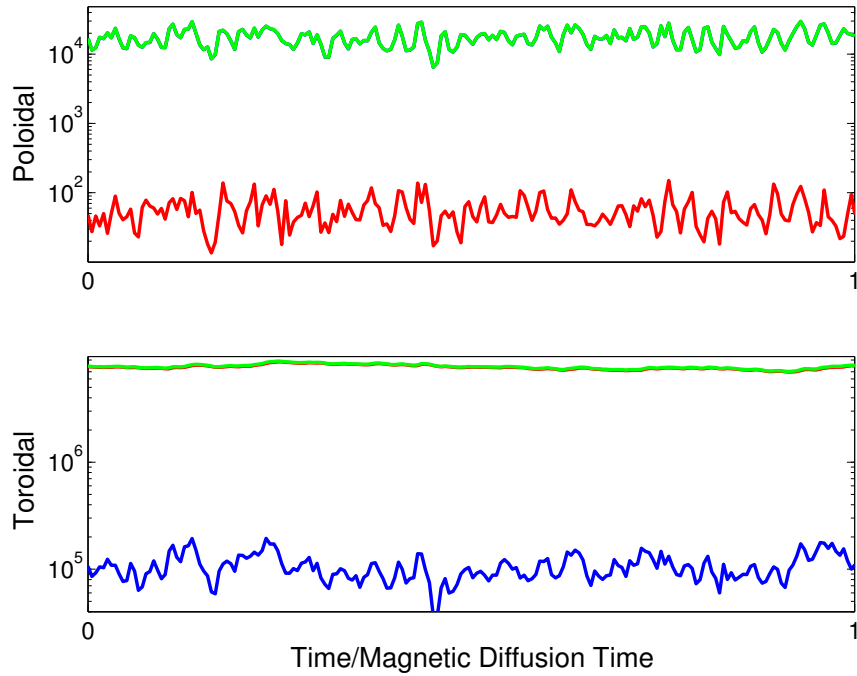


**Figure 2.32:** Kinetic energy vs. time for model 3. The axisymmetric (red), non-axisymmetric (blue) and total (green) energy are shown for the poloidal (top) and toroidal (bottom) components of the field. Energy is plotted on a log scale.

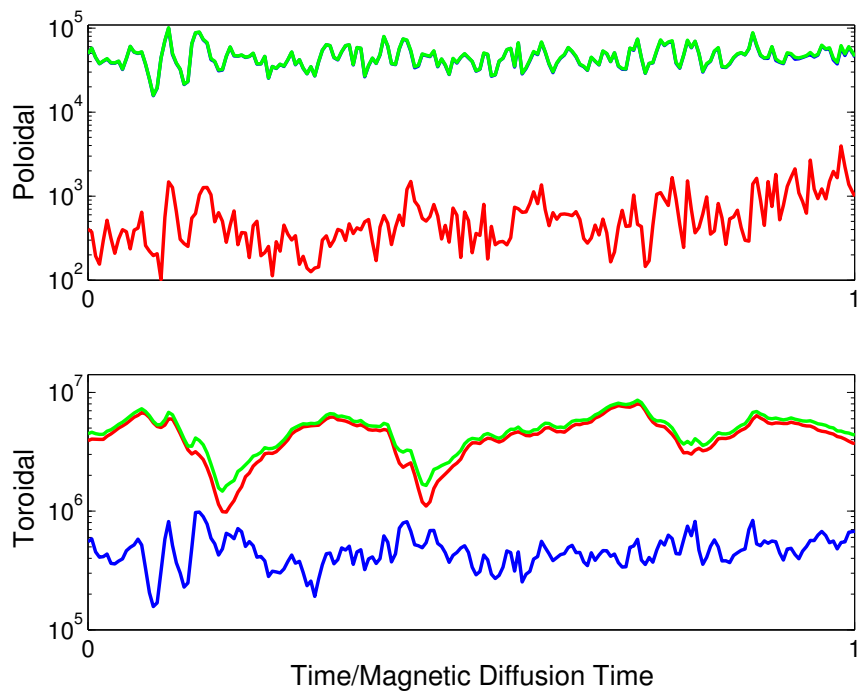


**Figure 2.33:** Same as Figure 2.32 but for model 7.

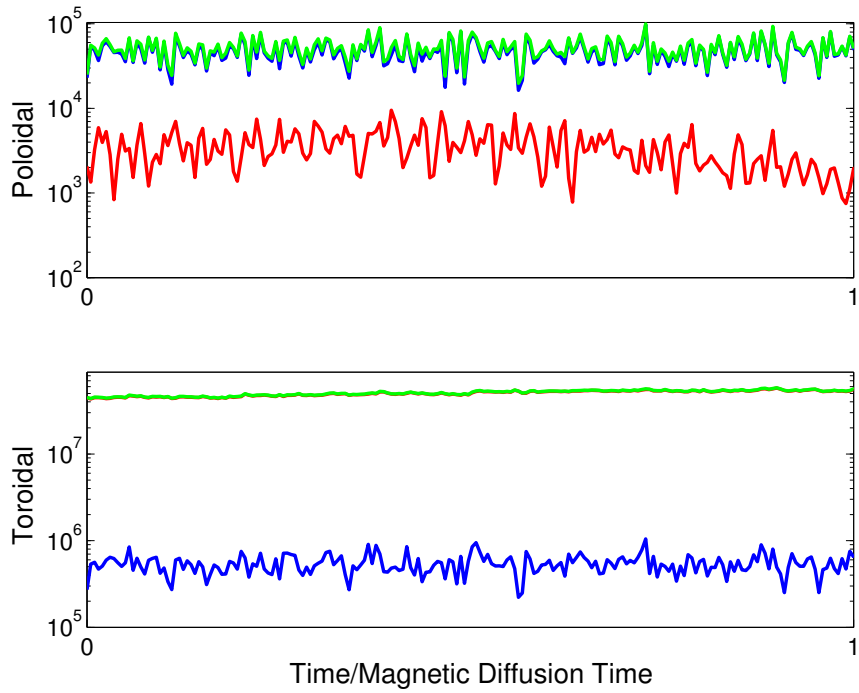


**Figure 2.34:** Same as Figure 2.32 but for model 8.

symmetry in their toroidal fields and equatorial anti-symmetry in their poloidal fields. This does not appear to be correlated strongly with stable shell radius and at various other time steps, model 5 produces a similar pattern to model 7 etc. The field morphologies are all quite variable except for that of model 8.

### 2.5.7 Velocity Field Plots

Figure 2.37 plots the velocity field for models 2 and 7. Model 7 which has a thinner convecting shell possesses a stronger differential rotation profile than model 2. This is consistent with our solid inner core models. A main difference between these models and solid inner core models is the presence of flow inside the stable layer. This flow is not part of the convection pattern seen in the outer layer and is most likely driven by magnetic field in the stable layer. The tilt in differential rotation profile seen in the solid inner core model 3 (see Figure 2.19) is not seen in either of these models. This is most likely because the thermal wind pattern seen in solid inner core model 3 is not present in these models (see Figure 2.38).

### 2.5.8 Magnetic Field Intensity

Another interesting property of Uranus' and Neptune's magnetic fields is their intensity, and we will now examine whether our numerical models can reproduce the observed intensity. Since the fields are non-dipolar, estimating the field intensity from their dipole moments is not very useful. Instead we choose to examine the magnitude of all the Gauss coefficients up to degree and order 3. Values for the observational models were given in Table 2.3. Since our numerical mod-

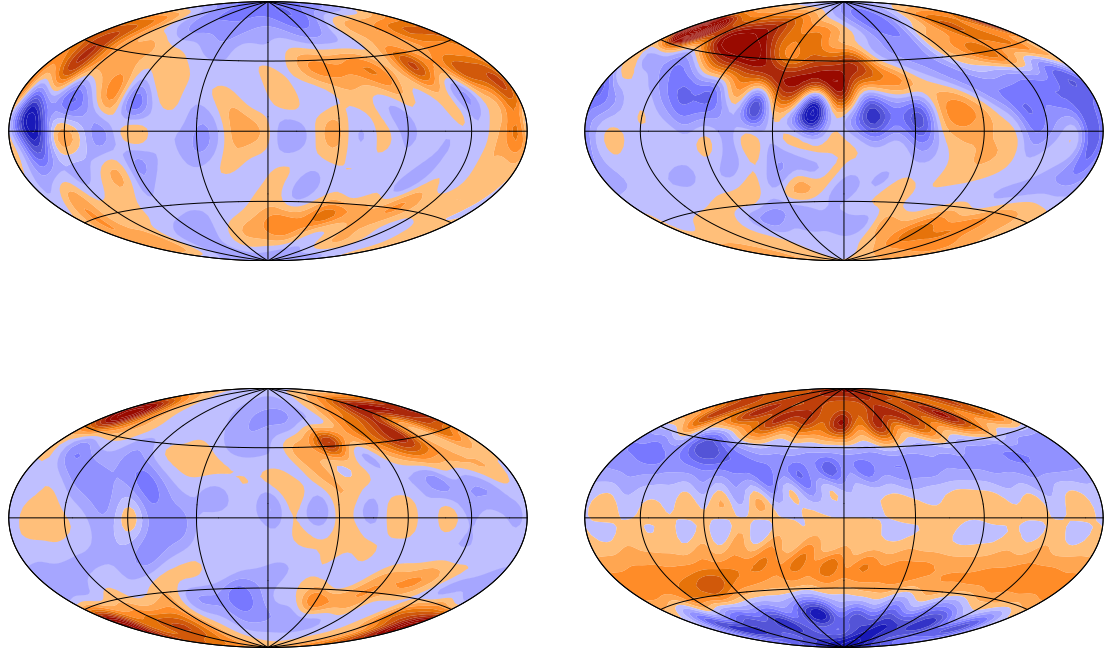


**Figure 2.35:** Filled contours of the radial magnetic field at the top of the dynamo source region at one instant in time for models 1 (top left), 5 (top right), 7 (bottom left) and 8 (bottom right). The different colors represent different field directions.

els are non-dimensionalized, we must dimensionalize our magnetic field variable in order to compare our models with the observations. The magnetic field variable was non-dimensionalized using the value obtained for an Elsasser number of 1, so to dimensionalize it, we multiply our variable by  $B_0 = \sqrt{2\Omega\rho/\sigma}$  and use representative values of  $\Omega = 1.0 \times 10^{-4} s^{-1}$ ,  $\rho = 10^3 \text{ kg m}^{-3}$ , and  $\sigma = 2 \times 10^3 (\Omega m)^{-1}$ . We can then examine the intensity of the Gauss coefficients in our models.

We find that most of our dynamo models produce fields where some of the Gauss coefficients are up to one order of magnitude larger than the observational values. However, one of our models, model 3, does produce similar Gauss coefficient magnitudes as the observations, although still slightly larger. The first 15 Gauss coefficients for one instant in time of this model are given in Table 2.7 and can be compared to the observational values given in Table 2.3.

Geodynamo models have various degrees of success at reproducing observational Earth-field intensities. For example, the Kuang and Bloxham (1997) model does quite well whereas the Glatzmaier and Roberts (1995a) model generates a field with intensity about 30 % of the Earth's field. Notice that our numerical model that produced the closest results worked at the lowest Rayleigh

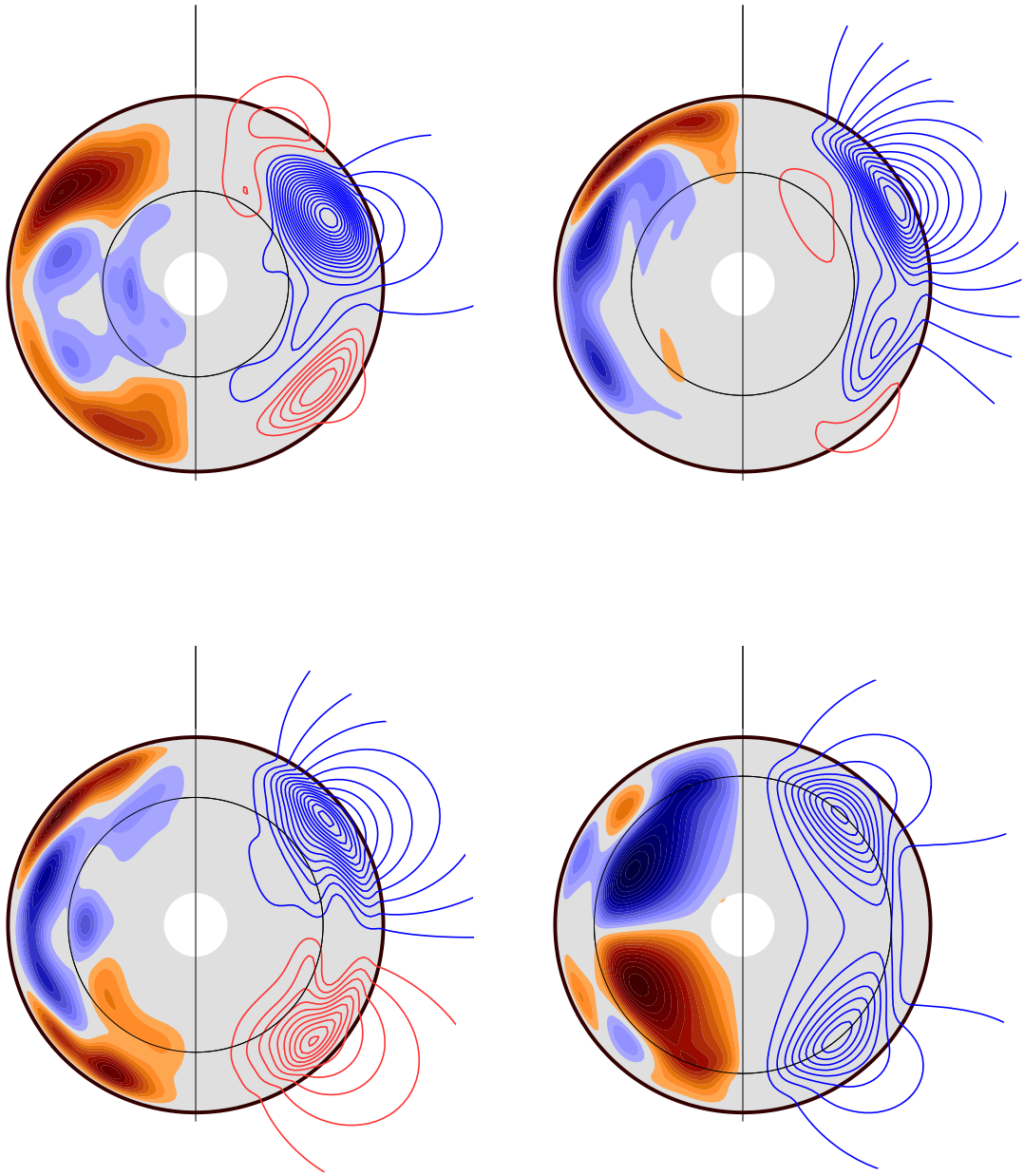


**Figure 2.36:** Axisymmetric magnetic field in a meridional slice through the dynamo source region at one instant in time for models 1 (top left), 5 (top right), 7 (bottom left) and 8 (bottom right). Contours of the toroidal field are shown in the left half and streamlines of the poloidal field are shown in the right half of the plots. The different colors represent different field directions. The grey shell is the fluid core, the inner white region is the solid inner core, the thick black circle is the top of the dynamo source region, the thin black circle is the boundary between the stable and unstable shells and the black vertical line represents the rotation axis.

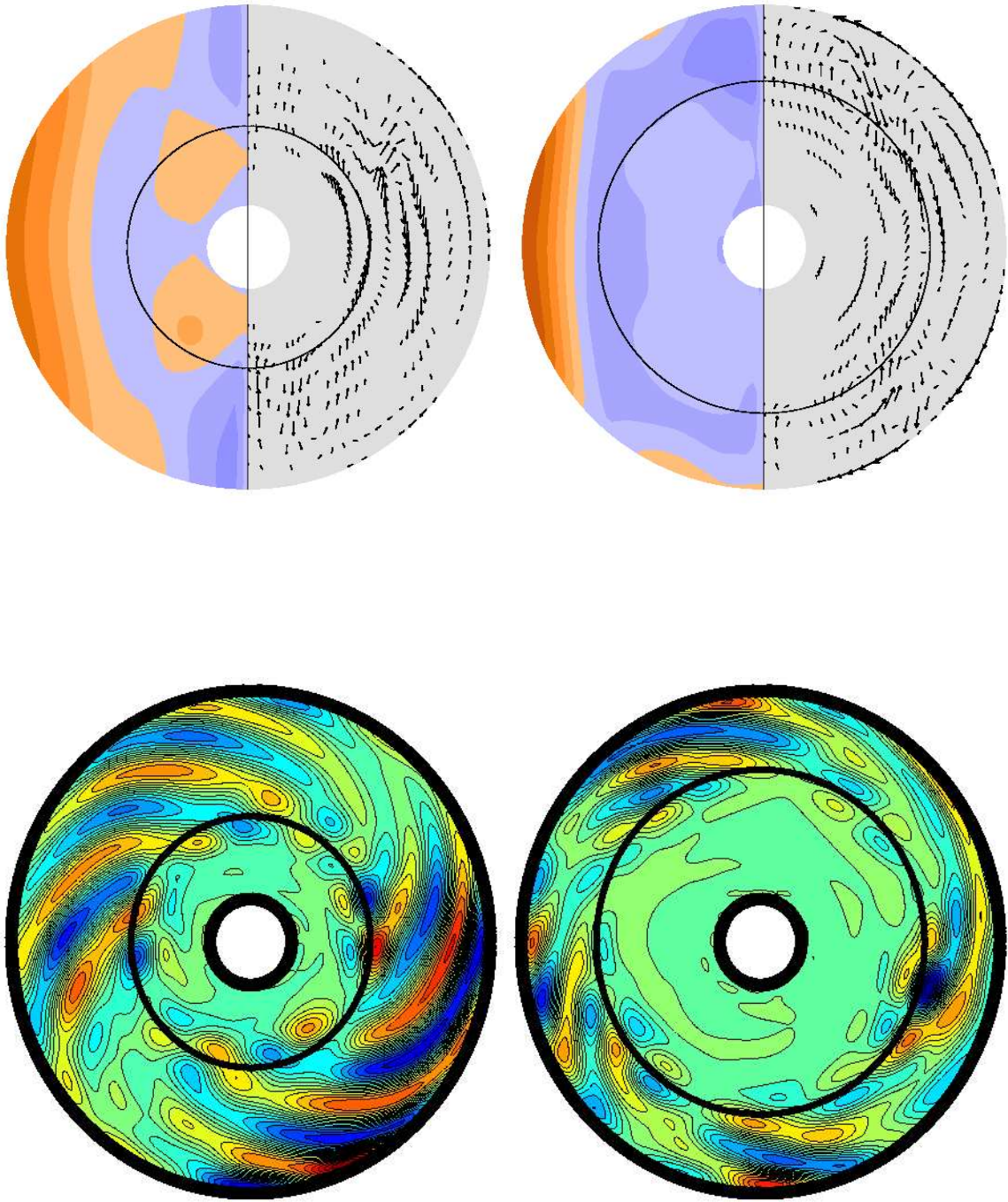


**Figure 2.37:** Velocity field for models 2 (left) and 7(right). The Axisymmetric field in a meridional slice through the dynamo source region at one instant in time is plotted in the top row. Contours of the axisymmetric toroidal field are plotted in the left half and flow vectors of the axisymmetric poloidal field are plotted in the right half. The non-axisymmetric poloidal field in a slice through the equator is shown in the bottom row. The contours are of the curl of the horizontal velocity field and the boundary between the stable and unstable layers is shown as a black circle.

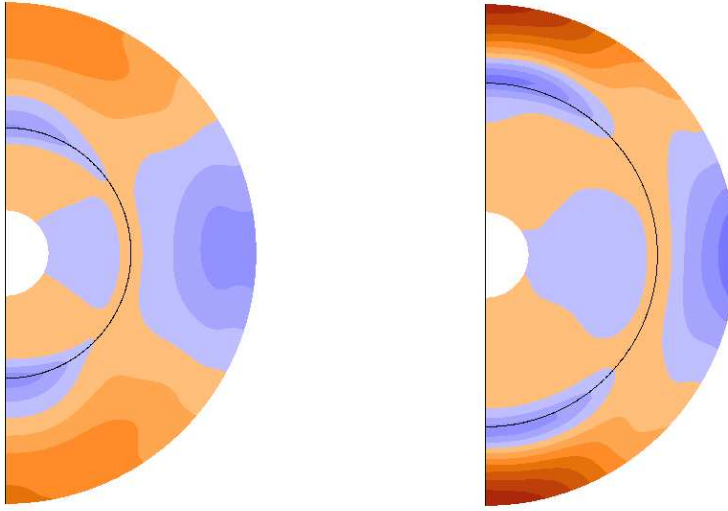


**Figure 2.38:** Axisymmetric temperature perturbation field in a meridional slice through the dynamo source region at one instant in time for models 2 (left), and 7 (right).

number of the models we studied. It is possible that if we work at even lower Rayleigh numbers we might be able to reproduce the field intensity better. Another possibility is that some of the approximations made in our numerical models resulted in the larger field intensity. These possibilities will be examined in future work.

### 2.5.9 Summary of Stably-Stratified Inner Region Models

We have found that dynamos operating in fluid convecting shells surrounding stably-stratified fluid interiors can produce magnetic fields similar to those of Uranus and Neptune. The models produce non-dipolar, non-axisymmetric magnetic fields that are highly variable in their morphology with time. For the cases studied we find that the stronger the convection in the models, the more non-axisymmetric the fields. The model which most resembles Uranus' and Neptune's fields in both morphology and intensity is model 3 from Table 2.6, although this may be coincidental since all the fields are highly variable in time.

Taking into account the Earth's field and model 8 from Table 2.6 it appears that there may be a minimum and maximum stable-layer radius at which Uranus- and Neptune- like solutions result. The minimum would result from eventually having a convecting shell thick enough that a stable-dipolar dynamo will result, similar to that seen in Earth, Jupiter and Saturn. The maximum, according to our models, occurs in the range  $0.7 < r_s \leq 0.8$ . When the convecting shell becomes too thin, most of the magnetic field penetrates the stable layer below and maintains a strong toroidal field there. The poloidal field in this case is generated near the boundary between the stable and unstable layers since this is the optimum place for both convective motions and the presence of a toroidal field from which the poloidal field is generated.

Most numerical dynamo models produce axially dipolar dominated fields, although a handful of non-axial, non-dipolar dynamos have been found (Grote *et al.*, 2000b; Grote and Busse, 2000; Kutzner and Christensen, 2002; Ishihara and Kida, 2002b). These studies find these dynamos

**Table 2.7:** Gauss coefficients (in nanoTeslas) for model 3 at one instant in time.

$g_1^0$	-2076
$g_1^1$	-30324
$h_1^1$	11622
$g_2^0$	25280
$g_2^1$	-1917
$g_2^2$	5306
$h_2^1$	4433
$h_2^2$	4312
$g_3^0$	-27639
$g_3^1$	-9543
$g_3^2$	10878
$g_3^3$	10319
$h_3^1$	-5385
$h_3^2$	3445
$h_3^3$	9485

in small regions of parameter space and some produce more ‘simple’ non-Earth-like fields than Uranus’ and Neptune’s fields such as equatorially dipolar dominated fields and axially quadrupole dominated fields. Since all numerical models at present cannot operate in the appropriate parameter space for planetary cores, we seek solutions that prevail over a wide range of parameter values. Because a range of stable layer radii and Rayleigh numbers can produce Uranus- and Neptune- like fields in our numerical models, we argue that this is a more likely and more robust explanation for Uranus’ and Neptune’s fields. It is also the only explanation that is consistent with the heat flow observations from these planets.

## 2.6 Discussion

Comparing the surface magnetic power spectra in Figures 2.23 (stable fluid inner cores) and 2.6 (solid inner cores), we see that the only solid inner core models with similar spectra to our stable inner core models are the less-conducting inner core models 3 and 4. These figures clearly demonstrate that changing only the size of the inner core does not affect the axial-dipole dominance of the fields, however changing the state of the inner core (fluid instead of solid) can significantly affect the morphology of the magnetic fields. The fact that the models with stably-stratified inner cores produce similar field morphologies to models with more insulating inner cores may suggest why the stably-stratified cores can produce this new field morphology.

The stabilizing effect of a solid conducting core was discussed in section 1.3.4. The solid inner core can effectively anchor the axially-dipolar field, stabilizing it to rapid fluctuations in the fluid outer core. In our models with insulating solid inner cores, the inner core has lost this anchoring effect, thereby giving the fields freedom to change on the rapid convective timescales present. This lack of anchoring also results in less communication between different regions of the core. This can

be seen in Figure 2.18 where even with the thinnest of shells (model 7), a magnetic field line can join remote regions inside the northern and southern tangent cylinders. Even though these regions do not come into direct contact, they maintain the same field which joins them through the solid conducting core. In contrast, model 3 in this figure shows there is little communication between the hemispheres once the inner core loses its conductivity.

A stable fluid interior can mimic this lack of anchoring seen in insulating inner core models. Because this region is fluid, it can respond to electromagnetic stress through fluid motion, unlike a solid conducting core. The magnetic field is no longer stabilized by the interior since the magnetic field can move here on a timescale much shorter than the diffusion timescale of a solid conducting core. This reduction in stability, combined with the smaller length scales of the thinner shells promote the creation of higher degree, non-axisymmetric structure in our numerical models.

We have found that there is a minimum convective shell thickness for which models with stably-stratified inner cores will mimic models with solid insulating inner cores since model 8 of Table 2.6 demonstrates that dynamos with a stable layer radius of  $r_s = 0.8$  have magnetic fields that concentrate inside the stable region. This cannot happen in a model with an insulating solid inner core. The next goal will be to determine the maximum convective shell thickness for which Uranus- and Neptune- like magnetic field morphologies result. We have not studied stably-stratified interior models at smaller  $r_s$  values (*i.e.* thicker shells) due to a limited amount of time available. Models with smaller  $r_s$  will be run in the future, as well as models with smaller  $r_{io}$  and insulating inner cores. The answer to any questions regarding why we didn't look at certain parameter value choices in our models (as long as they are feasible in dynamo modeling) is that we have not yet had the time. Clearly a more thorough examination of parameter space is necessary to better understand these magnetic field morphologies.

## 2.7 Stable Stratification in Other Dynamos

We have demonstrated the importance stably-stratified layers may have for Uranus and Neptune and now ask whether they may be important in other planetary dynamos as well. Below we discuss some possible applications for Earth, Saturn and the Sun.

### 2.7.1 Earth

It has been suggested that the outer portion of the Earth's core may be stably-stratified as either a result of a build up of light material that has been released through core freezing (Fearn and Loper, 1981) or as a result of slow core cooling by the mantle (Gubbins *et al.*, 1982). However, other theoretical considerations of the effects this stratification would have on the generation of the geomagnetic secular variation suggest that strong stable stratification may not be possible (Bloxham, 1990). Jones *et al.* (1995) examined the effect of a stable layer surrounding an unstable layer using a numerical mean-field dynamo model. They imposed the stable layer in the outer half of the core and found that the solutions had weaker non-axisymmetric fields than their solutions without a stable layer. Their models with a stable layer fit the observed geomagnetic field better than their models without a stable layer, arguing for the presence of this stable layer in the core. However, many other numerical dynamo models, especially fully 3-D models (*e.g.* Kuang and Bloxham (1999)) are able to fit geomagnetic observations without the presence of an outer stable layer.

## 2.7.2 Saturn

Another planet for which stable stratification may be important is Saturn. The observations of Saturn's magnetic field have demonstrated that Saturn's non-axisymmetric Gauss coefficients are exactly 0 (within errors) meaning that the field at satellite altitude is perfectly axisymmetric. Although Earth's and Jupiter's magnetic fields are dominated by their axisymmetric components, they do not possess the total symmetry seen in Saturn's field. Cowling's theorem (Cowling, 1934) states that a purely axisymmetric magnetic field cannot be maintained by dynamo action which seems problematic if we wish to explain Saturn's field by dynamo generation. However, the observed field is merely an extension of the field generated in the convecting region of the planet and as long as this internal field has some non-axisymmetry, it can be dynamo generated. Stevenson (1983) suggested a mechanism by which the non-axisymmetric field in the convective region can result in an observed field that is axisymmetric. Saturn may contain a stably-stratified helium rain-out layer surrounding the convecting shell (Salpeter, 1973; Stevenson, 1977) and this electrically conducting shell may axisymmetrize the field through the shearing motion of differential rotation. The work by Jones *et al.* (1995) suggests that this can lead to more axisymmetrized fields, however it has not been demonstrated that a purely axisymmetric field can result. This geometry has also been studied using kinematic dynamo theory (Love, 2000), and it was found that a stable layer could axisymmetrize the field, but that this was not always the outcome. Clearly more work needs to be done, including fully 3-D modeling, to determine whether Saturn's axisymmetry can be explained via a stable layer.

## 2.7.3 Sun

Our Sun, along with many other stars, possess magnetic fields generated by dynamo action. The Sun's magnetic field is comprised of a strong dipole component ( $\sim 10^{-4}$  T at photosphere) combined with even stronger complex small scale fields which can be as intense as  $\sim 10^{-2}$  T. The solar dynamo operates in a thin convecting shell surrounding its radiating interior. With the help of helioseismology we can observe the rotation profile in this region (for a nice review see Thompson *et al.* (2003)), thereby aiding in our understanding of the solar dynamo process. The transition layer between the convection zone and the radiating interior (known as the tachocline) may be an important stably-stratified layer. It is already believed to be important in the storage of magnetic flux bundles which eventually rise through the convection layer to become sunspots (one component of the strong small scale fields). In addition to the small scale structure, it is important to understand where the large scale dipole component of the field comes from. Our model 8 from section 2.5 may be relevant since it demonstrates that a dipole field can be maintained in a stably stratified inner region. Perhaps a similar process is occurring in the Sun in a stably-stratified region interior to the convective shell. This will be examined in future work.

# Chapter 3

## Mercury

### 3.1 Introduction

One could argue that of all the planets, Mercury inhabits the most hostile region of our solar system. Being closest to the Sun, it is exposed to the hottest external temperatures, largest solar gravitational forces, and the most violent solar wind activity. In this extreme environment we have a planet with surprising physical characteristics that need to be explained in our quest to understand planetary evolution. Mercury's anomalous nature can be seen in a comparison of various physical parameters of the terrestrial planets, such as those listed in Table 3.1.

Mercury's small radius of 2440 km makes it the smallest planet in the solar system (aside from Pluto if you believe it should be classified as a planet) and falls between the radii of Jupiter's two moons Callisto (2408km) and Ganymede (2634 km). Its uncompressed density of about  $5300 \text{ kg/m}^3$  implies the planet has a very large iron component. If it is fully differentiated into a mantle and core, then Mercury's core radius is approximately 75% of the total planet radius and its core mass is about 60% of the total planet mass; the largest core radius and mass fractions in the solar system. Whatever process was responsible for Mercury attaining this high metallic mass fraction, it must have occurred very early in its history since the planet's dense crater coverage implies the surface retains features of the heavy bombardment 3.8 billion years ago.

Mercury's orbit and rotation are also peculiar. The planet is trapped in a 3:2 spin-orbit reso-

---

**Table 3.1:** Physical properties of the terrestrial planets. Data from Lewis (1995).

Property	Mercury	Venus	Earth	Mars
Equatorial radius (km)	2439	6051	6378	3396
Planet mass ( $\times 10^{23}$ kg)	3.3	48.7	59.7	6.42
Uncompressed density ( $\text{kg/m}^3$ )	5300	4000	4050	3740
Surface gravity ( $\text{m/s}^2$ )	3.7	8.9	9.8	3.7
Rotation period (Earth days)	58.65	-243.01	1	1.03
Orbital period (Earth days)	87.97	224.70	365.26	687.01
Solar distance (AU)	0.39	0.72	1	1.52
Obliquity of spin axis (degrees)	0.0	177.3	23.45	25.19

**Table 3.2:** Mariner 10 trajectory and magnetic field characteristics. Data from Connerney and Ness (1988).

	Mercury I	Mercury III
Interplanetary field (nT)	~ 18	~ 20
Closest approach altitude (radii)	0.29	0.13
Time in magnetosphere (minutes)	33	14
Maximum field strength (nT)	98	400

nance; unusual in that most other bodies that are trapped in resonances are in the 'energetically easier' 1:1 resonance. Until recently it was believed that capture into the 3:2 resonance was highly improbable but recent work by Correia and Lasker (2004) demonstrated that if the chaotic evolution of Mercury's orbit is taken into account, then the resulting higher orbital eccentricities lead to the 3:2 resonance as the most probable final outcome of the planet's evolution. Another unusual aspect of its orbit is that, due to its long rotation period and non-zero eccentricity, when Mercury is close to perihelion the Sun moves in the retrograde direction. This means that during certain days on Mercury, the Sun rises, stops rising, changes direction and begins to unrise, then stops unrising, changes direction and rises again.

## 3.2 Observations of Mercury's Magnetic Field

Perhaps the most intriguing find for Mercury (although I cannot rule out bias on my part), was the presence of a magnetic field. Mariner 10's observations during the first and third flybys of the planet in 1974–1975, revealed the presence of a magnetic field of internal origin (Ness *et al.*, 1975, 1976). This was the first mission to use dual triaxial fluxgate magnetometers (Ness *et al.*, 1971) which allowed the removal of spacecraft magnetic fields from the data. Some characteristics of the two flybys and the field observed are listed in Table 3.2 and the trajectory of the two flybys is plotted in Figure 3.1. The inferred magnetic dipole moment is approximately  $300 \text{ nT} - R_M^3$  ( $1R_M = 2440 \text{ km}$ ), but the value varies among authors. Connerney and Ness (1988) showed that this variability (a factor of 2), is largely a result of different model assumptions regarding the interplanetary field and different modeling techniques. In essence, the value is not well constrained because of the spatial distribution and limited quantity of the data.

Even with the uncertainty in the dipole moment, the inferred field strength appears problematic for all typical sources of planetary magnetic fields. It is much too large to be explained by induction effects from solar wind currents on the premise that an induced field should not be larger than the inducing field. Impact magnetization is an unlikely candidate since a global dipolar field would not be the expected resulting morphology. One possibility is that the dipole field is due to crustal remanent magnetization from a dynamo operating in Mercury's past. If this is the case, then Mercury's crustal magnetism is quite different from that of Earth and Mars where crustal magnetic fields are short wavelength (*i.e.* non-dipolar) features. A uniform spherical shell magnetized by an internal field cannot be the source of the dipole signature because of Runcorn's theorem (Runcorn, 1975), however a planet is capable of producing a dipole remanent field if inhomogeneities exist in the magnetized shell. Stephenson (1975) and Srnka (1976) suggested variations in magnetic permeability between the shell and free space or the interior as a possible inhomogeneity, and more recently, Aharonson *et al.* (2004) showed that variations in crustal thickness due to laterally varying

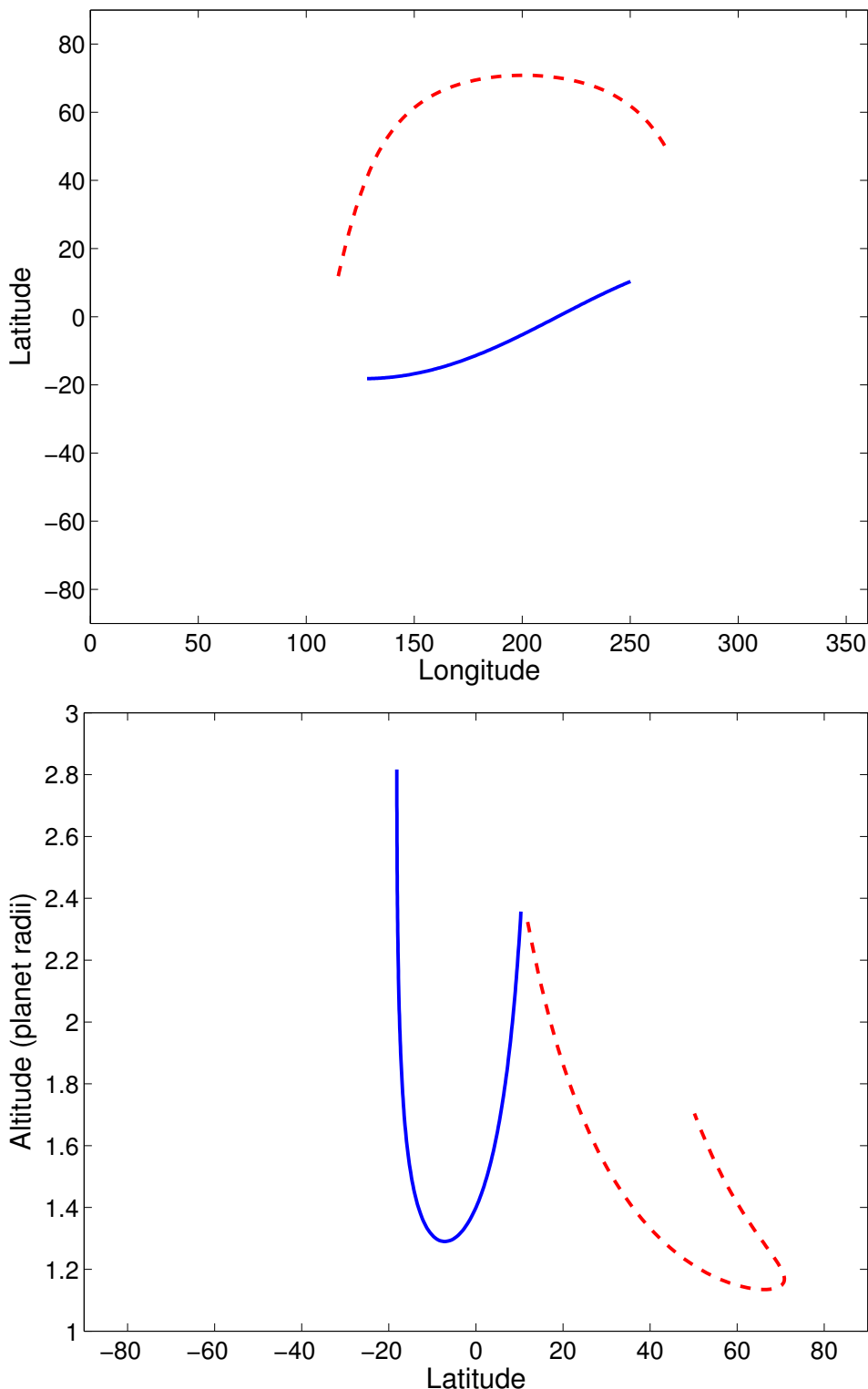


**Figure 3.1:** Mariner 10 trajectory shown as latitude vs longitude coverage (top), and altitude vs. latitude coverage (bottom). The blue solid lines are the trajectory of the first flyby and the red dashed lines are the trajectory of the third flyby. Data from Lepping *et al.* (1979).

external temperature gradients at Mercury could be a source of inhomogeneity. In both cases, a dipolar field can be produced from the crustal magnetism, but it is difficult to reconcile the field's strength. In order to explain the field's intensity, Mercury's crust must contain minerals capable of sustaining high specific magnetizations (similar to the magnetizations needed to explain Mars' crustal field), or Mercury's past dynamo produced a field much more intense than Earth's (which is unlikely). Reversals must also be at a minimum since they diminish the resultant field strength. Although it appears difficult to explain Mercury's field via crustal remanence, this possibility cannot be ruled out.

The possibility we will consider in the rest of this chapter is whether the field could be due to an active dynamo. Before the field's discovery, this wasn't considered likely since Mercury's small size suggested the planet should have cooled efficiently and hence completely frozen its iron core, negating the possibility of current dynamo action. However, the recent discovery by the Galileo mission that Ganymede, a body of similar size to Mercury, possesses an active dynamo suggests that it may not be so unusual for a Mercury-size body to possess a dynamo. Recent Earth-based radar measurements of Mercury's librations in longitude (Margot *et al.*, 2004) have demonstrated that the core and mantle are decoupled, and hence that the core must be at least partially fluid. This provides the basic necessary (although by no means sufficient) condition for an active dynamo to be the source of the magnetic observations. What is unknown is whether this fluid shell contains the necessary complex 3-D motions required to maintain magnetic field generation against ohmic decay.

The reason an active dynamo source for Mercury's field has been viewed as problematic is because of discrepancies between the observed field's magnitude and theoretical estimates on the magnetic field strength produced by an Earth-like dynamo. Whereas the remanent field explanation suffered from the observed field being too large, an Earth-like dynamo solution indicates the observed field is too small. This has led to suggestions of exotic dynamo alternatives such as a thermoelectric dynamo (Stevenson, 1987; Giampieri and Balogh, 2002) to explain Mercury's field.

### 3.3 Mercury's Thermal History and the State of its Core

Understanding how the core can remain liquid and cool efficiently enough to drive a dynamo is crucial in understanding the planet's interior composition, structure and thermal history. Thermal evolution models show that it is difficult to keep a pure iron core from freezing totally (Siegfried and Solomon, 1974), and so one possibility explored in these models is whether the core can remain at least partially molten if it contains a small concentration of a light element such as sulfur (Stevenson *et al.*, 1983). The presence of sulfur depresses the freezing point in the core, and while a nearly pure solid iron inner core grows through planet cooling, the sulfur concentration increases in the fluid outer core, further depressing the freezing point and thereby keeping the outer layer liquid. In the models studied, plausible sulfur concentrations of 1- 5% resulted in thin liquid outer cores surrounding relatively larger inner cores. The inner to outer core radius ratios were in the range 0.74-0.96. These values are much larger than Earth's radius ratio of 0.35.

Another possibility for keeping the core molten is the presence of an additional heat source such as tidal heating of the inner core. Schubert *et al.* (1988) showed that significant heating is generated only when the inner core becomes relatively large, however this additional heat source does not significantly alter the growth rate of the inner core or the temperatures inside the planet compared to previous models which only incorporated sulfur concentrations. The main effect of the tidal heating

is to slightly increase the temperature of the inner core and possibly allow thermal convection to be maintained for an additional 225 Myr compared to models without tidal heating.

Conzelmann and Spohn (1999) study a thermal evolution model that incorporates pressure and temperature dependent rheology in the description of mantle convection. Their models confirm the findings of the previous models mentioned above, but show that smaller sulfur concentrations are needed to produce the solid inner core radii seen in the previous models. They find that sulfur concentrations as low as 0.1 % are capable of maintaining a liquid outer layer in the core. Hauck *et al.* (2004) also incorporate temperature and pressure dependent rheology in their thermal evolution models, and further incorporate the magmatic and tectonic evolution of Mercury. Their models also show that outer liquid layers are easily produced for a wide range of parameter values.

So it appears that theoretical modeling and Earth-based radar observations are in agreement that Mercury contains at least a partially molten core. Although the radar measurements cannot determine the size of the solid inner core, the thermal evolution models show that a wide range of inner core radii are possible. The earlier models favored a relatively large solid inner core, and although the more recent models have relaxed this constraint somewhat, they still allow for large solid inner cores.

### 3.4 Magnetic Field Strength Expected From a Dynamo

In the introduction we mentioned that Mercury's magnetic field, if generated by a dynamo, produces a field too weak to be consistent with an Earth-like dynamo. In this section we will demonstrate two methods for estimating the magnetic field strength of a dynamo and compare the estimates to the observed field strengths of Mercury and Earth.

The first method (energy balance) involves balancing the energy supplied to the dynamo and the dissipation resulting from magnetic field generation. Following Stevenson (1983), the second law of thermodynamics states:

$$\Phi_{diss} < 4\pi R_c^2 F_c \left( \frac{T_m}{T_u} - 1 \right) + Q_{grav} + W, \quad (3.1)$$

where  $\Phi_{diss}$  is the total dissipation in the core,  $R_c$  is the radius of the core,  $F_c$  is the core heat flux,  $T_m$  and  $T_u$  are the maximum and upper boundary temperatures in the core,  $Q_{grav}$  is the gravitational energy release from the solidification of the core, and  $W$  is the rate at which work is done on the core by external processes such as tides . Using the Boussinesq approximation yields the approximation:

$$\Phi_{diss} \simeq \frac{\Delta T}{T_m} F_{conv} + Q_{grav} + W, \quad (3.2)$$

where  $\Delta T = T_m - T_u$  and  $F_{conv}$  is the radially averaged convective heat flux. Assuming  $Q_{grav}$  dominates the thermal and external energy sources, and assuming  $\Phi_{diss}$  is dominated by ohmic dissipation (since the magnetic diffusivity is much larger than the other diffusivities in the problem), one obtains the balance

$$Q_{grav} \simeq \int_{V_c} \frac{J^2}{\sigma} dV, \quad (3.3)$$

where  $V_c$  is the volume of the core. Assuming the poloidal currents (toroidal fields) are dominant in the core, and that most of the dissipation is in the outer core where the field is generated, we can

obtain an estimate for the right hand side of equation 3.3:

$$\int_{V_c} \frac{J^2}{\sigma} dV \sim \frac{4\pi R_{ic}^2 dB_T}{\sigma \mu_0^2 L^2} \quad (3.4)$$

where  $R_{ic}$  is the radius of the solid inner core,  $d$  is the thickness of the fluid outer core,  $B_T$  is the characteristic toroidal field strength and  $L$  is the characteristic length scale of the poloidal currents. The poloidal currents will certainly be smaller than  $d$ , and if we assume the dissipation occurs in the large scale currents, we can set  $L = \beta d$  where  $\beta$  is a scale factor say between 0.1 and 1.

Using the thermal evolution models for Mercury to estimate the gravitation energy, the inner core radius and the fluid outer shell thickness, and using  $\sigma = 5 \times 10^5$ , Stevenson (1987) and Schubert *et al.* (1988) showed that magnetic field strengths on the order of  $10^5 - 10^7$  nT are obtained from equation 3.3. This method for estimating the field, clearly depends on several assumptions which may be false for Mercury, especially that the energy is dominated by large scale currents, and if Mercury has a large inner core, that the dissipation is mostly in the outer core. Another issue is that there is no reliable observational estimate for  $Q_{grav}$  so it can only be estimated from thermal evolution models, and is therefore highly dependent on the individual model assumptions. However, it is a place to start and we will compare this estimate with another estimate we will obtain next from an entirely different method.

The second method (magnetostrophic balance) relies on assuming that Mercury's dynamo operates in the strong-field regime where the Lorentz force balances the Coriolis force. By comparing the size of the Lorentz force and Coriolis force terms in the momentum equation we get:

$$|2\Omega \times \mathbf{v}| = |\rho^{-1} \mathbf{J} \times \mathbf{B}| \quad \Rightarrow \quad (3.5)$$

$$2\Omega U = \frac{B^2}{\mu_0 \rho L}, \quad (3.6)$$

where  $U$  is a characteristic velocity scale,  $B$  is a characteristic magnetic field scale, and  $L$  is a characteristic length scale of electrical currents. Solving equation 3.6 for the magnetic field strength, and using the definition of the magnetic Reynolds number ( $Re_M = \sigma \mu_0 U L$ ) we obtain an estimate for the magnetic field strength of:

$$B = \sqrt{2\Omega\rho Re_M/\sigma}. \quad (3.7)$$

Using magnetic Reynolds numbers on the order of 10-1000 (10 is the minimum  $Re_M$  value for dynamo action), and  $\rho = 8 \times 10^3$  as an estimate of the density of the outer core, we obtain an estimate for the field strength of  $10^5 - 10^7$  nT, which is in the same range as was found using the energetic arguments.

The magnetic field estimate provided by these two methods does not immediately conflict with the observed field value since the estimate is of the field strength in the fluid core, rather than at some distance outside the core where the observations are made. As mentioned in section 1.1, the magnetic field can be decomposed into its toroidal ( $\mathbf{B}_T$ ) and poloidal ( $\mathbf{B}_P$ ) components. Since the toroidal field has no radial component, it is not observable outside the conducting core and only the poloidal field is measured outside the dynamo generation region. The magnetic field estimate given by the energy and magnetostrophic balance arguments pertains to the combination of the toroidal and poloidal field components in the core. If one assumes that the toroidal field is dominant, then the field estimates obtained above pertain to the toroidal field strength, and do not directly restrict the strength of the observed field outside the core which is an extension of the poloidal field.

**Table 3.3:** Model parameters and results. The average, median, maximum and minimum values of the  $B_{Dip}/B_T$  ratio over two magnetic diffusion times are given.

Model	$r_{io}$	$Ra_m$	$B_{Dip}/B_T$			
			mean	median	max	min
1	0.35	15000	$1.3 \cdot 10^{-1}$	$1.2 \cdot 10^{-1}$	$1.7 \cdot 10^{-1}$	$1.0 \cdot 10^{-1}$
2	0.35	18000	$1.3 \cdot 10^{-1}$	$1.3 \cdot 10^{-1}$	$1.7 \cdot 10^{-1}$	$1.0 \cdot 10^{-1}$
3	0.35	24000	$1.5 \cdot 10^{-1}$	$1.6 \cdot 10^{-1}$	$2.0 \cdot 10^{-1}$	$1.1 \cdot 10^{-1}$
4	0.7	18000	$1.5 \cdot 10^{-1}$	$1.5 \cdot 10^{-1}$	$2.0 \cdot 10^{-1}$	$1.1 \cdot 10^{-1}$
5	0.8	25000	$1.0 \cdot 10^{-2}$	$1.2 \cdot 10^{-2}$	$2.3 \cdot 10^{-2}$	$2.3 \cdot 10^{-3}$
6	0.8	30000	$1.9 \cdot 10^{-2}$	$2.1 \cdot 10^{-2}$	$5.2 \cdot 10^{-2}$	$6.7 \cdot 10^{-3}$
7	0.8	40000	$7.9 \cdot 10^{-2}$	$8.3 \cdot 10^{-2}$	$1.3 \cdot 10^{-1}$	$4.2 \cdot 10^{-2}$
8	0.83	45000	$1.1 \cdot 10^{-2}$	$1.4 \cdot 10^{-2}$	$3.2 \cdot 10^{-2}$	$1.7 \cdot 10^{-3}$
9	0.9	60000	$8.7 \cdot 10^{-2}$	$8.8 \cdot 10^{-2}$	$1.9 \cdot 10^{-1}$	$5.6 \cdot 10^{-2}$
10	0.9	70000	$8.4 \cdot 10^{-2}$	$8.3 \cdot 10^{-2}$	$1.7 \cdot 10^{-1}$	$5.0 \cdot 10^{-2}$

The problem arises when one compares the dipole field strength at Mercury's core-mantle boundary (assumed to be representative of the poloidal field strength at the core-mantle boundary) to the toroidal field strength in Mercury's core (estimated using the energy or magnetostrophic balance arguments). The ratio of these fields is  $B_{Dip}/B_T \approx 10^{-2} - 10^{-4}$ . By carrying out a similar analysis for Earth's dynamo, we find  $B_{Dip}/B_T \approx 10^{-1}$ . This is where a dynamo solution for Mercury's field becomes problematic since it appears that Mercury's dynamo produces a much smaller  $B_{Dip}/B_T$  ratio than Earth's dynamo and it is unclear why this should be the case.

In the rest of this chapter we investigate whether Mercury's non-Earth-like field partitioning is the result of a different convective region geometry for the planet. Since the thermal evolution models in section 3.3 suggest Mercury core may be comprised of a large solid inner core surrounded by a thin liquid outer core, we examine whether a thin shell dynamo could explain the much smaller  $B_{Dip}/B_T$  ratio found for Mercury. One possibility is that the ratio of poloidal field to toroidal field in the core ( $B_P/B_T$ ) may be smaller if the generation of toroidal field is more efficient than the generation of poloidal field. Another possibility is that the poloidal field may be dominated by smaller-scale structure than the dipole leading to a smaller  $B_{Dip}/B_P$  ratio. This would imply that projecting the dipole field observed by Mariner 10 to the CMB does not provide a good estimate for the CMB poloidal field at Mercury (unlike the Earth case where it is believed the dipole component at the CMB does provide a good estimate for the poloidal field strength there). In the following sections we examine both of these possibilities using numerical dynamo modeling.

### 3.5 Numerical Model Results

Using the numerical model outlined in section 1.4, we examine the effect of varying the non-dimensional inner core radius  $r_{io}$  (see equation 1.31) and the modified Rayleigh number  $Ra_m$  (see equation 1.32) on the morphology of the produced magnetic fields.

### 3.5.1 Toroidal and Poloidal Field Partitioning

We will begin by examining the partitioning of magnetic field among the toroidal and poloidal components. Table 3.3 lists the control parameters and results of each model studied. We use the non-dimensional  $L_2$  norm of the toroidal field to estimate its magnitude:

$$B_T = \left( \int_V |\mathbf{B}_T|^2 dV \right)^{1/2}, \quad (3.8)$$

where  $V$  is the non-dimensional volume of the fluid outer core. For  $B_{Dip}$ , we find the dipole moment of the field at the surface and downward project it to Mercury's core mantle boundary, assumed to be at 0.75 planetary radii:

$$B_{Dip} = \left( \frac{R_M}{R_{CMB}} \right)^3 \sqrt{(g_1^0)^2 + (g_1^1)^2 + (h_1^1)^2}, \quad (3.9)$$

where  $R_M$  is Mercury's total radius and  $R_{CMB}$  is the core-mantle boundary radius.

Models 1-3 which have an Earth-like inner core size, produce  $B_{Dip}/B_T$  ratios of about  $10^{-1}$  which is the same as the theoretical estimates for Earth's dynamo. For thinner shells we observe a more varied behavior. Some models have  $B_{Dip}/B_T$  ratios on the order of  $10^{-2}$  with minimum values on the order of  $10^{-3}$  (models 5,6 and 8) whereas others (models 4,7,9,10) have average ratios similar to the Earth-like cases. However, for some of the thinner shells (larger inner core radii) with Earth-like average ratios (models 8,10,11) we find the range of values obtained over the two diffusion times is larger than the range of values exhibited by the Earth-like shell thickness (i.e. their ratios are more variable).

The two factors that affect the  $B_{Dip}/B_T$  ratio were mentioned in section 3.4. Figure 3.2 shows that for a numerical model with small  $B_{Dip}/B_T$  ratio, both the  $B_P/B_T$  and the  $B_{Dip}/B_P$  ratios are smaller than a numerical model with Earth-like  $B_{Dip}/B_T$  ratio (We used the  $L_2$  norm of the poloidal field to estimate  $B_P$ ). Although we only plot the results for two of the models, the results are representative of all our models in Table 3.3. Both of these effects contribute a factor of order  $10^{-1}$  to the  $B_{Dip}/B_T$  ratio resulting in ratios on the order of  $10^{-2}$ . It therefore appears that thin shell dynamos are both less efficient at producing poloidal field from toroidal field and produce smaller scale poloidal field than Earth-like models. This may not be a coincidence since perhaps poorly generated poloidal field naturally results in smaller scale structure.

The three models with smaller  $B_{Dip}/B_T$  ratios also share other similar characteristics (and differences from models with larger  $B_{Dip}/B_T$  ratios). In the following sections we will examine some of these characteristics.

### 3.5.2 Symmetry of Field Partitioning

In Figures 3.3 and 3.4 we compare the partitioning of poloidal and toroidal energy in the core (energy components defined in equation 2.12) into axisymmetric and non-axisymmetric components for models 6 and 7. These models have the same  $r_{io}$  value but model 6 has a small  $B_{Dip}/B_T$  ratio and model 7 has an Earth-like  $B_{Dip}/B_T$  ratio. The model with smaller  $B_{Dip}/B_T$  ratio has a poloidal energy dominated by the non-axisymmetric component and toroidal energy dominated by the axisymmetric component. In contrast, the Earth-like  $B_{Dip}/B_T$  ratio model has both poloidal and

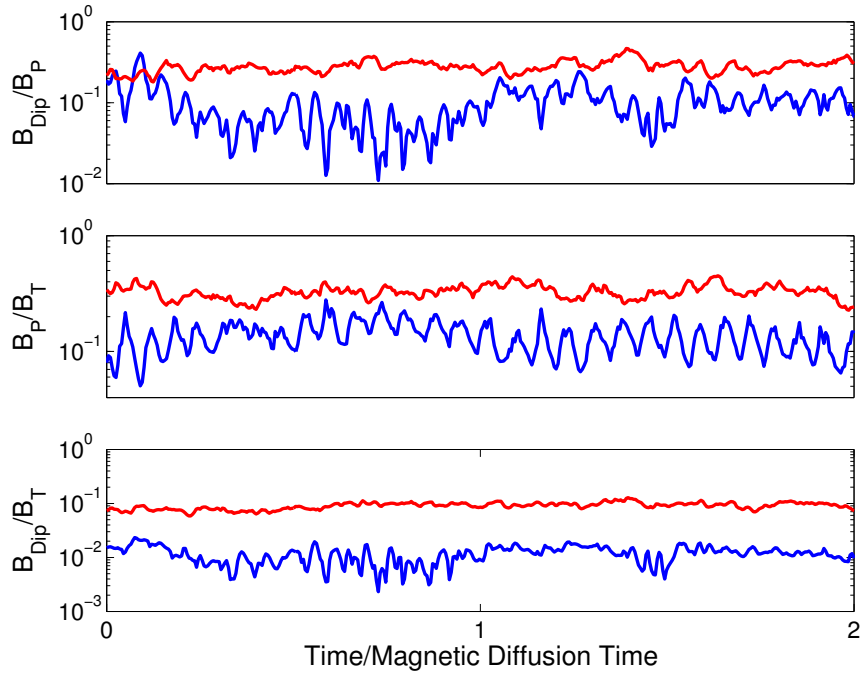


**Figure 3.2:** Magnetic field ratios as a function of time for model 5 (blue) and model 7 (red). The ratio of the dipole field at the CMB (assumed to be at 0.75 planetary radii) to the poloidal field in the core is shown in the top plot, poloidal field to toroidal field ratios in the core are shown in the middle plot, and dipole field at CMB to toroidal field in the core are shown in the bottom plot. Time is given in units of magnetic diffusion time.

toroidal energy dominated by the axisymmetric component. The dominant axisymmetric toroidal energy in both models is not surprising since it is generated through the shearing action of differential rotation which is present in both cases. The difference in poloidal energy dominance suggests that the mechanism generating poloidal field behaves differently in the two models. There also appears to be a periodic oscillation in the non-axisymmetric toroidal and poloidal energies in model 6 that is not evident in model 7.

### 3.5.3 Eccentric Dipole Models

Another characteristic we can compare is eccentric dipole models. Figure 3.5 plots the eccentric dipole tilts and offsets for models 1, 5 and 7. The model with small  $B_{Dip}/B_T$  ratio experiences larger variations in dipole tilt and offset than the thin shell model with Earth-like  $B_{Dip}/B_T$  ratio and the thick-shell Earth-like model. These results are characteristic of the other models in Table 3.3 that have similar  $B_{Dip}/B_T$  ratios. The larger eccentric dipole tilts and offsets of models with small  $B_{Dip}/B_T$  ratio do not only occur during reversals (as the one shown in Figure 3.5), but also during times of stable polarity direction. Only two of the three small  $B_{Dip}/B_T$  ratio models in Table 3.3 underwent a reversal at some point during the two diffusion times studied, however all three demonstrated similar variability in dipole tilt and offset when not reversing.

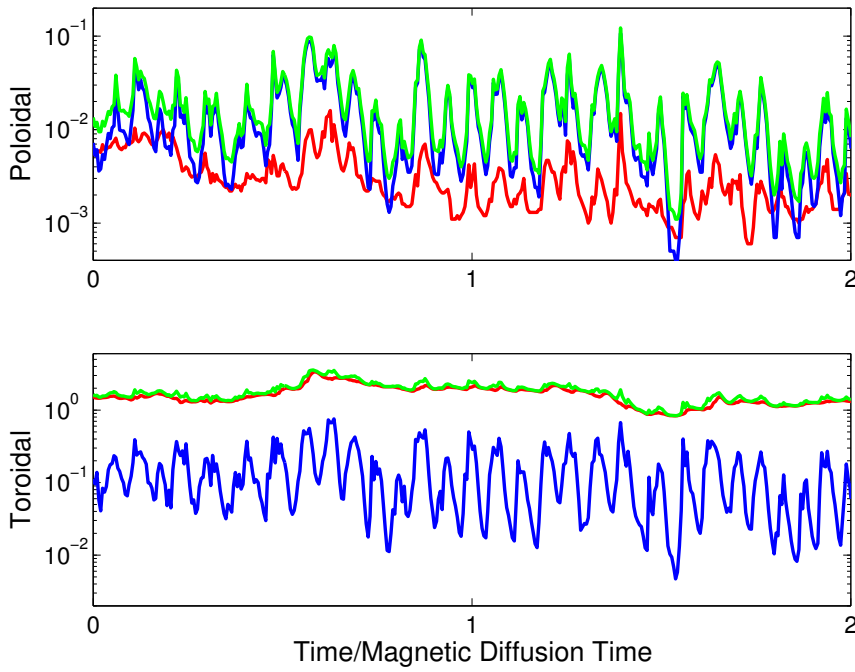


**Figure 3.3:** Magnetic energy components as a function of time for model 6. The axisymmetric (red), non-axisymmetric (blue) and total (green) non-dimensional energy for the poloidal (top) and toroidal (bottom) fields are shown. Time is given in units of magnetic diffusion time.

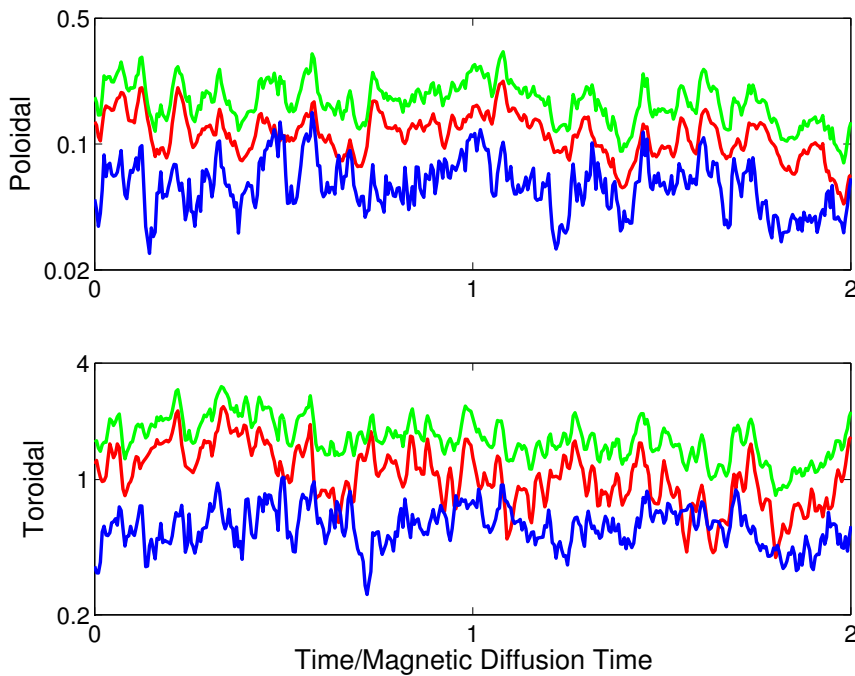


**Figure 3.4:** Same as 3.3 but for model 7.

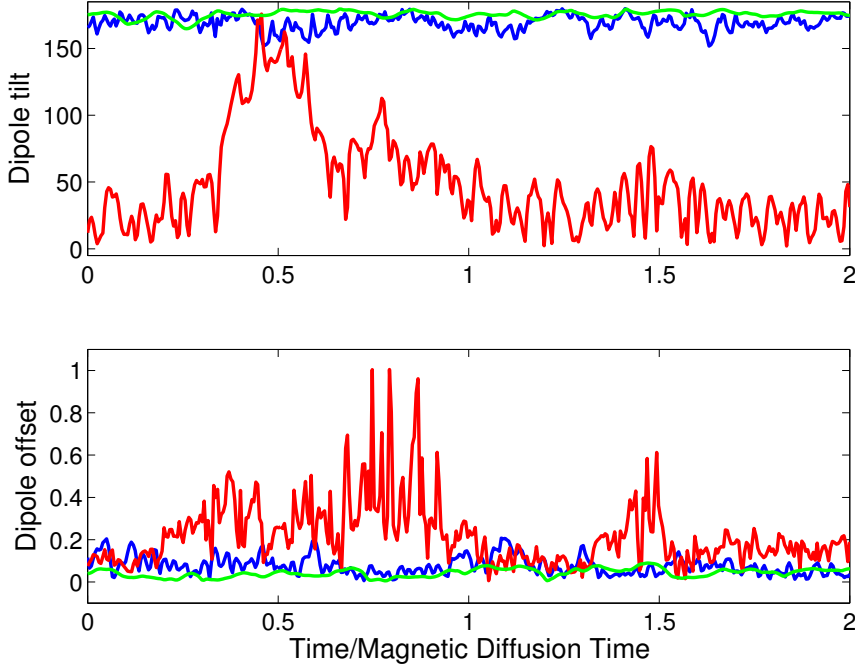


**Figure 3.5:** Eccentric dipole models as a function of time. Dipole tilt (top) and offset (bottom) are shown for models 1 (green), 5(blue) and 7(red). Time is given in units of magnetic diffusion time and dipole offset is in units of planetary radii.

### 3.5.4 Axisymmetric Magnetic Field Plots

Although some of the thin shell models produce Earth-like  $B_{Dip}/B_T$  ratios, there are differences between the fields generated by these dynamos and thick-shell dynamos. Figure 3.6 compares the axisymmetric toroidal and poloidal fields in models with various shell thicknesses, but Earth-like  $B_{Dip}/B_T$  ratios. The dominant pattern of toroidal magnetic field changes as the shell thickness varies. The thick-shell model in Figure 3.6(a) is dominated by a spherical harmonic degree 2 pattern which remains relatively stable in time. In contrast, the very thin-shell model in Figure 3.6(d) is dominated by a degree 4 pattern in both the time-averaged field and at the time step shown, however this model can also display a more complex toroidal field with contributions from multiple spherical harmonic degrees at certain times. For intermediate shell thicknesses (Figures 3.6(b) and (c)) the pattern appears to be going through a transition between the two states and therefore contains more complicated structure with significant contributions from both degree 2 and 4 components. The change to higher-degree (smaller scale) structure as the shell thickness decreases is perhaps not surprising since a length-scale in the problem is becoming smaller, however it is interesting that these different toroidal field morphologies still produce a dominant dipolar poloidal field.

We can also compare model 7's axisymmetric magnetic field to that of model 6, which has the same shell thickness but a small  $B_{Dip}/B_T$  ratio. Figure 3.7 plots the axisymmetric toroidal and poloidal fields for model 6. By comparing Figures 3.6(c) and 3.7, we see that although the shell thickness is the same, the toroidal field pattern is different. In model 6 the axisymmetric toroidal field is concentrated inside the tangent cylinder whereas in model 7 the toroidal field is found throughout the fluid core.

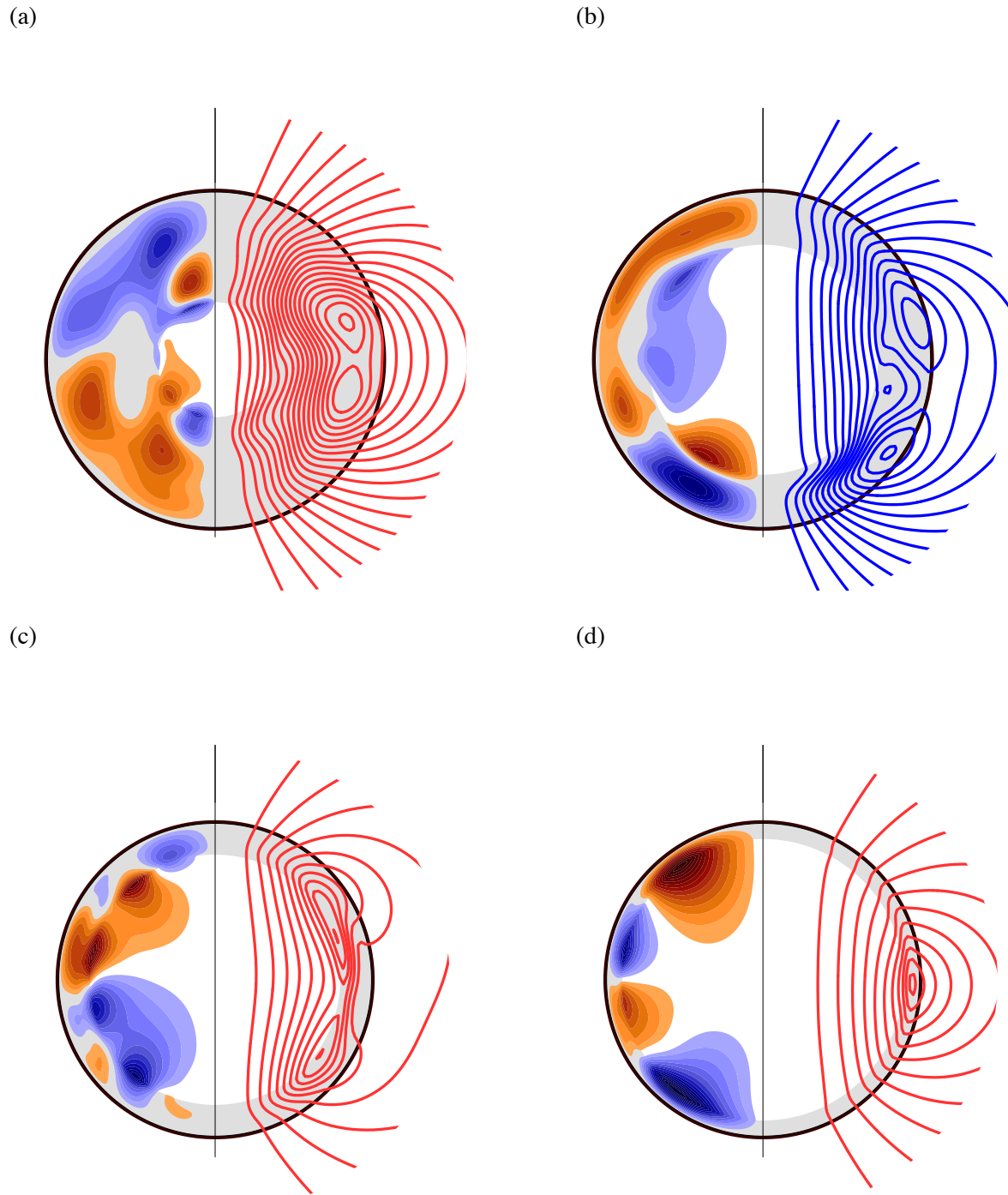


**Figure 3.6:** Axisymmetric magnetic field at one instant in time for models 2 (a), 4 (b), 7 (c) and 9 (d). Contours of the toroidal field are shown in the left half and streamlines of the poloidal field are shown in the right half of the plots. The different colors represent different field directions. The grey shell is the fluid core, the inner white region is the solid inner core, the thick black circle is the CMB and the black vertical line represents the rotation axis.

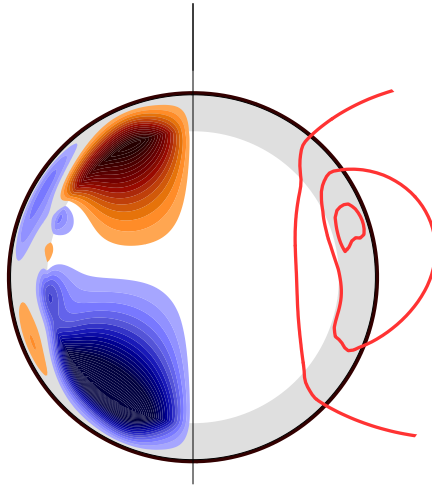


**Figure 3.7:** Same as Figure 3.6 but for model 6.

---

### 3.5.5 Axisymmetric Velocity Field Plots

There are also differences in the axisymmetric velocity fields of models with different  $B_{Dip}/B_T$  ratios. Figure 3.8 plots the axisymmetric toroidal and poloidal velocity fields in a meridional plane for models 6 and 7. Both models have similar toroidal velocity patterns outside the tangent cylinder, however their velocities inside the tangent cylinder are quite different. The model with smaller  $B_{Dip}/B_T$  ratio has a columnar differential rotation pattern inside the tangent cylinder which is not seen in the model with Earth-like  $B_{Dip}/B_T$  ratio. Model 6 also has a larger partitioning of its kinetic energy in the axisymmetric component of the field and some stronger velocity patterns near the rotation axis inside the tangent cylinder.

The velocity fields suggest that the models behave similarly outside the tangent cylinder, but that there are differences inside the tangent cylinder. This is also seen in the axisymmetric temperature perturbation fields in the models shown in Figure 3.9. If we examine the region outside the tangent cylinders in both models, they are fairly similar, displaying a high degree of equatorial symmetry. However, inside the tangent cylinder, the models have opposite symmetries. Model 6 displays an equatorially antisymmetric pattern, whereas model 7 has a symmetric pattern<sup>1</sup>.

---

<sup>1</sup>For those who have read chapter 2: The temperature perturbation field shown for a model with insulating inner core (Figure 2.20(right)) displayed an equatorially antisymmetric pattern throughout the core, not only inside the tangent cylinder as it does in model 6 here. Although the arrows in Figure 3.8 may be a bit small in the equatorial region to discern, we do not see the thermal wind pattern in this model that was seen in the insulating inner core model (Figure 2.19). We also don't see the tilt in differential rotation pattern that was seen in Figure 2.19.

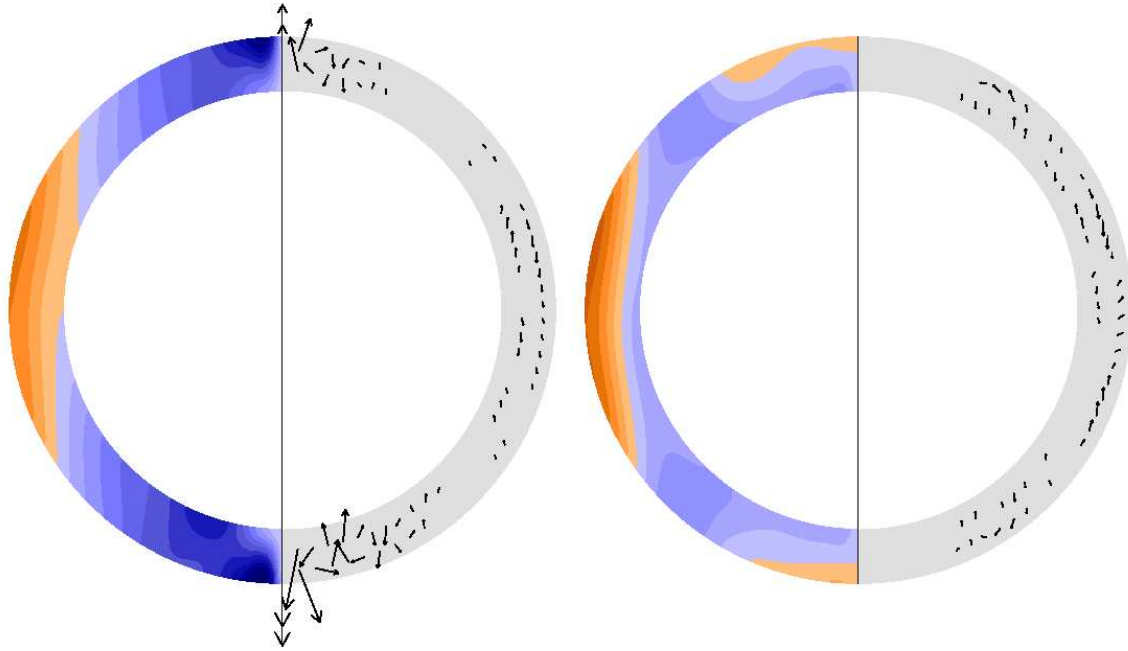


**Figure 3.8:** Axisymmetric velocity field in a meridional slice for models 6 (left) and 7 (right). Contours of the toroidal field are plotted in the left half and flow vectors of the poloidal field are plotted in the right half.

## 3.6 Discussion

The purpose of this study was to determine whether numerical dynamos with non-Earth-like  $B_{Dip}/B_T$  ratios existed, and this was accomplished, but our search of parameter space was not complete enough to determine the specific dependence of the  $B_{Dip}/B_T$  ratio on shell thickness and modified Rayleigh number. We do however observe some trends that will be verifiable once a further study of parameter space has been conducted.

### 3.6.1 Trends in the Models

Models 5-7 have the same inner core radius ( $r_{io} = 0.8$ ) but different modified Rayleigh numbers. The results suggest that lower modified Rayleigh numbers are able to produce fields with smaller  $B_{Dip}/B_T$  ratios. When we lowered the modified Rayleigh number to  $Ra_m = 20000$  for the same shell thickness, the strong field dynamo solution died. This suggests that modified Rayleigh numbers in a limited region near the lower boundary for strong field dynamo action in our numerical models can produce smaller  $B_{Dip}/B_T$  ratios. In future work we will examine whether this trend prevails at other inner core radii. The two models with  $r_{io} = 0.9$  (models 9 and 10) produce Earth-like ratios at their modified Rayleigh numbers. In a model with the same inner core radius and  $Ra_m = 30000$  we found the strong-field dynamo died. If dynamos operating at this shell thickness can produce smaller  $B_{Dip}/B_T$  ratios, our results from the  $r_{io} = 0.8$  case suggest it will occur somewhere in the  $Ra_m$  range of 30000-60000. This trend does not appear to occur for Earth-like shell thicknesses since model 1, which has an Earth-like  $B_{Dip}/B_T$  ratio, has a modified Rayleigh number very close to the critical value for strong field dynamo action (Kuang and Bloxham, 1999). This suggests that

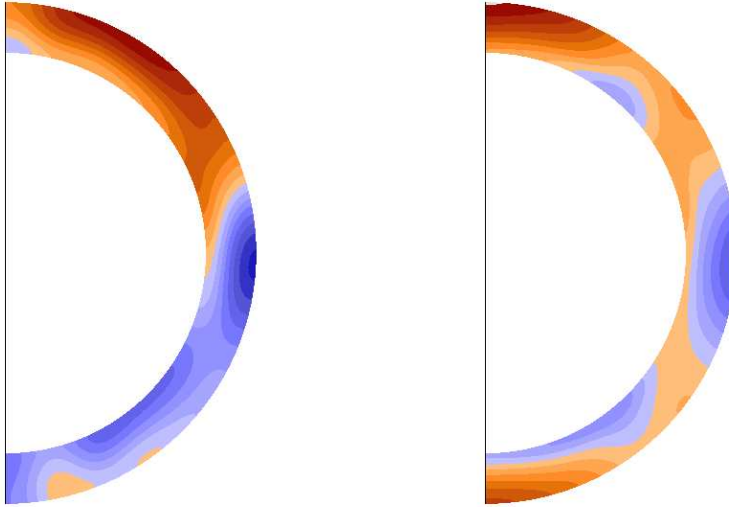


**Figure 3.9:** Axisymmetric temperature perturbation field in a meridional slice through the dynamo source region at one instant in time for models 6 (left) and 7 (right).

the field partitioning has a dependence on shell thickness as well as on modified Rayleigh number. Determining the critical shell thickness for which this trend begins to appear will be the goal of future parameter space searches.

### 3.6.2 Cause of Non-Earth-like Field Partitioning

In this section we examine the possible cause of this different field morphology. As a consequence of the Proudman-Taylor theorem (Proudman, 1916; Taylor, 1917), the convection pattern in a spherical rapidly rotating shell is dominated by 2-dimensional columnar rolls (Busse, 1970, 2002) that form parallel to the rotation axis outside the tangent cylinder. Convection inside the tangent cylinder is more difficult since the geometry requires the complex 3-D motions that transfer heat from the inner core boundary to the CMB to break the 2-dimensionality imposed by the Proudman-Taylor theorem. In a thick shell geometry, these convection columns are an efficient means of producing poloidal magnetic field from toroidal field since the region outside the tangent cylinder occupies a large fraction of the fluid core's volume and the toroidal field is present throughout this region. However, as the shell thickness decreases, the region outside the tangent cylinder occupies a smaller ratio of the total volume and therefore, the convective motions outside the tangent cylinder do not interact as efficiently with the toroidal field which is present in the entire fluid shell. The ratio of magnetic field generation to dissipation is given by the magnetic Reynolds number ( $Re_M = UL/\eta$ ), which is proportional to the characteristic length ( $L$ ) and velocity ( $U$ ) scales. As the shell thickness decreases, the velocity (i.e. the convective vigor) must increase in order to maintain the same level of field generation (same  $Re_M$ ). One might expect that at a certain shell thickness, the Rayleigh numbers required to maintain strong field dynamo action outside the tangent cylinder may be similar to those for the onset of dynamo action inside the tangent cylinder.

We can now provide a possible explanation for both the shell thickness and Rayleigh number dependencies seen in our models. The toroidal field is generated efficiently in both thick and thin

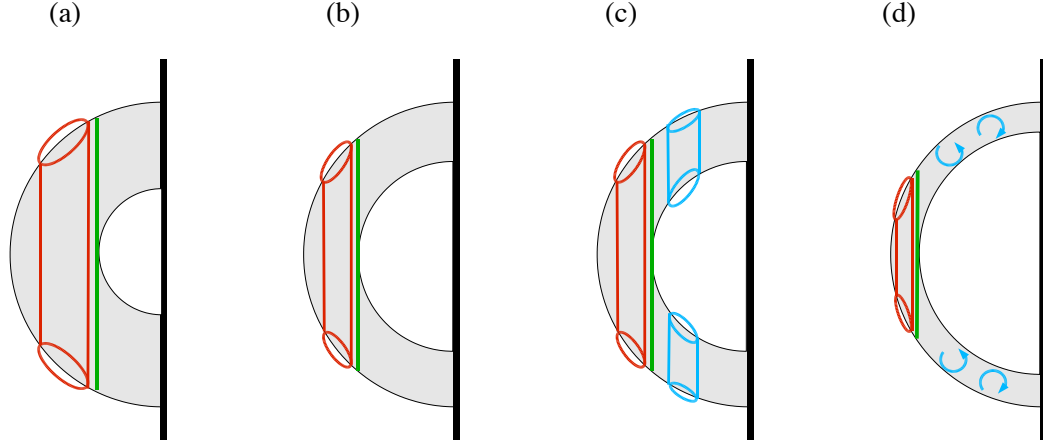


**Figure 3.10:** Sketch of theoretical convective flow patterns in meridional slices for models with varying shell thicknesses. The black and green lines represent the rotation axis and tangent cylinder respectively, gray regions are the fluid outer core and inner white regions are the solid inner core. A thick shell geometry (a) has a convection pattern dominated by columnar rolls (red cylinders) that form near the tangent cylinder. This form of convection is efficient at generating poloidal dipolar field and produces Earth-like  $B_{Dip}/B_T$  ratios. As shell thickness decreases, the convection columns become shorter and move to regions of higher boundary slope. If the Rayleigh number is low enough so that convection does not occur inside the tangent cylinder, then these rolls are not efficient at converting toroidal field to poloidal dipole field (b) and these dynamos can produce smaller  $B_{Dip}/B_T$  ratios. At similar shell thicknesses but higher Rayleigh numbers, convection inside the tangent cylinder is more efficient at producing poloidal dipole field (c) causing Earth-like  $B_{Dip}/B_T$  ratios. Eventually a shell thickness may be reached where dynamo action inside and outside the tangent cylinder begin at similar critical Rayleigh numbers, eliminating the small  $B_{Dip}/B_T$  ratio regime.

shells through differential rotation ( $\omega$  effect). The poloidal field is generated when upwellings from convection produce poloidal field from toroidal field (macroscopic  $\alpha$  effect). In our numerical thick shell dynamos these processes result in a  $B_{Dip}/B_T$  ratio of about  $10^{-1}$ . As the shell thickness decreases, columnar convection becomes less efficient at producing poloidal field from toroidal field because the columns occur in a limited region outside the tangent cylinder. We obtain dynamos with small  $B_{Dip}/B_T$  ratios in the parameter regime when convection outside the tangent cylinder is not as efficient at producing poloidal field (i.e. thin shells) and the modified Rayleigh number is low enough that convection inside the tangent cylinder does not efficiently produce poloidal field. We obtain Earth-like  $B_{Dip}/B_T$  ratios in thin shell geometries when the Rayleigh number is large enough that convection inside the tangent cylinder is capable of producing a strong poloidal field from the strong toroidal field there. This is why models 5 and 6 have small  $B_{Dip}/B_T$  ratios whereas model 7, which has the same shell thickness but larger modified Rayleigh number, has an Earth-like  $B_{Dip}/B_T$  ratio. Small  $B_{Dip}/B_T$  ratios will no longer occur in dynamos where the shell thickness is small enough that either convection outside the tangent cylinder alone is not efficient enough to produce dynamo action (can't get to critical  $Re_M$ ), or dynamo action inside and outside the tangent cylinder occur at similar critical Rayleigh numbers. At this point the convection inside and outside the tangent cylinder will be an efficient means of producing poloidal field and Earth-like  $B_{Dip}/B_T$  ratios will result. A sketch of these different scenarios is shown in Figure 3.10.

We see evidence of this process occurring in our dynamo models. In Figures 3.11 and 3.12 we show the horizontal fluid flow in slices parallel to the equator of models 5 and 7 respectively. For the slices in the equatorial plane (part (a) in both figures), both slices contain similar convection

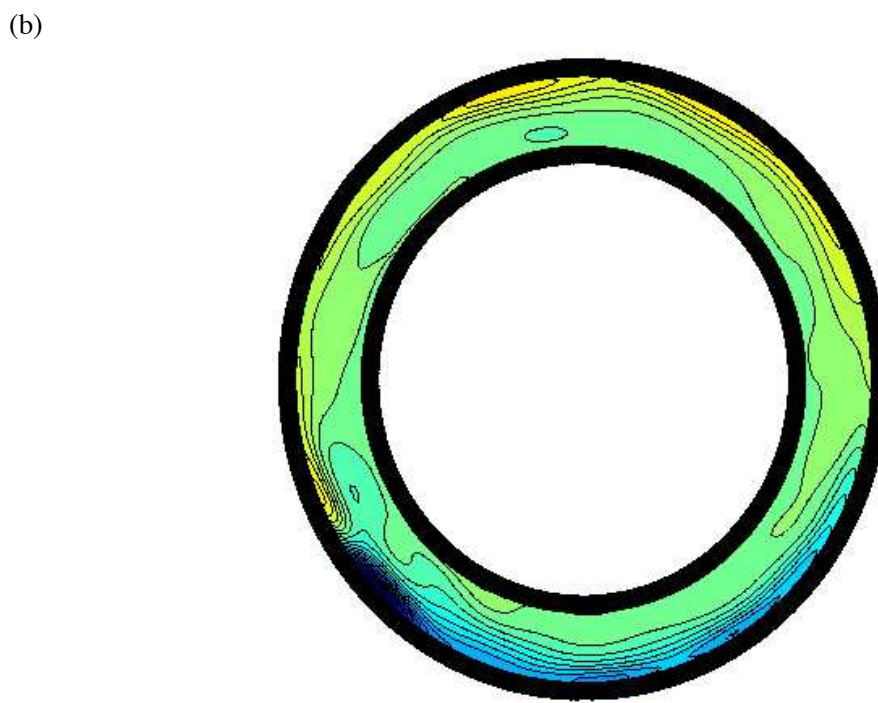
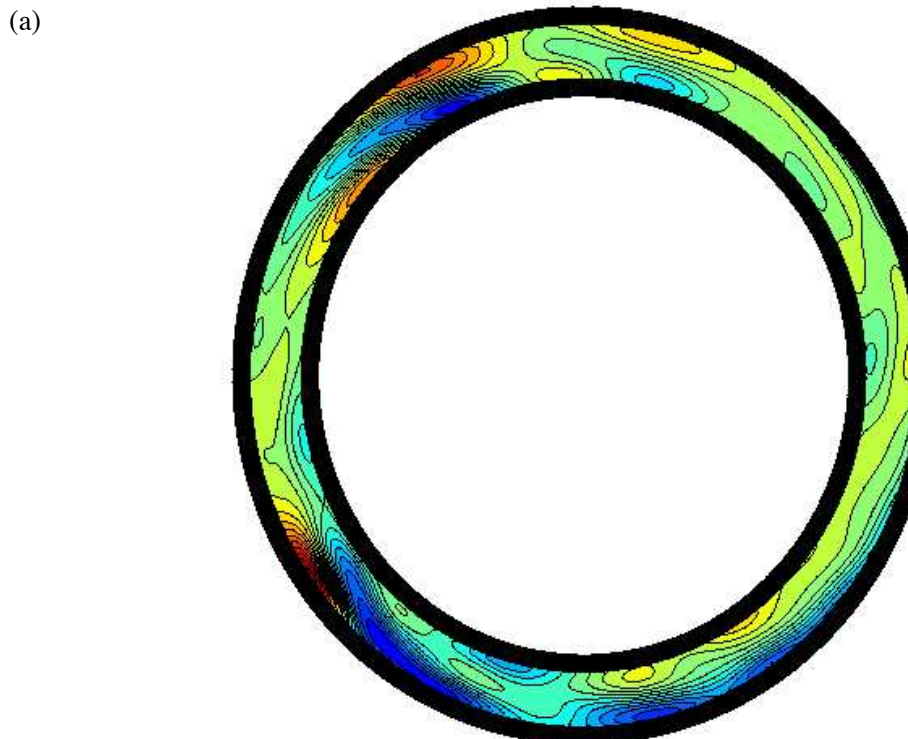
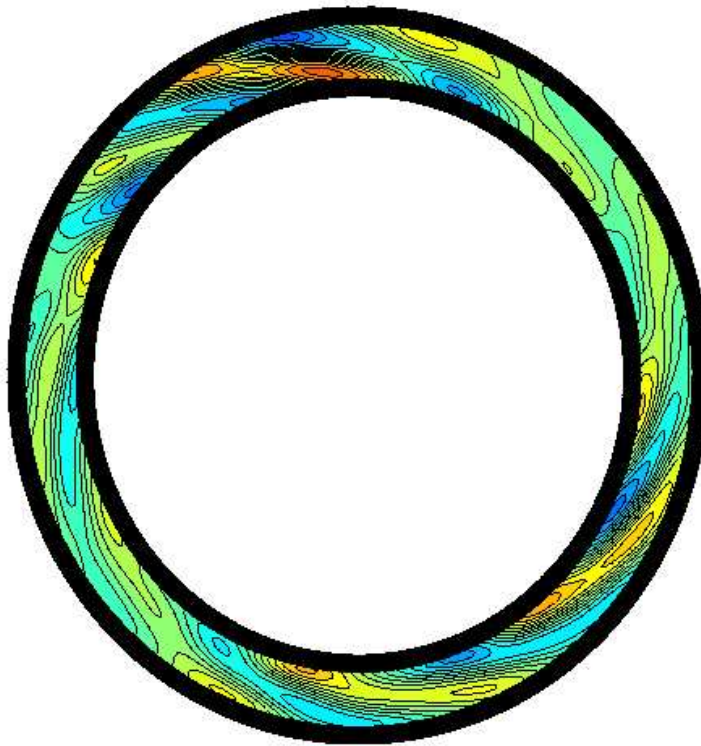


**Figure 3.11:** The non-axisymmetric poloidal velocity field in slices parallel to the equatorial plane for model 5. The contours are of the curl of the horizontal velocity field. A slice through the equatorial plane is shown in (a) and a slice through a plane parallel to the equatorial plane at a height of  $0.5 r_o$  is shown in (b).

(a)



(b)

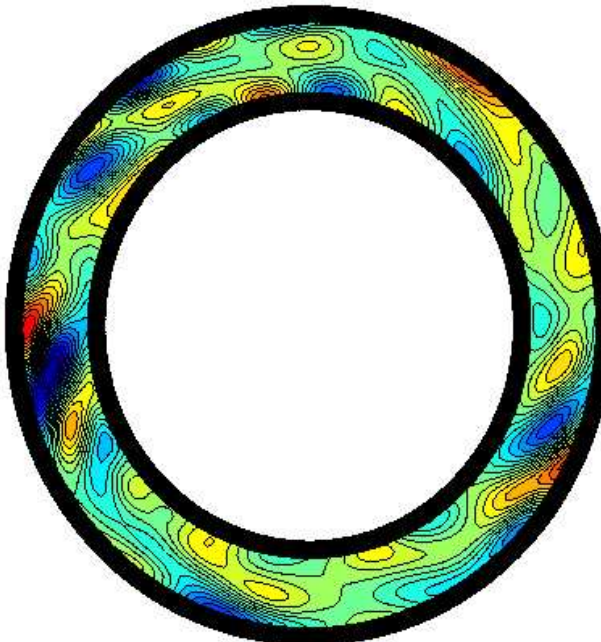


**Figure 3.12:** Same as Figure 3.11 but for model 7.

patterns occurring outside the tangent cylinder, however model 7 appears to be convecting more vigorously as expected since the modified Rayleigh number is larger in this model. We see these convection patterns at similar radii in slices through other planes parallel to the equatorial plane, demonstrating their columnar nature. However, in part (b) of both figures, we plot the convection pattern occurring in a plane parallel to the equatorial plane at a height  $z = 0.5r_o$ . In this plane, most of the fluid is contained inside the tangent cylinder. Here is where the difference between the two models is seen. At lower Rayleigh number, convection columns have not begun to form inside the tangent cylinder (Figure 3.11(b)), whereas at higher Rayleigh number, we see the convection patterns inside the tangent cylinder (Figure 3.12(b)).

### 3.6.3 Future Work

We have demonstrated that dynamos operating in thin shells can produce a variety of behaviors not seen in thick-shell dynamos. Further study of this geometry is necessary for understanding the magnetic field generation process in planets and may be relevant for Mercury as well as Ganymede and perhaps Mars' past dynamo. Al-Shamali *et al.* (2004) have recently performed numerical studies of the onset of convection in thin shells and Aurnou *et al.* (2003) have performed experiments on convection patterns inside the tangent cylinder. Both of these forms of study, along with numerical dynamo studies will be important in understanding dynamo generation in thin shells. In future work we will explore more of parameter space in our numerical models to determine the dependence of this new field morphology on the governing parameters.

This first study has shown that a dynamo solution for Mercury's magnetic field is possible since thin shell dynamos can produce fields with Mercury-like partitioning of toroidal and poloidal fields, however, it does not rule out crustal magnetization or a thermoelectric dynamo as the source of Mercury's field. Future measurements of Mercury's magnetic field by the MESSENGER and Bepi-Colombo missions may help to resolve the issue. If any secular variation of the field is observed, then the dynamo source will prove correct. If the field structure is correlated with gravity signatures indicating topography at the core-mantle boundary, then a thermoelectric dynamo will be the most likely answer. Any small scale structure with shallow source depths is crustal in origin. If no secular variation is detected this does not mean the field is not dynamo generated, just that the timescale of secular variation is longer than the length of time the observations are carried out. Determining whether the field is crustal or dynamo generated in this case may be possible if evidence of an effect due to the tangent cylinder is seen. If the character of the magnetic field is different inside and outside the tangent cylinder (due to different convection patterns in these regions) then a dynamo source for the field may be the answer.



## Chapter 4

# Conclusions and Future Work

Given our discussion in the previous chapters of the importance of symmetry in characterizing planetary magnetic fields, it seems fitting that the title of this thesis, '*So Many Dynamos*', is also symmetric (its a palindrome). The title also conveys the fact that our solar system presents us with various field morphologies and the purpose of this thesis was to examine the cause of these different morphologies. We found that the three different classes of fields can be explained by different convective region geometries:

- Uranus' and Neptune's non-dipolar, non-axisymmetric fields appear to be the result of dynamo action in a thin shell surrounding a stably-stratified fluid interior,
- Mercury's weak surface field may be the result of a thin shell convective-region geometry combined with a restricted location of poloidal field generation,
- Earth, Jupiter, Saturn and Ganymede possess strong axially-dipolar dominated fields because their dynamos work in either thick shell geometries, or (possibly for Ganymede since we don't know much about its interior) thinner shell geometries surrounding conducting inner cores.

The results presented in this thesis are not only important for the study of these planets' dynamos, but also indicate that magnetic fields can be an important tool for studying planetary interiors. If we can determine the characteristics of a planet's magnetic field that relate to its interior structure or composition, then we can use a magnetic field as a probe of the planet's internal make-up. On Earth, seismology determined the size of the solid inner core, but remote spacecraft observations of the other terrestrial planets and moons have not provided similar information. A seismological investigation of another planet's core would require multiple landers and has so far not been feasible. On a similar note, studying the interiors of the giant planets has been limited to observations of the gravity field, surface expressions of the interiors and experimental/theoretical work. Magnetic fields may provide us with another tool to carry out these investigations and has the attractive property of being relatively inexpensive when compared to multiple lander seismology missions.

In previous chapters we mentioned some future work we will carry out on those topics. In the most general terms, future work will involve conducting a larger survey of parameter space, in order to determine the dependencies of field morphology on properties such as the inner core radius,

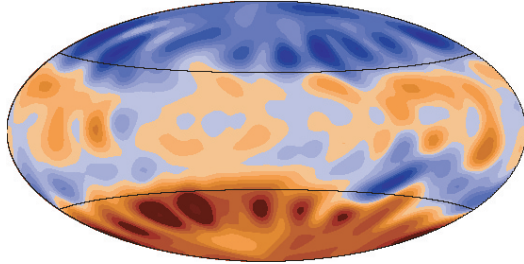


**Figure 4.1:** Correspondence of magnetic field structure and the tangent cylinder. The radial magnetic field at the core-mantle boundary of a thin shell dynamo model with  $r_{io} = 0.8$  and  $Ra_m = 40000$ . The black curves indicate the projection of the tangent cylinder on the core mantle boundary.

---

presence of stable regions and driving forces. Some other specific ideas for future work are outlined below.

### Tangent Cylinder Effects

As we saw in the previous chapters, the location of the inner core tangent cylinder changes when the size of the inner core changes and the processes governing magnetic field generation inside and outside the tangent cylinder can be quite different. If these processes lead to different magnetic field structures near the core-mantle boundary for these fields, then we may be able to determine the inner core radius by studying the magnetic field. An illustrative example is shown in Figure 4.1 which plots the radial magnetic field at the core-mantle boundary of a model with a large solid inner core. There is a clear correspondence in this figure between the projection of the tangent cylinder on the core-mantle boundary and the change in radial field patterns. There may also be useful relationships between surface magnetic power spectra and inner core size or driving force. Figure 4.2 demonstrates the differences in the surface magnetic power spectra for numerical dynamo models with various inner core radii and Rayleigh numbers.

### Time Dependence

At present, except for Earth's field, we have very little information on the time variation of planetary magnetic fields. The numerical models studied in this thesis are highly variable in time. Numerical models of Earth's magnetic field reproduce the secular variation rates of the observed field quite well (Kuang and Bloxham, 1997), suggesting that perhaps a combination of time-dependent observations of other planetary fields and analysis of the time variability of numerical models can provide insight into the dynamics of the dynamo source regions. For example, the drift rate of features outside the tangent cylinder may be correlated with the velocity patterns in this region. Our models show differences in both the toroidal and poloidal velocity fields in this region for different geometries studied.

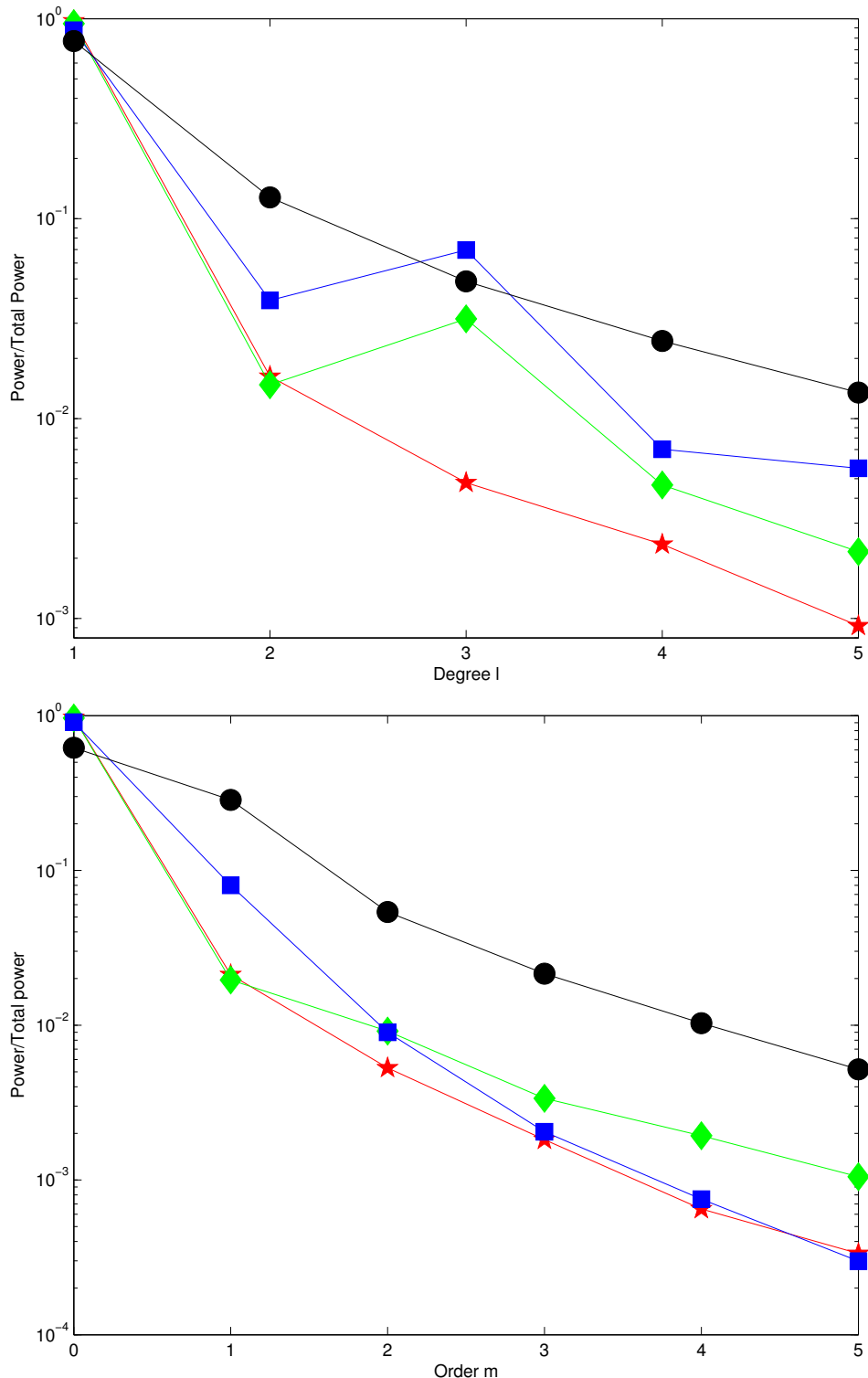


**Figure 4.2:** Correspondence of surface power spectra and inner core radius. Average surface power vs. degree is shown in (a) and vs. order is shown in (b). Models with different  $r_{io}$  and  $Ra_m$  are shown:  $r_{io} = 0.35, Ra_m = 18000$  (red stars),  $r_{io} = 0.8, Ra_m = 25000$  (black circles),  $r_{io} = 0.8, Ra_m = 40000$  (blue squares),  $r_{io} = 0.9, Ra_m = 60000$  (green diamonds).

## **Death of the Martian Dynamo**

Magnetic field measurements made by the Mars Global Surveyor mission show that Mars has a remanent crustal magnetic field most likely due to a dynamo operating in its early history (Acuna *et al.*, 1999; Connerney *et al.*, 1999). The timing of the dynamo depends on the heat flow from the core which is directly related to the form of mantle convection and the initial conditions of Mars' cooling (Arkani-Hamed, 2004; Breuer and Spohn, 2003; Nimmo and Stevenson, 2000; Stevenson, 2001, 2003b; Williams and Nimmo, 2004). Several possibilities for the cause of the Martian dynamo's death have been proposed and directly relate to the thermal history of the planet.

We will use numerical dynamo modeling to examine one of the possible causes for the Martian dynamo's death outlined by Stevenson (2001): the solid inner core in Mars eventually grew too large, resulting in a shell thickness too small to sustain dynamo action. We will determine the necessary buoyancy forces required to drive a dynamo for various shell thicknesses. Current thermal evolution models assume that the entropy requirement for core convection is similar to that for dynamo action (Williams and Nimmo, 2004), and although this may be the case for thick shell dynamos (Stevenson, 2001), it is not necessarily the case for dynamos operating in thinner shells since the magnetic Reynolds number decreases with decreasing shell thickness.

Since core cooling is directly linked to mantle cooling, we will also study the effect of the mantle convection mode in Mars on the dynamo process. Geodynamo studies which have implemented the Earth's pattern of mantle convection as a thermal boundary condition at the CMB have shown that the dynamo can be sensitive to thermal core-mantle interactions (Bloxham and Gubbins, 1987; Bloxham, 2000a,b; Christensen and Olson, 2003; Glatzmaier *et al.*, 1999). Some mantle convection models which can explain Mars' crustal dichotomy suggest that the mantle underwent a spherical harmonic degree 1 convection pattern with heat loss concentrated in one hemisphere (Zhong and Zuber, 2001; Zuber, 2001). If Mars underwent whole-mantle convection, then this signature would also have been present at Mars' CMB and may have affected the dynamo process. We will implement this heat flux pattern at the CMB in our models to determine the effect on dynamos operating in various shell thicknesses.

## **Saturn's Rotation Period and Magnetic Field**

The Cassini spacecraft, which began orbiting Saturn on June 30, 2004, has already begun returning valuable data from the planet. A very recent press release on the Jet Propulsion Lab website<sup>1</sup> presented a new puzzle regarding the relationship between Saturn's rotation and its magnetic field. Since giant planets have no surface features to track, and their atmospheric features may not move with the bulk rotation rate of the planet, the giant planet rotation periods are determined by measuring the rotational modulation of radio emissions from the planets magnetic fields. Saturn's rotation period which was measured by Voyager 1 and 2 appears to be shorter than the rotation period recently measured by Cassini by about 6 minutes. It is unlikely that the planet has slowed its rotation by this amount since the Voyager measurements so the discrepancy is being attributed to a slippage between the deep interior of the planet and the magnetic field which controls the radio emissions. As discussed in chapter 2, it has been suggested that Saturn possesses a stably-stratified layer surrounding the dynamo source region. Perhaps this geometry can cause the slippage between the field and the planet's bulk rotation. We plan to examine this from a numerical dynamo modeling perspective.

---

<sup>1</sup><http://www.jpl.nasa.gov/news.cfm?release=2004-164>

# Bibliography

- Acuna, M., J. Connerney, N. Ness, R. Lin, D. Mitchell, C. Carlson, J. McFadden, K. Anderson, H. Reme, C. Mazellem, D. Vignes, P. Wasilewski, and P. Cloutier (1999). Global distribution of crustal magnetization discovered by the Mars Global Surveyor MAG/ER experiment. *Science*, 284, 790–793.
- Aharonson, O., M. Zuber, and S. Solomon (2004). Crustal remanence in an internally magnetized non-uniform shell: a possible source for Mercury’s magnetic field? *Earth Planet. Sci. Lett.*, 218, 261–268.
- Al-Shamali, F., M. Heimpel, and J. Aurnou (2004). Varying the spherical shell geometry in rotating thermal convection. *Geophys. Astrophys. Fluid Dynam.*, 98, 153–169.
- Ardes, M., F. Busse, and J. Wicht (1997). Thermal convection in rotating spherical shells. *Phys. Earth Planet. Int.*, 99, 55–67.
- Arkani-Hamed, J. (2004). Timing of the Martian core dynamo. *J. Geophys. Res.*, 109. Doi:10.1029/2003JE002195.
- Aubert, J. and J. Wicht (2004). Axial vs. equatorial dipolar dynamo models with implications for planetary magnetic fields. *Earth Planet. Sci. Lett.*, 221, 409–419.
- Aurnou, J., S. Andreadis, L. Zhu, and P. Olson (2003). Experiments on convection in earth’s core tangent cylinder. *Earth Planet. Sci. Lett.*, 212, 119–134.
- Aurnou, J. and P. Olson (2001). Strong zonal winds from thermal convection in a rotating spherical shell. *Geophys. Res. Lett.*, 28, 2557–2560.
- Benedetti, L., J. Nguyen, W. Caldwell, H. Liu, M. Kruger, and R. Jeanloz (1999). Dissociation of CH<sub>4</sub> at high pressures and temperatures: Diamond formation in giant planet interiors? *Science*, 286, 100–102.
- Bloxham, J. (1990). On the consequences of strong stable stratification at the top of Earth’s outer core. *Geophys. Res. Lett.*, 17, 2081–2084.
- Bloxham, J. (2000a). The effect of thermal core-mantle interactions on the palaeomagnetic secular variation. *Phil. Trans. R. Soc. Lond. A*, 358, 1171–1179.
- Bloxham, J. (2000b). Sensitivity of the geomagnetic axial dipole to thermal core-mantle interactions. *Nature*, 405, 63–65.
- Bloxham, J. and D. Gubbins (1987). Thermal core-mantle interactions. *Nature*, 325, 511–513.
- Braginsky, S. and P. Roberts (1995). Equations governing convection in Earth’s core and the geo-dynamo. *Geophys. Astrophys. Fluid Dynam.*, 79, 1–97.
- Breuer, D. and T. Spohn (2003). Early plate tectonics versus single-plate tectonics on Mars: Evidence from magnetic field history and crust evolution. *J. Geophys. Res.*, 108. Doi:10.1029/2002JE001999.
- Buffett, B. and J. Bloxham (2002). Energetics of numerical geodynamo models. *Geophys. J. Int.*, 149, 211–224.
- Buffett, B. and G. Glatzmaier (2000). Gravitational braking of inner-core rotation in geodynamo

- simulations. *Geophys. Res. Lett.*, 27, 3125–3128.
- Bullard, E. and H. Gellman (1954). Homogeneous dynamos and terrestrial magnetism. *Phil. Trans. Roy. Soc. London A*, 247, 213–278.
- Busse, F. (1970). Thermal instabilities in rapidly rotating systems. *J. Fluid. Mech.*, 44, 441–460.
- Busse, F. (1983). A model of mean zonal flows in the major planets. *Geophys. Astrophys. Fluid Dynam.*, 23, 153–174.
- Busse, F. (1994). Convection driven zonal flows and vortices in the major planets. *Chaos*, 4, 123–134.
- Busse, F. (2000). Homogeneous dynamos in planetary cores and in the laboratory. *Ann. Rev. Fluid Mech.*, 32, 383–408.
- Busse, F. (2002). Convective flows in rapidly rotating spheres and their dynamo action. *Phys. Fluids*, 14, 1301–1314.
- Busse, F. and C. Carrigan (1976). Laboratory simulation of thermal convection in rotating planets and stars. *Science*, 191, 81–83.
- Busse, F., E. Grote, and A. Tilgner (1998). On convection driven dynamos in rotating spherical shells. *Stud. Geophys. Geod.*, 42, 211–223.
- Christensen, U. (2001). Zonal flow driven by deep convection in the major planets. *Geophys. Res. Lett.*, 28, 2553–2556.
- Christensen, U. (2002). Zonal flow driven by strongly supercritical convection in rotating spherical shells. *J. Fluid. Mech.*, 470, 115–133.
- Christensen, U. and P. Olson (2003). Secular variation in numerical geodynamo models with lateral variations of boundary heat flow. *Phys. Earth Planet. Int.*, 138, 39–54.
- Christensen, U., P. Olson, and G. Glatzmaier (1998). A dynamo model interpretation of geomagnetic field structures. *Geophys. Res. Lett.*, 25, 1565–1568.
- Christensen, U., P. Olson, and G. Glatzmaier (1999). Numerical modelling of the geodynamo: a systematic parameter study. *Geophys. J. Int.*, 401, 885–890.
- Christensen, U. and A. Tilgner (2004). Power requirement of the geodynamo from ohmic losses in numerical and laboratory dynamos. *Nature*, 429, 169–171.
- Coe, R., L. Hongre, and G. Glatzmaier (2000). An examination of simulated geomagnetic reversals from a palaeomagnetic perspective. *Phil. Trans. Roy. Soc. London A*, 358, 1141–1170.
- Connerney, J. E. P. (1981). The magnetic field of Jupiter: A generalized inverse approach. *J. Geophys. Res.*, 86, 7679–7693.
- Connerney, J. E. P. (1993). Magnetic fields of the outer planets. *J. Geophys. Res.*, 98, 18,659–18,679.
- Connerney, J. E. P., M. Acuna, and N. Ness (1987). The magnetic field of Uranus. *J. Geophys. Res.*, 92, 15,329–15,336.
- Connerney, J. E. P., M. Acuna, and N. Ness (1991). The magnetic field of Neptune. *J. Geophys. Res.*, 96, 19,023–19,042.
- Connerney, J. E. P., M. Acuna, P. Wasilewski, N. Ness, H. Reme, C. Mazellem, D. Vignes, R. Lin, D. Mitchell, and P. Cloutier (1999). Magnetic lineations in the ancient crust of Mars. *Science*, 268, 1892–1894.
- Connerney, J. E. P. and N. F. Ness (1988). Mercury's magnetic field and interior. In: *Mercury*, eds. F. Vilas, C. Chapman, and M. Matthews, pp. 494–513. University of Arizona Press.
- Conzelmann, V. and T. Spohn (1999). New thermal evolution models suggesting a hot, partially molten Mercuryian interior. *Bull. Am. Astron. Soc.*, 31, 1102.
- Correia, A. and J. Lasker (2004). Mercury's capture into the 3/2 spin-orbit resonance as a result of its chaotic dynamics. *Nature*, 429, 848–850.
- Cowling, T. (1934). The magnetic field of sunspots. *Mon. Not. Roy. Astron. Soc.*, 8, 345–355.

- David, H. and S. Hamann (1959). The chemical effects of pressure .5. The electrical conductivity of water at high shock pressures. *T. Faraday Soc.*, *55*, 72–78.
- Dormy, E., J. Valet, and V. Courtillot (2000). Numerical models of the geodynamo and observational constraints. *Geochem. Geophys. Geosyst.*, *1*, 2000GC000,062.
- Dumberry, M. and J. Bloxham (2003). Torque balance, Taylor's constraint and torsional oscillations in a numerical model of the geodynamo. *Phys. Earth Planet. Int.*, *140*, 29–51.
- Fearn, D. R. (1998). Hydromagnetic flow in planetary cores. *Rep. Prog. Phys.*, *61*, 175–235.
- Fearn, D. R. and D. Loper (1981). Compositional convection and stratification of Earth's core. *Nature*, *289*, 393–394.
- Giampieri, G. and A. Balogh (2002). Mercury's thermoelectric dynamo model revisited. *Planet. Space Sci.*, *50*, 757–762.
- Gilman, P. (1983). Dynamically consistent nonlinear dynamos driven by convection in a rotating spherical shell. II. Dynamos with cycles and strong feedbacks. *Astrophys. J. Suppl. Ser.*, *53*, 243–268.
- Gilman, P. and J. Miller (1981). Dynamically consistent nonlinear dynamos driven by convection in a rotating spherical shell. *Astrophys. J. Suppl. Ser.*, *46*, 211–238.
- Glatzmaier, G. A. (1984). Numerical simulations of stellar convective dynamos. I. The model and method. *J. Comp. Phys.*, *55*, 461–484.
- Glatzmaier, G. A. (1985a). Numerical simulations of stellar convective dynamos. II. Field propagation in the convection zone. *Astrophys. J.*, *291*, 300–307.
- Glatzmaier, G. A. (1985b). Numerical simulations of stellar convective dynamos. III. At the bottom of the convection zone. *Geophys. Astrophys. Fluid Dynam.*, *31*, 137–150.
- Glatzmaier, G. A. (2002). Geodynamo simulations - How realistic are they? *Ann. Rev. Earth Planet. Sci.*, *30*, 237–257.
- Glatzmaier, G. A. and T. Clune (2000). Computational aspects of geodynamo simulations. *Comput. Sci. Eng.*, *2*, 61–67.
- Glatzmaier, G. A., R. Coe, L. Hongre, and P. Roberts (1999). The role of the earth's mantle in controlling the frequency of geomagnetic reversals. *Nature*, *401*, 885–890.
- Glatzmaier, G. A. and P. H. Roberts (1995a). A three-dimensional convective dynamo solution with rotating and finitely conducting inner core and outer mantle. *Phys. Earth Planet. Int.*, *91*, 63–75.
- Glatzmaier, G. A. and P. H. Roberts (1995b). A three-dimensional convective self-consistent computer simulation of a geomagnetic field reversal. *Nature*, *377*, 203–209.
- Glatzmaier, G. A. and P. H. Roberts (1996a). An anelastic evolutionary geodynamo simulation driven by compositional and thermal convection. *Physica D*, *97*, 81–94.
- Glatzmaier, G. A. and P. H. Roberts (1996b). Rotation and magnetism of earth's inner core. *Science*, *274*, 1887–1891.
- Glatzmaier, G. A. and P. H. Roberts (1997). Simulating the geodynamo. *Contemp. Phys.*, *38*, 269–288.
- Glatzmaier, G. A. and P. H. Roberts (1998). Dynamo theory then and now. *Int. J. Eng. Sci.*, *36*, 1325–1338.
- Grote, E. and F. Busse (2000). Hemispherical dynamos generated by convection in rotating spherical shells. *Phys. Rev. E*, *62*, 4457–4460.
- Grote, E. and F. Busse (2001). Dynamics of convection and dynamos in a rotating sphere. *Fluid Dynam. Res.*, *28*, 349–368.
- Grote, E., F. Busse, and A. Tilgner (1999). Convection-driven quadrupolar dynamos in rotating spherical shells. *Phys. Rev. E*, *60*, R5025–R5028.
- Grote, E., F. Busse, and A. Tilgner (2000a). Effects of hyperdiffusivities on dynamo simulations. *Geophys. Res. Lett.*, *27*, 2001–2004.

- Grote, E., F. Busse, and A. Tilgner (2000b). Regular and chaotic spherical dynamos. *Phys. Earth Planet. Int.*, 117, 259–272.
- Gubbins, D. and P. H. Roberts (1987). Magnetohydrodynamics of the Earth's core. In: *Geomagnetism*, vol. 2, pp. 1–183. Academic Press LTD.
- Gubbins, D., C. Thomson, and K. Whaler (1982). Stable regions in the Earth's liquid core. *Geophys. J. R. Astron. Soc.*, 68, 241–251.
- Guillot, T. (1999). A comparison of the interiors of Jupiter and Saturn. *Planet. Space Sci.*, 47, 1183–1200.
- Hamann, S. and M. Linton (1969). Electrical conductivities of aqueous solutions of KCL, KOH, and HCl, and ionization of water at high shock pressures. *T. Faraday Soc.*, 65, 2186.
- Hanel, R., B. Conrath, L. Herath, V. Kunde, and J. Pirraglia (1981). Albedo, internal heat, and energy-balance of Jupiter-preliminary results of the Voyager infrared investigation. *J. Geophys. Res.*, 86, 8705–8712.
- Hanel, R., B. Conrath, V. Kunde, J. Pearl, and J. Pirraglia (1983). Albedo, internal heat flux and energy balance of Saturn. *Icarus*, 53, 62–285.
- Hauck, S., A. Dombard, R. Phillips, and S. Solomon (2004). Internal and tectonic evolution of Mercury. *Earth Planet. Sci. Lett.*, 222, 713–728.
- Hollerbach, R. and C. A. Jones (1993a). A geodynamo model incorporating a finitely conducting inner core. *Phys. Earth Planet. Int.*, 75, 317–327.
- Hollerbach, R. and C. A. Jones (1993b). Influence of the Earth's inner core on geomagnetic fluctuations and reversals. *Nature*, 365, 541–543.
- Hollerbach, R. and C. A. Jones (1995). On the magnetically stabilizing role of the Earth's inner core. *Phys. Earth Planet. Int.*, 87, 171–181.
- Holme, R. (1995). *The Magnetic Fields of Uranus and Neptune*. Ph.D. thesis, Harvard University.
- Holme, R. and J. Bloxham (1996). The magnetic fields of Uranus and Neptune: Methods and models. *J. Geophys. Res.*, 101, 2177–2200.
- Hubbard, W. B., A. Burrows, and J. Lunine (2002). Theory of giant planets. *Annu. Rev. Astron. Astrophys.*, 40, 103–136.
- Hubbard, W. B., W. Nellis, A. Mitchell, N. Holmes, S. Limaye, and P. McCandless (1991). Interior structure of Neptune: Comparison with Uranus. *Science*, 253, 648–651.
- Hubbard, W. B., M. Podolak, and D. Stevenson (1995). Interior of Neptune. In: *Neptune and Triton*, ed. D. Cruickshank, pp. 109–138. University of Arizona Press, Tucson.
- Ishihara, N. and S. Kida (2000). Axial and equatorial magnetic dipoles generated in a rotating spherical shell. *J. Phys. Soc. Jpn.*, 69, 1582–1585.
- Ishihara, N. and S. Kida (2002a). Dynamo mechanism in a rotating spherical shell: competition between magnetic field and convection vortices. *J. Fluid. Mech.*, 465, 1–32.
- Ishihara, N. and S. Kida (2002b). Equatorial magnetic dipole field intensification by convection vortices in a rotating spherical shell. *Fluid Dynam. Res.*, 31, 253–274.
- Jones, C. A., A. Longbottom, and R. Hollerbach (1995). A self-consistent convection driven geodynamo model, using a mean field approximation. *Phys. Earth Planet. Int.*, 92, 119–141.
- Jones, C. A., A. Soward, and A. Mussa (2000). The onset of convection in a rapidly rotating sphere. *J. Fluid. Mech.*, 405, 157–179.
- Kageyama, A., M. Ochi, and T. Sato (1999). Flip-flop transitions of the magnetic intensity and polarity reversals in the magnetohydrodynamic dynamo. *Phys. Rev. Lett.*, 82, 5409–5412.
- Kageyama, A. and T. Sato (1997a). Dipole field generation by an MHD dynamo. *Plasma Phys. Contr. F.*, 39, 83–91.
- Kageyama, A. and T. Sato (1997b). Generation mechanism of a dipole field by a magnetohydrodynamic dynamo. *Phys. Rev. E*, 55, 4617–4626.

- Kageyama, A. and T. Sato (1997c). Velocity and magnetic field structures in a magnetohydrodynamic dynamo. *Phys. Plasmas*, *4*, 1569–1575.
- Katayama, J., M. Matsushima, and Y. Honkura (1999). Some characteristics of magnetic field behaviour in a model of MHD dynamo thermally driven in a rotating spherical shell. *Phys. Earth Planet. Int.*, *111*, 141–159.
- Khurana, K., M. Kivelson, D. Stevenson, G. Schubert, C. Russell, R. Walker, and C. Polanskey (1998). Induced magnetic fields as evidence for subsurface oceans in Europa and Callisto. *Nature*, *395*, 777–780.
- Kida, S., K. Araki, and H. Kitauchi (1997). Periodic reversals of magnetic field generated by thermal convection in a rotating spherical shell. *J. Phys. Soc. Jpn.*, *66*, 2194–2201.
- Kida, S. and H. Kitauchi (1998a). Chaotic reversals of dipole moment of thermally driven magnetic field in a rotating spherical shell. *J. Phys. Soc. Jpn.*, *67*, 2950–2951.
- Kida, S. and H. Kitauchi (1998b). Thermally driven MHD dynamo in a rotating spherical shell. *Prog. Theor. Phys. Supp.*, *130*, 121–136.
- Kitauchi, H. (1998). Topological structure of magnetic flux lines generated by thermal convection in a rotating spherical shell. *J. Phys. Soc. Jpn.*, *67*, 1243–1249.
- Kitauchi, H. and S. Kida (1998). Intensification of magnetic field by concentrate-and-stretch of magnetic flux lines. *Phys. Fluids*, *10*, 457–468.
- Kivelson, M., K. Khurana, C. Russell, R. Walker, J. Warnecke, F. Coroniti, C. Polanskey, D. Southwood, and G. Schubert (1996). Discovery of Ganymede's magnetic field by the Galileo space-craft. *Nature*, *384*, 537–541.
- Kivelson, M., K. Khurana, D. Stevenson, L. Bennett, S. Joy, C. Russell, R. Walker, C. Zimmer, and C. Polanskey (1999). Europa and Callisto: Induced or intrinsic fields in a periodically varying plasma environment. *J. Geophys. Res.*, *104*, 4609–4625.
- Kono, M. and P. Roberts (2002). Recent geodynamo simulations and observations of the geomagnetic field. *Rev. Geophys.*, *40*, 1013.
- Kono, M., A. Sakuraba, and M. Ishida (2000). Dynamo simulation and palaeosecular variation models. *Phil. Trans. Roy. Soc. London A*, *358*, 1123–1139.
- Krimigis, S., R. Decker, M. Hill, T. Armstrong, G. Gloeckler, D. Hamilton, L. Lanzerotti, and E. Roelof (2003). Voyager I exited the solar wind at a distance of 85 AU from the sun. *Nature*, *426*, 45–48.
- Kuang, W. (1999). Force balances and convective state in the Earth's core. *Phys. Earth Planet. Int.*, *116*, 65–79.
- Kuang, W. and J. Bloxham (1997). An Earth-like numerical dynamo model. *Nature*, *389*, 371–374.
- Kuang, W. and J. Bloxham (1998). Numerical dynamo modeling: Comparison with the Earth's magnetic field. In: *The Core-Mantle Boundary Region*, Geodynamics 28. American Geophysical Union.
- Kuang, W. and J. Bloxham (1999). Numerical modeling of magnetohydrodynamic convection in a rapidly rotating spherical shell: Weak and strong field dynamo action. *J. Comp. Phys.*, *153*, 51–81.
- Kutzner, C. and U. Christensen (2002). From stable dipolar towards reversing numerical dynamos. *Phys. Earth Planet. Int.*, *131*, 29–45.
- Lepping, R., N. Ness, and K. Behannon (1979). Summary of Mariner 10 magnetic field and trajectory data for Mercury I and III encounters. *NASA Technical Memorandum*, *80600*, November.
- Lewis, J. (1995). *Physics and Chemistry of the Solar System*. Academic Press.
- Li, J., T. Sato, and A. Kageyama (2002). Repeated and sudden reversals of the dipole field generated by a spherical dynamo action. *Science*, *295*, 1887–1890.
- Lissauer, J., J. Pollack, G. Wetherill, and D. Stevenson (1995). Formation of the Neptune system.

- In: *Neptune and Triton*, ed. D. Cruickshank, pp. 37–108. University of Arizona Press, Tucson.
- Love, J. (2000). Dynamo action and the nearly axisymmetric magnetic field of Saturn. *Geophys. Res. Lett.*, 27, 2889–2892.
- Margot, J., S. Peale, R. Jurgens, M. Slade, and I. Holin (2004). Earth-based measurements of Mercury's forced librations in longitude. *Eos Trans. AGU*, 85, GP33A–03.
- Marley, M., P. Gomez, and M. Podolak (1995). Monte carlo interior models for Uranus and Neptune. *J. Geophys. Res.*, 100, 23,349–23,353.
- McDonald, F., E. Stone, A. Cummings, B. Heikkila, N. Lal, and W. Webber (2003). Enhancements of energetic particles near the heliospheric termination shock. *Nature*, 426, 48–50.
- McMillan, D., C. Constable, R. Parker, and G. Glatzmaier (2001). A statistical analysis of magnetic fields from some geodynamo simulations. *Geochem. Geophys. Geosyst.*, 2. Doi: 2000GC000130.
- Merrill, R. T., M. McElhinny, and P. McFadden (1996). *The Magnetic Field of the Earth*, vol. 63 of *International Geophysics Series*. Academic Press.
- Mitchell, A. and W. Nellis (1982). Equation of state and electrical conductivity of water and ammonia shocked to the 100 GPa (1 Mbar) pressure range. *J. Chem. Phys.*, 76, 6273–6281.
- Mitchell, A. et al. (1980). In: *High pressure science and technology*, eds. B. Vodary and P. Marteau, pp. 1048–1050. Pergamon Press, Oxford.
- Nellis, W. J. (2000). Metallization of fluid hydrogen at 140 GPa (1.4 Mbar): implications for Jupiter. *Planet. Space Sci.*, 48, 671–677.
- Nellis, W. J., D. Hamilton, N. Holmes, H. Radousky, F. Ree, A. Mitchell, and M. Nicol (1988). The nature of the interior of Uranus based on studies of planetary ices at high dynamic pressure. *Science*, 240, 779–781.
- Nellis, W. J., S. Weir, and A. Mitchell (1996). Metallization and electrical conductivity of hydrogen in Jupiter. *Science*, 273, 936–938.
- Ness, N. F., M. Acuna, K. Behannon, L. Burlaga, J. Connerney, R. Lepping, and F. Neubauer (1986). Magnetic fields at Uranus. *Science*, 233, 85–89.
- Ness, N. F., M. Acuna, L. Burlaga, J. Connerney, R. Lepping, and F. Neubauer (1989). Magnetic fields at Neptune. *Science*, 246, 1473–1478.
- Ness, N. F., K. Behannon, R. Lepping, and K. Schatten (1971). Use of two magnetometers for magnetic field measurements on a spacecraft. *J. Geophys. Res.*, 76, 3564–3573.
- Ness, N. F., K. Behannon, R. Lepping, and Y. Whang (1975). The magnetic field of Mercury I. *J. Geophys. Res.*, 80, 2708–2716.
- Ness, N. F., K. Behannon, R. Lepping, and Y. Whang (1976). Observations of Mercury's magnetic field. *Icarus*, 28, 479–488.
- Nimmo, F. and D. Stevenson (2000). Influence of early plate tectonics on the thermal evolution and magnetic field of Mars. *J. Geophys. Res.*, 105, 11,969–11,979.
- Ochi, M., A. Kageyama, and T. Sato (1999). Dipole and octapole field reversals in a rotating spherical shell: Magnetohydrodynamic dynamo simulation. *Phys. Plasmas*, 6, 777–787.
- Olson, P. and U. Christensen (2002). The time-averaged magnetic field in numerical dynamos with non-uniform boundary heat flow. *Geophys. J. Int.*, 151, 809–823.
- Olson, P., U. Christensen, and G. Glatzmaier (1999). Numerical modeling of the geodynamo: Mechanisms of field generation and equilibration. *J. Geophys. Res.*, 104 (B5), 10,383–10,404.
- Podolak, M., W. Hubbard, and D. Stevenson (1991). Models of Uranus' interior and magnetic field. In: *Uranus*, eds. J. Bergstrahl, E. Minor, and M. S. Matthews, pp. 29–61. University of Arizona Press, Tucson.
- Podolak, M., J. Podolak, and M. Marley (2000). Further investigations of random models of Uranus and Neptune. *Planet. Space Sci.*, 48, 143–151.
- Podolak, M., A. Weizman, and M. Marley (1995). Comparative models of Uranus and Neptune.

- Planet. Space Sci.*, 43 (12), 1517–1522.
- Proudman, J. (1916). On the motions of solids in a liquid possessing vorticity. *Proc. R. Soc. London A*, 92, 418–424.
- Roberts, P. (1968). On the thermal instability for a self-gravitating fluid sphere containing heat sources. *Phil. Trans. Roy. Soc. London A*, 263, 93–117.
- Roberts, P. H. and G. A. Glatzmaier (2000a). Geodynamo theory and simulations. *Rev. Mod. Phys.*, 72, 1081–1123.
- Roberts, P. H. and G. A. Glatzmaier (2000b). A test of the frozen-flux approximation using a new geodynamo model. *Phil. Trans. Roy. Soc. London A*, 358, 1109–1121.
- Roberts, P. H. and G. A. Glatzmaier (2001). The geodynamo, past, present and future. *Geophys. Astrophys. Fluid Dynam.*, 94, 47–84.
- Runcorn, S. (1975). An ancient lunar magnetic field. *Nature*, 253, 701–703.
- Ruzmaikin, A. A. and S. V. Starchenko (1991). On the origin of Uranus and Neptune magnetic fields. *Icarus*, 93, 82–87.
- Sakuraba, A. and M. Kono (1999). Effect of the inner core on the numerical solution of the magnetohydrodynamic dynamo. *Phys. Earth Planet. Int.*, 111, 105–211.
- Salpeter, E. (1973). Convection and gravitational layering in Jupiter and in stars of low mass. *Astrophys. J.*, 181, L83–L86.
- Schubert, G., M. Ross, D. Stevenson, and T. Spohn (1988). Mercury's thermal history and the generation of its magnetic field. In: *Mercury*, eds. F. Vilas, C. Chapman, and M. Matthews, pp. 429–460. University of Arizona Press.
- Schluz, M. and G. A. Paulikas (1990). Planetary magnetic fields: A comparative view. *Adv. Space Res.*, 10, 155–164.
- Siegfried, R. W. and S. C. Solomon (1974). Mercury: Internal structure and thermal evolution. *Icarus*, 23, 192–205.
- Srnka, L. (1976). Magnetic dipole moment of a spherical shell with TRM acquired in a field of internal origin. *Phys. Earth Planet. Int.*, 11, 184–190.
- Stanley, S. and J. Bloxham (2004). Convective-region geometry as the cause of Uranus' and Neptune's unusual magnetic fields. *Nature*, 428, 151–153.
- Stephenson, A. (1975). Crustal remanence and the magnetic moment of Mercury. *Earth Planet. Sci. Lett.*, 28, 454–458.
- Stevenson, D. J. (1983). Planetary magnetic fields. *Rep. Prog. Phys.*, 46, 555–620.
- Stevenson, D. J. (1987). Mercury's magnetic field: a thermoelectric dynamo? *Earth Planet. Sci. Lett.*, 82, 114–120.
- Stevenson, D. J. (2001). Mars' core and magnetism. *Nature*, 412, 214–219.
- Stevenson, D. J. (2003a). Planetary magnetic fields. *Earth Planet. Sci. Lett.*, 208, 1–11.
- Stevenson, D. J. (2003b). Styles of mantle convection and their influence on planetary evolution. *Comptes Rendus Geoscience*, 335, 99–111.
- Stevenson, D. J., T. Spohn, and G. Schubert (1983). Magnetism and thermal evolution of the terrestrial planets. *Icarus*, 54, 466–489.
- Stevenson, E., D. J. and Salpeter (1977). Phase-diagram and transport properties for hydrogen-helium fluid planets. *Astrophys. J. Suppl. S.*, 35, 221–237.
- Takahashi, F., J. Katayama, M. Matsushima, and Y. Honkura (2001). Effects of boundary layers on magnetic field behavior in an MHD dynamo model. *Phys. Earth Planet. Int.*, 128, 137–148.
- Takahashi, F., J. Katayama, M. Matsushima, and Y. Honkura (2003). Dynamo action and its temporal variation inside the tangent cylinder in MHD dynamo simulations. *Phys. Earth Planet. Int.*, 140, 53–71.
- Taylor, G. (1917). Motion of solids in fluids when the flow is not irrotational. *Proc. R. Soc. London*

- A*, 93, 99–113.
- Thompson, M., J. Christensen-Dalsgaard, M. Miesch, and J. Toomre (2003). The internal rotation of the Sun. *Annu. Rev. Astron. Astrophys.*, 41, 599–643.
- Tilgner, A. and F. Busse (1997). Finite amplitude convection in rotating spherical fluid shells. *J. Fluid. Mech.*, 332, 359–376.
- Wicht, J. (2002). Inner-core conductivity in numerical dynamo simulations. *Phys. Earth Planet. Int.*, 132, 281–302.
- Wicht, J. and P. Olson (2004). A detailed study of the polarity reversal mechanism in a numerical dynamo model. *Geochem. Geophys. Geosyst.*, 5, Q03H10.
- Williams, J. and F. Nimmo (2004). Thermal evolution of the Martian core: Implications for an early dynamo. *Geology*, 32, 97–100.
- Zhang, K. (1992). Spiralling columnar convection in rapidly rotating spherical shells. *J. Fluid. Mech.*, 236, 535–556.
- Zhang, K. (1994). On coupling between the Poincaré equation and the heat equation. *J. Fluid. Mech.*, 268, 211–229.
- Zhang, K. (1995). On coupling between the Poincaré equation and the heat equation: non-slip boundary conditions. *J. Fluid. Mech.*, 284, 239–256.
- Zhang, K. and G. Schubert (1996). Penetrative convection and zonal flow on Jupiter. *Science*, 273, 941–943.
- Zhang, K. and G. Schubert (2000). Teleconvection: Remotely driven thermal convection in rotating stratified spherical layers. *Science*, 290, 1994–1997.
- Zhang, K. and G. Schubert (2002). From penetrative convection to teleconvection. *Astrophys. J.*, 572, 461–476.
- Zhong, S. and M. Zuber (2001). Degree-1 mantle convection and the crustal dichotomy of Mars. *Earth Planet. Sci. Lett.*, 189, 75–84.
- Zuber, M. (2001). The crust and mantle of Mars. *Nature*, 412, 220–227.